

POLITECNICO DI TORINO



**CORSO DI LAUREA MAGISTRALE
IN INGEGNERIA AEROSPAZIALE**

FINAL TEST

**ANALYSIS OF DEPLOYABLE STRUCTURAL
ELEMENTS FOR SPACE APPLICATIONS**

CANDIDATE
SIMONE AMBROSINO

SUPERVISORS
ERASMO CARRERA
ALFONSO PAGANI

APRIL 2020

To my family

Abstract

In this work, a series of analyses concerning the behavior of structures typically used in space applications are carried out. These structures are united by their properties of lightweight and minimal thickness, along with the need for them to occupy a highly confined space; this last necessity makes the deployable structures the most acceptable solutions in the space industry.

The numerical analyses of this kind of structure are carried out through two different codes: the commercial software Abaqus and the Mul² code developed by the homonymous group of the PoliTo, based on the CUF theory. The objective of this work is, therefore, to introduce the main features of the deployable structures and then to demonstrate the ability of the Mul² code to reproduce very reliable results for different kinds of analysis and structures.

The thesis is subdivided into two distinct parts, presenting separately the theoretical subject on which the Mul² code is based, and the numerical analysis themselves.

Chapter 1 is an introduction to the main subject: deployable structures. The existing literature on the argument is presented, together with some classification methods. Moreover, some relevant and commonly used space structures are showed, and both their folding processes and their applications are given.

In Chapter 2, the CUF theory is briefly introduced, just enough to understand the mathematics standing hidden behind the code. The application of the CUF theory to non-linear analysis is presented too.

Chapter 3 deals with the preliminary analysis of some classical structures, not necessarily applicable for spatial purposes: in ascending order of complexity are analyzed square beams, C-beams, and C-beams with holes along the axis.

In Chapter 4, typical space structures such as tape springs are analyzed, also studying the effect of some features on the buckling behavior. At the end of the

chapter, the numerical results are also compared with an experimental test carried out by the CalTech.

At last, in Chapter 5, TRAC boom structures are introduced and analyzed. Their buckling behavior is deeply discussed, also through a linearized buckling analysis. Last but not least, results concerning a parametric analysis on the effects of the boom length are shown.

In the Conclusions are provided some general comments regarding the analysis previously made, and some ideas for future developments.

Contents

1	Introduction	1
1.1	Coiled rods	4
1.2	Structural mechanisms	7
1.3	Membranes	8
1.4	Flexible shells	12
2	Unified models for flexible beams	15
2.1	Preliminaries	15
2.2	Carrera Unified Formulation	17
2.2.1	Unified formulation	17
2.2.2	Finite element formulation	18
2.2.3	Secant stiffness matrix	19
2.2.4	Loading vector	20
2.3	Non-linear analysis	21
2.3.1	Newton-Raphson linearization	21
2.3.2	Crisfield arc-length method	22
2.3.3	Tangent stiffness matrix	24
3	Preliminary results	26
3.1	Square Beam	26
3.1.1	CUF Model	27
3.1.2	Analysis	29
3.1.3	Results	29
3.2	C-Beam	31
3.2.1	Abaqus model	32
3.2.2	CUF model	37

3.2.3	Results	39
3.3	C-Beam with holes	43
3.3.1	Load in the plane of the core	43
3.3.2	Load out of the plane of the core	47
3.3.3	Bending moments applied to the edges of the beam	49
3.3.4	Bending moments with thin cross-section	51
4	Analysis of tape spring structures	56
4.1	Linear analysis	57
4.1.1	Geometry	57
4.1.2	Abaqus analysis	58
4.1.3	MUL ² analysis	59
4.1.4	Comparison between Abaqus and MUL ² solutions	64
4.2	Non-linear analysis and sensitivity versus curvature radius	65
4.2.1	CUF validation	66
4.2.2	CUF analysis	70
4.2.3	Abaqus analysis	72
4.3	Comparison with experimental analysis	75
4.3.1	Experiment	75
4.3.2	Numerical results	80
5	Analysis of TRAC boom structures	84
5.1	Introduction	84
5.2	Linear analysis	88
5.2.1	Z-bending	89
5.2.2	X-bending	91
5.3	Linearized buckling analysis	95
5.4	Non-linear analysis and sensitivity versus boom length	99
5.4.1	Z-bending	99
5.4.2	X-bending	104
	Conclusions	111
	Bibliography	113

List of Figures

1.1	Adrover classification - some examples [26]	2
1.2	Adrover classification [11]	3
1.3	Coiled rod [23]	5
1.4	Coilable mast [23]	5
1.5	Coilable mast retraction	6
1.6	Pantograph deployment	8
1.7	Ring-like pantograph deployment	9
1.8	Ring-like pantograph components [23]	9
1.9	Letter folding [23]	10
1.10	Map folding [23]	10
1.11	Miura-ori folding [23]	11
1.12	Solar concentrator [23]	12
1.13	Tape measure booms [23]	13
1.14	Tape measure coiling [23]	13
1.15	Tape measure bending [23]	14
2.1	Non-linear analysis control methods [5]	22
2.2	Crisfield arc-length method [22]	23
3.1	Cantilever square beam geometry. L is the length, h the height	27
3.2	Deformed shape for three different load values - square beam	30
3.3	Square beam load-deflection curve, reference from [4]	30
3.4	C-beam cross-section. Points for load application and displacement monitoring are included	31
3.5	C-beam, short configuration - Shell and solid elements mesh comparison - 10x18 elements	33

3.6	C-Beam, short configuration - Deformed shapes for different load values	33
3.7	C-Beam, long configuration - Shell and solid elements mesh comparison	35
3.8	C-Beam, long configuration - Deformed shapes for different load values	36
3.9	C-Beam - Cross-section CUF meshes	38
3.10	C-Beam load-deflection curve ($\frac{L}{h} = 3$)	40
3.11	C-Beam deformed CUF models	41
3.12	C-Beam load-deflection curve ($\frac{L}{h} = 30$)	42
3.13	Booms unfolding [18]	43
3.14	C-Beam with holes load and control point disposition (left), and cross-section mesh 7 L9 (right)	44
3.15	Holes disposition in C-Beam	44
3.16	Holed C-beam equilibrium curve due to a load directed along the core direction	45
3.17	Deformed shapes of the C-Beam with two holes, load along the core direction	46
3.18	Holed C-beam cross-section mesh with lateral forces, 7L9	47
3.19	Equilibrium curve for a load directed out of the plane of the core	48
3.20	C-Beam with two holes and load directed out of the plane of the core - deformed shapes	49
3.21	Holed C-beam with two moments applied, Cross-section mesh, 9 L9; loads are applied in points A and C, boundary conditions in points B	50
3.22	Holed C-beam equilibrium curve due to two moments applied at the extremities of the structure	50
3.23	C-Beam with one hole and moments applied to the two extremities - deformed shapes	52
3.24	Holed C-beam with thin cross-section mesh, 9 L9	53
3.25	Thin C-beam, hole location	53
3.26	Holed C-beam equilibrium curve with the thin structure and bending moments applied	54
3.27	C-Beam with one hole, thin cross-section and bending moment - Deformation	55

4.1	Tape spring measure ready to be tested, courtesy of CalTech	56
4.2	Tape spring measure cross-section geometry	57
4.3	Tape spring measure Abaqus model, 16x113 shell elements. RP1 and RP2 are the rotation points	58
4.4	Tape spring measure Abaqus model deformation; colors scale stands for the vertical displacement	60
4.5	Tape spring measure CUF cross-section mesh, 14 L9; forces are applied in points C and A, BCs in points B	62
4.6	Tape spring measure CUF model deformed shape; colder colors indicate higher vertical displacement	63
4.7	General tape geometry [28]	65
4.8	Tape typical $M-\theta$ diagram [28]	66
4.9	Abaqus model tape R100, 12x85 shell elements	67
4.10	CUF model tape R100, 10 L9	68
4.11	Detail of Fig. 4.10	68
4.12	Equilibrium curve, tape R100, Abaqus shell and CUF models	69
4.13	Effect of radius of curvature on the tape equilibrium curve, various CUF models	70
4.14	Tape CUF meshes, different curvature radius and number of elements	71
4.15	Effect of the radius of curvature on the tape equilibrium curve, Abaqus shell models	73
4.16	Tape R100, Abaqus shell models deformation in the points indicated in Fig. 4.15a	74
4.17	Commercial tape spring	76
4.18	FaroArm scanner	76
4.19	Tape spring sample, courtesy of Caltech	77
4.20	Fischer's machine, courtesy of Caltech	77
4.21	Experimental results, opposite sense bending, courtesy of Caltech	78
4.22	Experimental results, equal sense bending, courtesy of Caltech	79
4.23	Tape spring measure complete equilibrium curve	81
4.24	Tape spring measure equilibrium curve - opposite sense detail	82
4.25	Tape spring measure deformed shapes with Abaqus, 16x113 shell elements	83

5.1 TRAC geometry in the open and closed configuration (modified from [2]) 85

5.2 TRAC boom with central hub mechanism [2] 85

5.3 Typical TRAC application in membranes supporting [1] 86

5.4 Membrane folding process thanks to TRAC booms [1] 86

5.5 TRAC cross-section geometry with main parameters denomination (modified from [16]). $w = 8 \text{ mm}$, $t = 0.08 \text{ mm}$, $r = 12.7 \text{ mm}$, $\theta = 90^\circ$ 87

5.6 TRAC boom geometry with orthogonal axis orientation 88

5.7 TRAC boom cross-section mesh for the Z-Bending configuration. Each of the triangle represents the edge of an element. Letters indicate the nodes upon which BCs and loads are applied, BCs in A, loads in B. 32 L9 89

5.8 Detail of the vertical flange of the cross-section of Fig. 5.7, together with the conjunction zone. 12 L9 elements on this flange 90

5.9 Deformed shape of the TRAC boom subjected to $M_Z = 1000 \text{ Nmm}$, linear static analysis. Scale factor of 20 91

5.10 TRAC boom cross-section mesh for the X-Bending configuration. Each of the triangle represents the edge of an element. Letters indicate the nodes upon which BCs and loads are applied, BCs in A, loads in B. 34 L9 92

5.11 Detail of the vertical flange of the cross-section of Fig. 5.10, together with the conjunction zone. 14 L9 elements on this flange 93

5.12 Deformed shape of the TRAC boom subjected to $M_X = 2000 \text{ Nmm}$, linear static analysis. Scale factor of 20 94

5.13 Deformed shape of the TRAC boom subjected to $M_X = -2000 \text{ Nmm}$, linear static analysis. Scale factor of 20 94

5.14 Deformed shapes of the TRAC boom subjected to uniform compression, buckling analysis. Scale factor of 20 95

5.15 Deformed shapes of the TRAC boom subjected X-bending, buckling analysis. Scale factor of 20 96

5.16 Deformed shapes of the TRAC boom subjected Z-bending, buckling analysis. Scale factor of 20 97

5.17 Deformed shape of the TRAC boom subjected to $M_Z = 1000 \text{ Nmm}$, Non-linear static analysis. Scale factor of 20 100

5.18 TRAC boom 500 <i>mm</i> long, equilibrium curve under Z-bending. Linear analysis result is included	100
5.19 TRAC boom 500 <i>mm</i> long deformed shape at the end of the equilibrium curve ($M_Z = 2546 \text{ Nmm}$, $\theta = 1.43^\circ$)	101
5.20 TRAC boom equilibrium curve under Z-bending for three different lengths	102
5.21 TRAC boom 1000 <i>mm</i> long deformed shape at the end of the equilibrium curve ($M_Z = 2185 \text{ Nmm}$, $\theta = 3.40^\circ$)	103
5.22 TRAC boom 1500 <i>mm</i> long deformed shape at the end of the equilibrium curve ($M_Z = 2293 \text{ Nmm}$, $\theta = 4.71^\circ$)	104
5.23 Deformed shape of the TRAC boom subjected to $M_X = 2000 \text{ Nmm}$, Non-linear static analysis. Scale factor of 20	105
5.24 Deformed shape of the TRAC boom subjected to $M_X = -2000 \text{ Nmm}$, Non-linear static analysis. Scale factor of 20	105
5.25 TRAC boom 500 <i>mm</i> long, equilibrium curve under X-bending. Linear analysis result is included	106
5.26 TRAC boom 500 <i>mm</i> long deformed shape at the end of the equilibrium curve ($M_X = 7923 \text{ Nmm}$, $\theta = 2.26^\circ$)	107
5.27 TRAC boom 500 <i>mm</i> long deformed shape at the end of the equilibrium curve ($M_X = -11597 \text{ Nmm}$, $\theta = -2.89^\circ$)	107
5.28 TRAC boom equilibrium curve under X-bending for three different lengths	108
5.29 TRAC boom 1000 <i>mm</i> long deformed shape at the end of the equilibrium curve in the opposite sense bending ($M_X = -2238 \text{ Nmm}$, $\theta = -1.28^\circ$). Scale factor of 5	109
5.30 TRAC boom 1500 <i>mm</i> long deformed shape at the end of the equilibrium curve in the opposite sense bending ($M_X = -10366 \text{ Nmm}$, $\theta = -9.55^\circ$)	109

List of Tables

3.1	Square beam material properties	27
3.2	C-Beam material properties	37
4.1	Tape spring measure CUF model material properties	61
4.2	Loads applied on the tape	62
4.3	Longitudinal displacements of some relevant nodes	63
4.4	Comparison between the rotations obtained with Abaqus and Mul ²	64
4.5	$M - \theta$ curve parameters variation due to curvature radius changing	72
5.1	TRAC boom Z-bending loads (expressed in $[N]$)	90
5.2	TRAC boom Z-bending boundary conditions	90
5.3	TRAC boom X-bending loads (expressed in $[N]$). For a negative moment the all the signs must be changed	93
5.4	TRAC boom X-bending boundary conditions	93
5.5	TRAC boom first critical loads	98

Chapter 1

Introduction

This first introductory chapter deals with a quick overview of the various deployable structures, with a particular focus on space applications. In the beginning, a definition for this kind of structure is given, also reporting some examples already written in literature; then, a sort of classification is described, based on geometry, functional features or technology. In the final part of the chapter, three different families of deployable structures are described singularly. The main source for this overview is taken from the work of Pellegrino (2001) [23]. More info about deployable and inflatable structures than the ones briefly introduced hereafter can be found in [13], [21], [14].

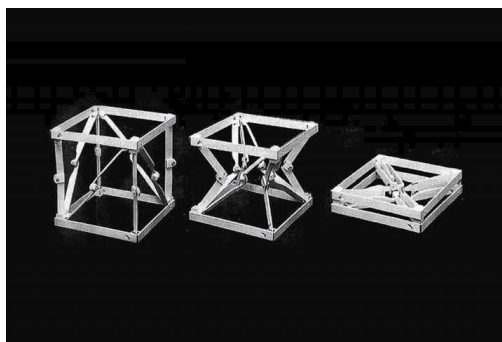
Let's start from the etymological meaning of the word *deployable* [11]: it stems from the Latin *displicare*, which precisely means *to deploy*. Thus, deployable structures are such elements able to modify their configuration from a folded state to a deployed (unfolded) one, through a transformation that is called, again, *deployment*. The inverse transformation, the transition from the unfolded back to the folded configuration, is commonly named *retraction*.

Typically, the deployment should be performed autonomously, thus the mechanism responsible for the structure movement is quite essential. Moreover, the transition from one configuration to the other must be controlled in order to maintain a fluid motion and to avoid damages in the structure.

Deployable structures are vital for space applications, due to their lightweight and ease of accommodating in tiny compartments. They are usually folded dur-

ing the launch of the spacecraft, and unfold themselves automatically when the operative orbit is reached, or when their functionalities are needed. Thus, functional requirements are different for folded and unfolded configuration: the former one requires small volume and compact structure, the latter one the functions for which the instrument has been designed.

One of the most common examples of a deployable instrument is the umbrella, which is usually folded, and then deployed when it is necessary to cover from rain (i.e., to perform its function). On the other hand, typical space applications for deployable structures are accounted for by solar panels deployment mechanisms, expandable antennas, solar reflectors, and many others.



(a) Rigid structure



(b) Deformable structure



(c) Flexible structure



(d) Combined structure

Figure 1.1: Adrover classification - some examples [26]

A recent classification was made by Adrover (2015) [26]. The author at first

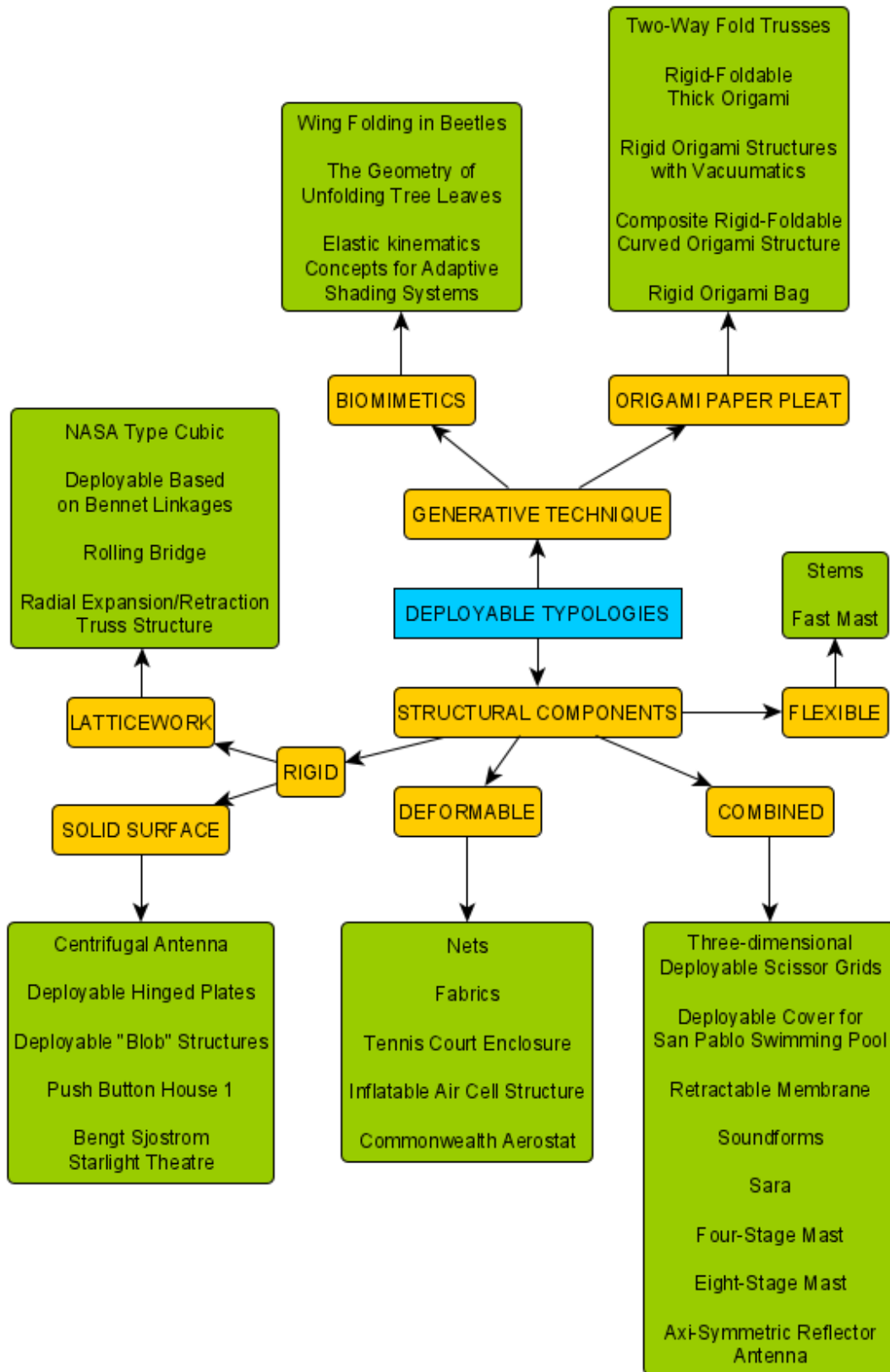


Figure 1.2: Adrover classification [11]

made a general distinction based on the approach used for the development of the structure: "Structural components" are those instruments whose design is driven by the structural mechanism that moves its parts; "Generative Technique" is used instead for objects whose development is based on movements and forms inspired by other sources. This last family contains, for example, origami techniques.

The focus of this study must remain obviously on structural components because this class represents all the deployable engineering structures. The author goes on, subdividing these structures into four categories: rigid, deformable, flexible, and combined components. The first two of them are the categories that are usually adopted in literature, whereas Adrover added the last two in order to include other structures which were not included in the first two. The overall classification can be seen in Fig.1.2.

An example of each type of deployable class is showed in Fig. 1.1: the rigid one is a truss structure developed by NASA in 1997 as extensible support for either solar concentrators or phased arrays; the deformable one represents a connection of different inflated air cells, which can become very useful in the colonization of other celestial bodies; the flexible structure is a BRC, utilized in various applications such as deployable tube pointing camera mechanisms; the combined structure is a Soundform, the first outdoor portable stage invented in 2012 and capable of optimizing sound audience in the neighboring.

Some of the items collocated in Fig.1.2 will be adequately presented in the following sections.

On the other hand, a real classification was not made by Pellegrino, who preferred to present some relevant and quite generic examples one by one. This is the approach that will be adopted hereafter.

1.1 Coiled rods

A simple example of a coiled rod is shown in Fig 1.3. Here a rod with a circular cross-section, wrapped around a spool with radius R , is deployed into a straight structure employing a series of rotative mechanisms.

These spools are contained in small housings and deployed when needed. Typical materials for the rod structure can be glass fibers or even steel. Despite the

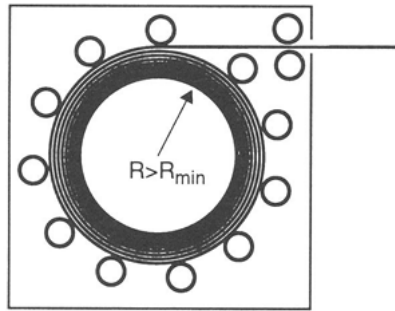


Figure 1.3: Coiled rod [23]

lightweight and small volume, a harmful property of such a structure is the not excellent stiffness: in fact, these types of coiled rods are only a few more rigid than a simple tape measure, though this last one has a housing dimension typically one-fifth of the coiled rod.

Many improvements can be reached with a different kind of structure: the lattice column, or coilable mast. A schematic representation of such a device is shown in Fig. 1.4.

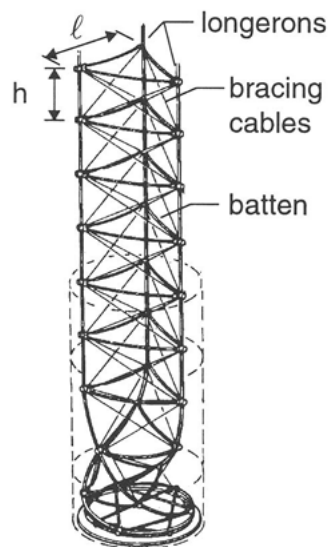


Figure 1.4: Coilable mast [23]

The assembly of various components composes this complex structure: some longerons (3 in this case, that is the minimum number allowable) run along the

longitudinal direction, and are interconnected by transversal elements like bracing cables and battens. Regarding Fig. 1.4, the battens form a series of equidistant triangles lying on the transversal plane, each vertex of the triangle is connected by the bracing cables to the vertexes belonging to different longerons of the triangles above and underneath. The space between two successive triangles is named "bay". This structure can reach a very high stiffness maintaining a little weight, and it is usually utilized for the deployment of some scientific instruments or solar arrays.

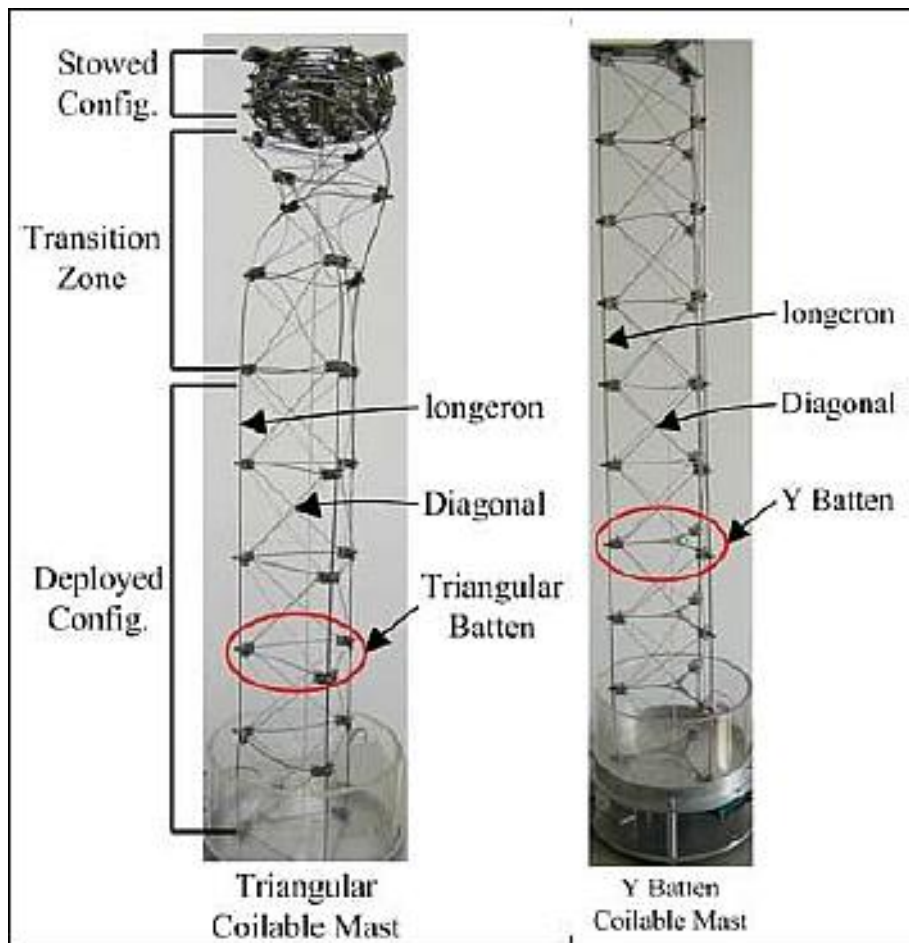


Figure 1.5: Coilable mast retraction

In order to achieve an efficiently working structure, the $\frac{h}{l}$ ratio must be decided following some rules:

- each bay should be approximately square to obtain an efficient structure (i.e. $\frac{h}{l} \approx 1$);

- stacking requirements tell that $h \neq \frac{2\pi R}{3}$, where R is the radius of the mast in the folded configuration, in order to guarantee a proper helical stacking without leaving any gap in the closed structure;
- the local buckling load of each bay should be smaller, but not too much smaller than the global buckling load.

The last of the three rules is usually the most demanding, thus the typical $\frac{h}{l}$ ratio is equal to $\frac{2}{3}$.

Let us describe now the retracting process with the help of Fig. 1.5. It shows how the folding of a typical short mast (up to 3 m) works: a compression load is applied at the top edge of the mast, which collapses and begins to rotate and get compressed, creating a helical transition structure that moves on toward the base of the mast. If the coilable mast is too long, then the stiffness of the transition region is not big enough to support the stowed region above, and hence the first part to collapse into a helix is collocated near the base instead of the top. In both cases, the base of the structure is typically contained within a canister, which can rotate, moved by an electrical motor, and contribute with the mast retraction.

1.2 Structural mechanisms

The structural mechanisms presented here are "*assemblies of rigid parts connected by movable joints, arranged in such a way that the transformation from a packaged to a deployable configuration is possible*" [23]. These structures look very similar to the coilable masts already discussed, but the main difference is that structural mechanisms are rigid parts assembled into a new structure utilizing unrelated joints, whereas the joints of the coilable masts are part of the structure themselves.

An interesting example of such a structure is the pantograph [32], an assembly of bars connected by multiple joints that permit their rotation, as shown in Fig. 1.6. Here the deployment mechanism is also represented.

In the figure, some cables connecting the joints are also visible; these are pre-tensioned in the deployed configuration in order to increase the structural stiffness.

Another configuration is the ring-like pantograph, as the one shown in Fig. 1.7. Here the deployment is obtained through a radial motion of the structure, which increases its diameter expanding. In this kind of pantograph, it is not rare

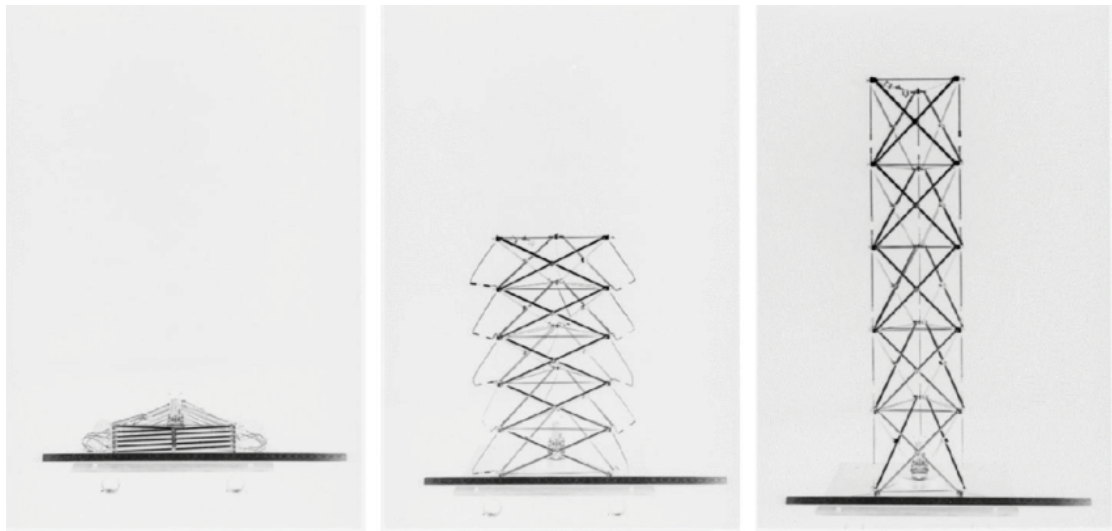


Figure 1.6: Pantograph deployment

to have different dimensions of the bars, as shown in Fig. 1.8; in this way, it is possible to create a structure that is smaller in the center and higher in the outer region. Ring-like pantographs are often used in the deployment mechanism of parabolic antennas due to their circular shape, which is very similar to the antenna to accommodate.

1.3 Membranes

Membranes are very versatile structures, modeled as thin layers of material that can be folded in various ways, according to the functional requirements to achieve. When they are subjected to a biaxial state of tension, they reach a good value of stiffness and stability, but once the tension is removed, they can collapse easily into the packed configuration, by a series of folding steps which can be arranged in every desired way. Three ways of folding are the most commonly used and are described hereafter.

Letter folding This folding process is the most straightforward and consists of a series of folding about the center lines: taking as reference Fig. 1.9, the membrane is first folded about its centerline, then about a new centerline in the perpendicular direction, and this process is repeated until the complete packaged configuration

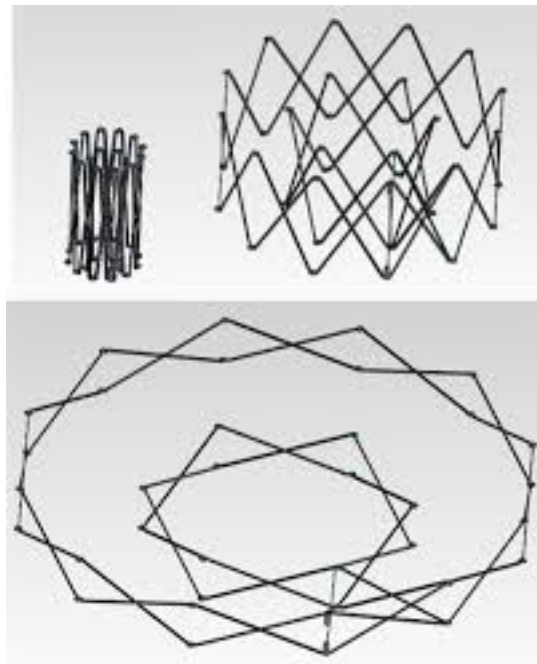


Figure 1.7: Ring-like pantograph deployment

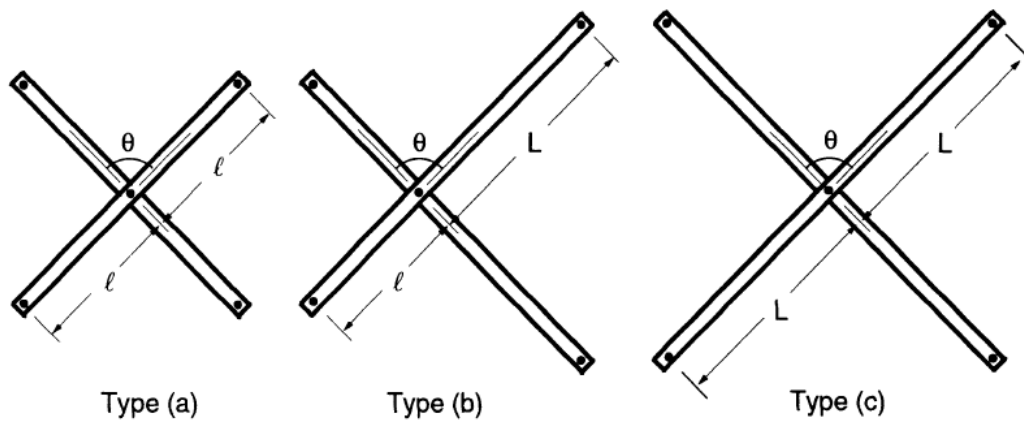


Figure 1.8: Ring-like pantograph components [23]

is reached, alternating 0° and 90° foldings.

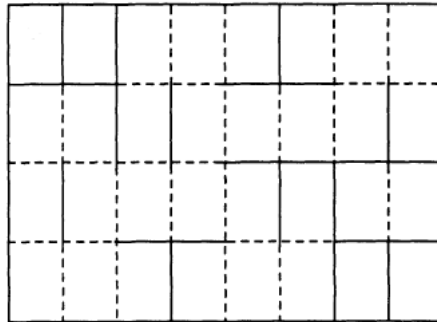


Figure 1.9: Letter folding [23]

As can be reasonably thought, the unfolding process must take place in precisely the inverse order than the folding one: a first unfold in a direction, then one in the perpendicular one, repeating these steps until the membrane is fully deployed. This procedure implies a very demanding automation process to perform, and then this folding way is not very used.

Map folding The map folding process is an evolution of the letter folding one: the folds are first made in only one direction, creating a concertina, and then the process is repeated in the perpendicular direction. The result of such folding is shown in Fig. 1.10.

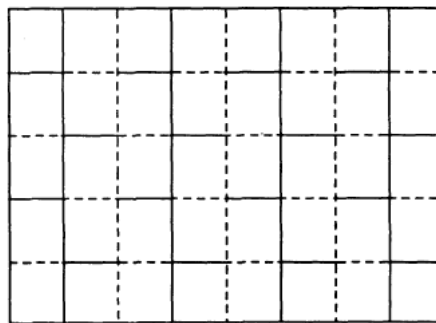


Figure 1.10: Map folding [23]

The improvement given to the unfolding process by this way of folding is that now the membrane is first completely unfolded in a direction, and then entirely

in the other; only two different movements are needed then, instead of a sequence of alternate unfolds as in the letter folding configuration. A further improvement can be reached with the Miura-ori folding.

Miura-ori folding This folding philosophy is the most complex but can imply a significant simplification in the unfolding process. The Miura-ori folding is showed in Fig. 1.11.

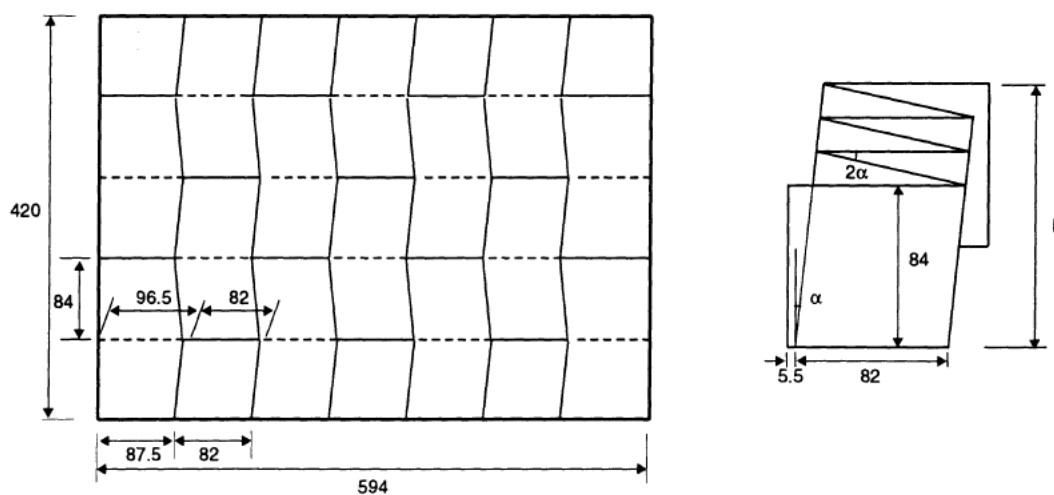


Figure 1.11: Miura-ori folding [23]

The vertical folds lines are not straight but follow a zigzag path. This kind of folding has the great advantage of permitting the unfolding process to be performed by only one step, which is single traction along the diagonal direction of the rectangular membrane. This leads to an enormous simplification of the deployment mechanism. Moreover, in the packed configuration, the structure maintains a small distance from every membrane layers; in this way, the maximum curvature is reduced and consequently, also the stresses. In order to have a look at the work of Miura one can use as reference [20].

An example of a membrane structure application is showed in Fig. 1.12: a solar rays concentrator for a solar panel. Its function is elementary: solar rays are reflected on the membrane and directed toward the solar array; in this way, the apparent surface of the solar panel is increased by several factors. The two

membranes visible in the figure are deployed using the booms in correspondence of the short edges. Thus, the folding process would probably be a single concertina, maintaining the packed shape of the structure as one long strip. Once they are deployed, each reflector is tensioned by a tension spring, which maintains the membrane wrinkle-free.

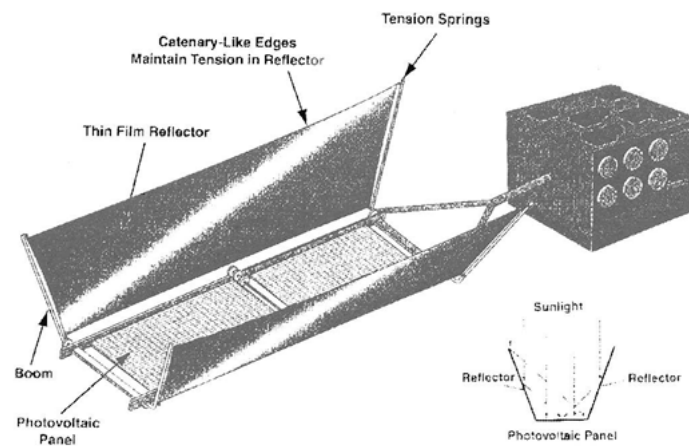


Figure 1.12: Solar concentrator [23]

1.4 Flexible shells

The most common example of a flexible shell structure is the steel tape measure: it is formed by a skinny layer of steel (typical thickness varies from 0.1-0.2 *mm*) which can reach lengths of 3 *m*, curved with a radius of 12-14 *mm* (the cross-section is an arc of a circle). In the packed configuration, the tape is flattened and coiled into a small container. Usually, the booms are arranged as showed in Fig. 1.13. Here three different configurations are visible:

- a STEM** One single tape with a great arc angle, greater than 360° , forming a circular extendible tube;
- b bi-STEM** Two tapes are nested into each other, creating a symmetric structure with a short transition region;
- c Collapsible tube** One single tape with a double layer with opposite curvature, which increases the torsional stiffness considerably.

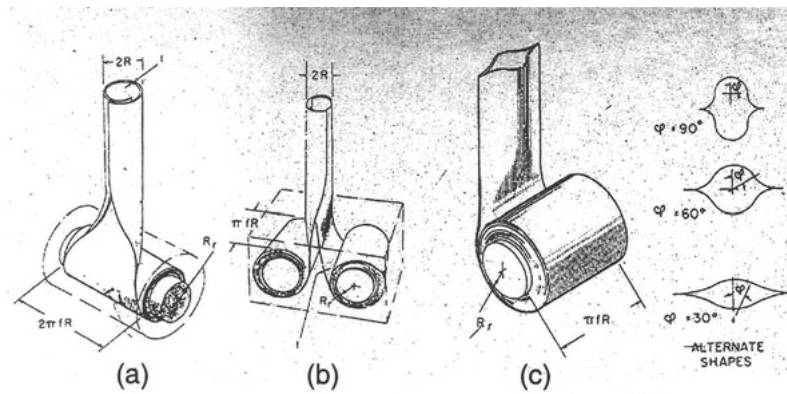


Figure 1.13: Tape measure booms [23]

In the folded configuration, these structures are flattened, and, due to their minimal thickness, this flattening acts as an elastic deformation only. The elastic energy held in the structure is released once the tape is fully deployed. Usually, one can identify two different ways of folding: equal sense and opposite sense.

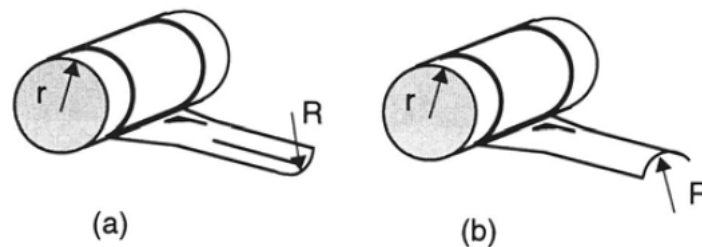


Figure 1.14: Tape measure coiling [23]

Figure 1.14 shows the equal sense coiling on the left, and the opposite sense coiling on the right. In the first case, the edges of the shell go into compression during coiling, whereas in the second case, they go into traction. Typically, $\frac{r}{R}$ ratios are close to 1.

The same nomenclature is adopted when the tape is subjected to a flexion, as in Fig. 1.15. The top figures show the opposite sense bending, whereas the bottom figures the equal sense one. The behavior of this kind of structure under the effect of bending moments is the subject of the successive analyses reported in the following chapters.

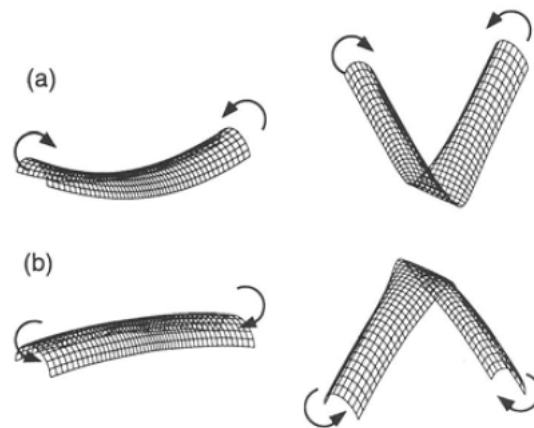


Figure 1.15: Tape measure bending [23]

A practical application of a flexible shell was used for the solar arrays deployment system of the Hubble space telescope, where bi-STEM tapes were adopted.

For more info about the behavior of these structures, one can see as reference [28].

Chapter 2

Unified models for the analysis of highly flexible beams

In this chapter is presented the CUF theory and its application on non-linear analysis. In the beginning, there is an introductory section where the main vectors appearing in the structural mechanics are showed. Then the CUF is fully explained, together with the derivation of the governing equations and their respective matrices. At last, the non-linear analysis procedure is exposed, with particular reference to the Crisfield arch-length method.

In order to carry out this theoretical study, the main works taken as reference are [7] for the beam models, whereas [22] for the non-linear analysis.

2.1 Preliminaries

Before to start talking about the mathematics involved in the classical theories and CUF, an introduction of the main elements that are going to be find hereafter must be made. Let's define, for the moment, how the components of displacements, strains and stresses are named:

- Displacements \mathbf{u} . The displacement components of a point P belonging to a deformable body are contained into the displacement vector; in a three-dimensional space this vector has got three components, as follows:

$$\mathbf{u} = \left\{ u_x, u_y, u_z \right\}^T$$

Each component represents the displacement value along one of the three orthogonal axis (x , y , z in this case).

- Strains ϵ . The strain vector is composed by nine terms:

$$\epsilon = \left\{ \epsilon_{xx} \quad \epsilon_{yy} \quad \epsilon_{zz} \quad \epsilon_{xz} \quad \epsilon_{yz} \quad \epsilon_{xy} \quad \epsilon_{zx} \quad \epsilon_{yx} \quad \epsilon_{zy} \right\}^T$$

The first three terms are the axial deformations, whereas the last six ones are the shear deformations, which are symmetric. For this reason the independent terms are only six, and the vector is generally written as:

$$\epsilon = \left\{ \epsilon_{xx} \quad \epsilon_{yy} \quad \epsilon_{zz} \quad \epsilon_{xz} \quad \epsilon_{yz} \quad \epsilon_{xy} \right\}^T$$

- Stresses σ . The stress vector is composed by nine terms:

$$\sigma = \left\{ \sigma_{xx} \quad \sigma_{yy} \quad \sigma_{zz} \quad \sigma_{xz} \quad \sigma_{yz} \quad \sigma_{xy} \quad \sigma_{zx} \quad \sigma_{yx} \quad \sigma_{zy} \right\}^T$$

The first three terms are the axial stresses, whereas the last six ones are the shear stresses, which are symmetric. For this reason the independent terms are only six, and the vector is generally written as:

$$\epsilon = \left\{ \sigma_{xx} \quad \sigma_{yy} \quad \sigma_{zz} \quad \sigma_{xz} \quad \sigma_{yz} \quad \sigma_{xy} \right\}^T$$

Stresses and strains are not independent but are linked by, in the case of linear elastic materials, the Hooke's law, which provides the constitutive relation. It states that:

$$\sigma = \mathbf{C}\epsilon \quad (2.1)$$

where \mathbf{C} is the material stiffness matrix.

The following expression governs strains and displacements relation:

$$\epsilon = \epsilon_l + \epsilon_{nl} = (\mathbf{b}_l + \mathbf{b}_{nl})\mathbf{u} \quad (2.2)$$

where \mathbf{b}_l and \mathbf{b}_{nl} are respectively the linear and nonlinear matrices containing differential operators; their complete form can be read in [22].

2.2 Carrera Unified Formulation

The CUF is a refined beam theory able to overcome the limits of classical modeling techniques. In fact, classical theories like the Euler-Bernoulli (EBBT) [10] and Timoshenko (TBT) [30] models are based on a fixed number of variables, and this number is usually related to the particular problem that is taken into account. This property of the classical theories makes them problem-dependent, and hence their application field is limited. On the other hand, CUF is based on a displacement field obtained in a unified manner, and then every theory order can be reached.

In this section, the unified formulation is given at first, and then finite elements are used to obtain the "fundamental nuclei" and all the matrices needed.

2.2.1 Unified formulation

In order to achieve an unified formulation of the beam cross-section, the displacement field is written as follows:

$$\mathbf{u}(x, y, z) = F_s(x, z)\mathbf{u}_s(y), \quad s = 1, 2, \dots, M \quad (2.3)$$

where F_s are functions of the coordinates x and z on the cross-section, \mathbf{u}_s is the displacement vector along the beam axis, and M stands for the number of the terms used in the expansion. The repeated subscript s indicates summation. By choosing different F_s functions one can decide the order of the model; for example, if a second order model is chosen, eq. (2.3) can be written as:

$$\begin{aligned} u_x &= u_{x_1} + xu_{x_2} + zu_{x_3} + x^2u_{x_4} + xzu_{x_5} + z^2u_{x_6} \\ u_y &= u_{y_1} + xu_{y_2} + zu_{y_3} + x^2u_{y_4} + xzu_{y_5} + z^2u_{y_6} \\ u_z &= u_{z_1} + xu_{z_2} + zu_{z_3} + x^2u_{z_4} + xzu_{z_5} + z^2u_{z_6} \end{aligned}$$

In this case $M = 6$ and there are 18 different displacement variables. Note that one can find the particular cases of Euler-Bernoulli and Timoshenko displacements fields simply by using an appropriate set of F_s functions.

2.2.2 Finite element formulation

Through a finite element formulation, the weak form of the governing equations can be obtained. Let us begin the study introducing the nodal displacement vector:

$$\mathbf{q}_{sj} = \left\{ \begin{matrix} q_{u_{x_{sj}}} & q_{u_{y_{sj}}} & q_{u_{z_{sj}}} \end{matrix} \right\}^T \quad s = 1, 2, \dots, M \quad j = 1, 2, \dots, N_{EN} \quad (2.4)$$

Here the subscript j indicates the element node, and N_{EN} the number of nodes per element. Note that the element considered now is a beam element along the longitudinal y-axis. This displacement variables are interpolated along the y-axis by means of the shape functions N_j , obtaining:

$$\mathbf{u} = N_j(y)F_s(x, z)\mathbf{q}_{sj} \quad j = 1, 2, \dots, p + 1 \quad (2.5)$$

where p is the order of the shape functions. The complete form of the shape functions can be found in [3]. It is important to underline that, whatever the shape functions are, they are always independent of the cross-section polynomials F_s . In the analysis presented in the following chapters, for example, are usually adopted B4 elements for the longitudinal mesh (third-order shape functions) and L9 (Lagrange polynomials with 9 points) elements on the cross-section. For further information about the LE beam theories the readers can use as reference [8] and [6].

In order to derive the fundamental nuclei of the CUF theory the PVD is applied. It states that *the sum of all the virtual work done by the internal and external forces existing in the system in any arbitrary infinitesimal virtual displacements satisfying the prescribed geometrical constraints is zero* [31]. This can be written as:

$$\delta L_{int} - \delta L_{ext} = 0 \quad (2.6)$$

where L_{int} is the strain energy, and L_{ext} is the work of the external forces. If eqs. (2.3), (2.5) and (2.6) are used, the following expression is derived:

$$\mathbf{K}_S^{ij\tau s} \mathbf{q}_{sj} - \mathbf{p}_{sj} = 0 \quad (2.7)$$

$\mathbf{K}_S^{ij\tau s}$ is the fundamental nucleus (FN) of the secant stiffness matrix, whereas \mathbf{p}_{sj} is the FN of the loading vector. The fundamental nuclei must be assembled during

the expansion in order to obtain the global matrices, as in the expression:

$$\mathbf{K}_S \mathbf{q} - \mathbf{p} = 0 \quad (2.8)$$

Thus, the purpose of the following sections is to explain how the secant stiffness matrix and the loading vector are created; once they are assembled, the nodal unknowns can be computed by means of eq.(2.8).

2.2.3 Secant stiffness matrix

For the derivation of the secant stiffness matrix FN the expression of the virtual variation of the strain energy must be taken into account:

$$\delta L_{int} = \langle \delta \boldsymbol{\epsilon}^T \boldsymbol{\sigma} \rangle \quad (2.9)$$

Hereafter it is defined $\langle (\cdot) \rangle = \int_V (\cdot) dV$; V is the initial volume of the beam structure.

The purpose now is to express the integral argument in terms of nodal unknowns. Remembering the expression of the strains in (2.2) and using the unified formulation introduced in eq. (2.5) one can write:

$$\boldsymbol{\epsilon} = (\mathbf{B}_l^{sj} + \mathbf{B}_{nl}^{sj}) \mathbf{q}_{sj} \quad (2.10)$$

\mathbf{B}_l^{sj} and \mathbf{B}_{nl}^{sj} are differential operators matrix which contains functions of \mathbf{u} , \mathbf{F}_s and \mathbf{N}_j and their derivatives. The first has got the linear terms only, while the second the non-linear ones. Their full form can be seen in [22]. As it is necessary to have the virtual variation of the strains vector, the following step is to write:

$$\delta \boldsymbol{\epsilon} = (\mathbf{B}_l^{\tau i} + 2\mathbf{B}_{nl}^{\tau i}) \delta \mathbf{q}_{\tau i} \quad (2.11)$$

And thus:

$$\delta \boldsymbol{\epsilon}^T = \delta \mathbf{q}_{\tau i}^T (\mathbf{B}_l^{\tau i} + 2\mathbf{B}_{nl}^{\tau i})^T \quad (2.12)$$

Here the apexes τ and i are used in order to differentiate this equation from the one written for the stress vector; in fact, remembering the constitutive equation

of the material (2.1) one can also write:

$$\boldsymbol{\sigma} = \mathbf{C}(\mathbf{B}_l^{sj} + \mathbf{B}_{nl}^{sj})\mathbf{q}_{sj} \quad (2.13)$$

Thus, substituting eqs. (2.12) and (2.13) in eq. (2.9) the result is:

$$\begin{aligned} \delta L_{int} &= \delta \mathbf{q}_{\tau i}^T \langle (\mathbf{B}_l^{\tau i} + 2\mathbf{B}_{nl}^{\tau i})^T \mathbf{C}(\mathbf{B}_l^{sj} + \mathbf{B}_{nl}^{sj}) \rangle \mathbf{q}_{sj} \\ &= \delta \mathbf{q}_{\tau i}^T \mathbf{K}_0^{ij\tau s} \mathbf{q}_{sj} + \delta \mathbf{q}_{\tau i}^T \mathbf{K}_{lnl}^{ij\tau s} \mathbf{q}_{sj} + \delta \mathbf{q}_{\tau i}^T \mathbf{K}_{nll}^{ij\tau s} \mathbf{q}_{sj} + \delta \mathbf{q}_{\tau i}^T \mathbf{K}_{nlnl}^{ij\tau s} \mathbf{q}_{sj} \\ &= \delta \mathbf{q}_{\tau i}^T \mathbf{K}_S^{ij\tau s} \mathbf{q}_{sj} \end{aligned} \quad (2.14)$$

The secant stiffness matrix \mathbf{K}_S is then the sum of four different matrices:

$$\mathbf{K}_S^{ij\tau s} = \mathbf{K}_0^{ij\tau s} + \mathbf{K}_{lnl}^{ij\tau s} + \mathbf{K}_{nll}^{ij\tau s} + \mathbf{K}_{nlnl}^{ij\tau s} \quad (2.15)$$

These matrices represent, respectively, the linear component, the two non-linear components of order 1, and the non-linear component of order 2. They are given in terms of *fundamental nuclei*, and are the result of:

$$\begin{aligned} \mathbf{K}_0^{ij\tau s} &= \langle (\mathbf{B}_l^{\tau i})^T \mathbf{C} \mathbf{B}_l^{sj} \rangle \\ \mathbf{K}_{lnl}^{ij\tau s} &= \langle (\mathbf{B}_l^{\tau i})^T \mathbf{C} \mathbf{B}_{nl}^{sj} \rangle \\ \mathbf{K}_{nll}^{ij\tau s} &= 2 \langle (\mathbf{B}_{nl}^{\tau i})^T \mathbf{C} \mathbf{B}_l^{sj} \rangle \\ \mathbf{K}_{nlnl}^{ij\tau s} &= 2 \langle (\mathbf{B}_{nl}^{\tau i})^T \mathbf{C} \mathbf{B}_{nl}^{sj} \rangle \end{aligned} \quad (2.16)$$

The elemental secant stiffness matrix can be obtained, once the F_τ functions are chosen, by expanding the indexes $\tau, s = 1, \dots, M$ and $i, j = 1, \dots, p+1$. After this expansion, the global stiffness matrix is obtained in the classical way of FEM. This method is explained for example in [6].

2.2.4 Loading vector

In order to obtain the loading vector \mathbf{p}_{sj} the expression of the external virtual work must be taken into account. Given a concentrated load \mathbf{P} applied in one of the nodes of the structures, as it is always done in the next analysis, the external virtual work is:

$$\delta L_{ext} = \mathbf{P} \delta \mathbf{u}^T \quad (2.17)$$

With the CUF formulation of eq. (2.5) the virtual work can be written in terms of the nodal unknowns vector:

$$\delta L_{ext} = F_s N_j \mathbf{P} \delta \mathbf{q}_{sj}^T \quad (2.18)$$

Thus, the loading vector *fundamental nucleus* is given by:

$$\mathbf{p}_{sj} = F_s N_j \mathbf{P} \quad (2.19)$$

In a similar way to what was done for the secant stiffness matrix, the elemental loading vector is obtained by expanding the indexes $s = 1, \dots, M$ and $j = 1, \dots, p+1$, and then the global loading vector with the classical FEM theory.

For a different load distribution [7] can be seen as a reference.

2.3 Non-linear analysis

The non-linear analysis is presented here using the Newton-Raphson method [24], and Crisfield arc-length method [9]. In the end, the analytical derivation of the tangent stiffness matrix is given.

2.3.1 Newton-Raphson linearization

The starting point is eq. (2.8), which can be reformulated as:

$$\boldsymbol{\varphi}_{res} \equiv \mathbf{K}_S \mathbf{q} - \mathbf{p} = 0 \quad (2.20)$$

Here $\boldsymbol{\varphi}_{res}$ represents the residual nodal forces vector; it is the parameter which must be set the closest possible to zero in order to obtain the equilibrium solution. This last equation can be linearized using a Taylor's series expansion of $\boldsymbol{\varphi}_{res}$ stopped at the first-order terms:

$$\boldsymbol{\varphi}_{res}(\mathbf{q} + \delta \mathbf{q}, \mathbf{p} + \delta \mathbf{p}) = \boldsymbol{\varphi}_{res}(\mathbf{q}, \mathbf{p}) + \frac{\partial \boldsymbol{\varphi}_{res}}{\partial \mathbf{q}} \delta \mathbf{q} + \frac{\partial \boldsymbol{\varphi}_{res}}{\partial \mathbf{p}} \delta \lambda \mathbf{p}_{ref} = 0 \quad (2.21)$$

The loading vector \mathbf{p} is been written as $\mathbf{p} = \lambda \mathbf{p}_{ref}$, where λ is the load parameter. Moreover, $\frac{\partial \boldsymbol{\varphi}_{res}}{\partial \mathbf{q}} = \mathbf{K}_T$ is the tangent stiffness matrix, and $-\frac{\partial \boldsymbol{\varphi}_{res}}{\partial \mathbf{p}}$ is equal to the

identity matrix. Thus, eq. (2.21) can be simplified and the compact form is:

$$\mathbf{K}_T \delta \mathbf{q} = \delta \lambda \mathbf{p}_{ref} - \boldsymbol{\varphi}_{res} \quad (2.22)$$

An additional constraint relationship must be written in order to solve this equation, as the load parameter is a variable itself. Thus, the complete system is:

$$\begin{cases} \mathbf{K}_T \delta \mathbf{q} = \delta \lambda \mathbf{p}_{ref} - \boldsymbol{\varphi}_{res} \\ c(\delta \mathbf{q}, \delta \lambda) = 0 \end{cases} \quad (2.23)$$

Different constraint relationships lead to different incremental methods: for example, if the constraint is $\delta \lambda = 0$ eq. (2.23) represents a load-control method, and if it is $\delta \mathbf{q} = 0$ is a displacement-control method. These two methods, together with the path-following one, are briefly depicted in Fig. 2.1.

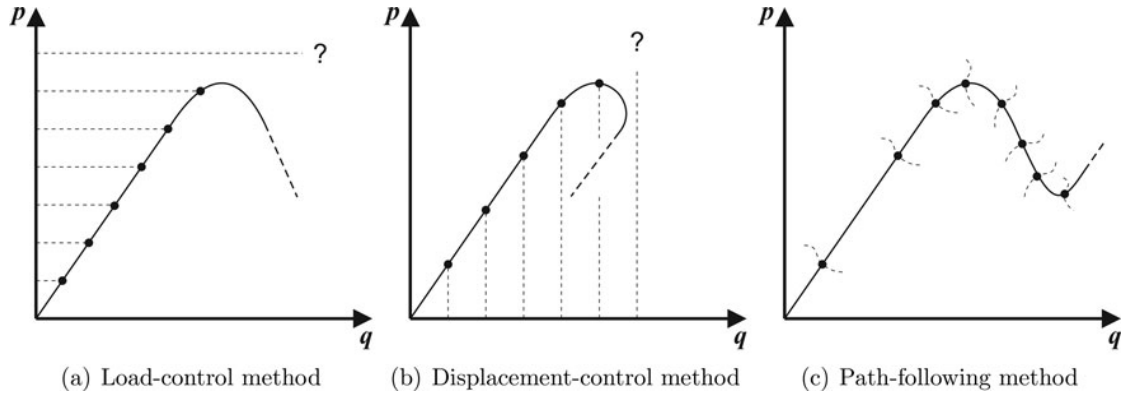


Figure 2.1: Non-linear analysis control methods [5]

2.3.2 Crisfield arc-length method

The Crisfield arc-length method, adopted for all the non-linear analysis of the next chapters, is of the "path-following" kind, and the constraints relationship contains both load and displacement variation controls. This is the best way to obtain equilibrium curves with very non-linear shapes, such as snap-backs. In order to understand how this method works, the reader must have a look at Fig. 2.2.

In this figure, the subscript m indicates the global iteration, and the apex n the local one. This means that the analysis is formed by a series of global iterations (or

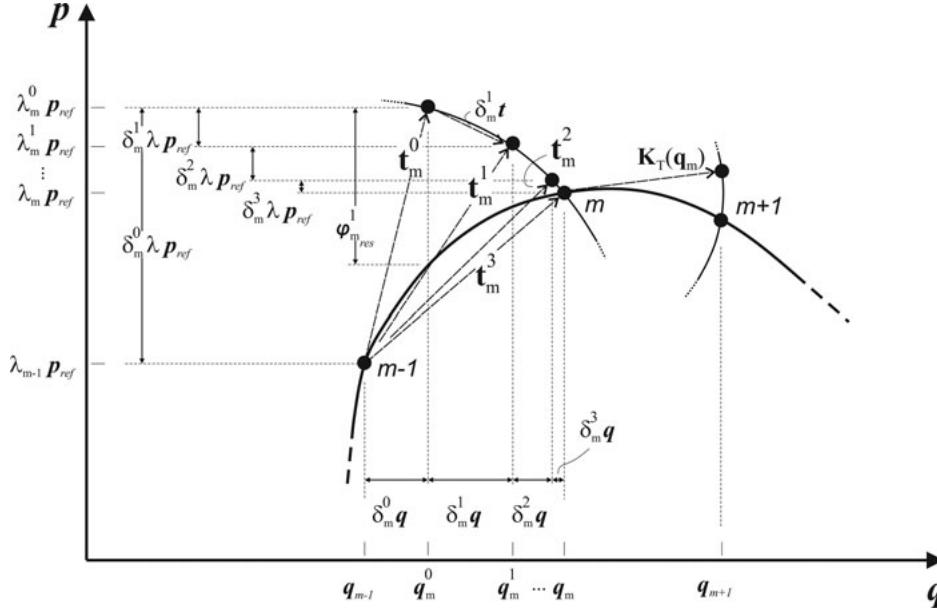


Figure 2.2: Crisfield arc-length method [22]

load steps) that identify a first solution, $\delta_m^0 \mathbf{q}$; then, a second inner iteration makes converge the solution toward the equilibrium curve, by solving eq. (2.23). Once the residual nodal forces vector is small enough, a new global iteration is made, and the process restarts. The global iterations are made using the tangent stiffness matrix: the first attempt to find the m -step equilibrium point is made along the tangent to the $(m-1)$ -step solution. The vector that connects the solution of one step to the solution of the next step is indicated with \mathbf{t} , and so the first attempt to find the equilibrium point of the m -step is made through the \mathbf{t}_m^0 vector.

The constraints relationship corresponds to a multi-dimensional sphere with radius equal to the initial arc-length value Δl_m^0 . This means that the modulus of the vector \mathbf{t} is equal to the square of the initial arc-length, and then eq. (2.23) for the Crisfield arc-length method transforms into:

$$\begin{cases} \mathbf{K}_T \delta \mathbf{q} = \delta \lambda \mathbf{p}_{ref} - \boldsymbol{\varphi}_{res} \\ \mathbf{t}_m^{nT} \mathbf{t}_m^n = (\Delta l_m^0)^2 \end{cases} \quad (2.24)$$

For further details about the strategies adopted to preserve symmetric solvers the reader is directed to [22].

2.3.3 Tangent stiffness matrix

The solution of eq. (2.24) requires the knowledge of the tangent stiffness matrix \mathbf{K}_T . That is obtained from the linearization of the virtual variation of the strain energy, as follows:

$$\begin{aligned}
\delta(\delta L_{int}) &= \langle \delta(\delta \boldsymbol{\epsilon}^T \boldsymbol{\sigma}) \rangle \\
&= \langle \delta \boldsymbol{\epsilon}^T \delta \boldsymbol{\sigma} \rangle + \langle \delta(\delta \boldsymbol{\epsilon}^T) \boldsymbol{\sigma} \rangle \\
&= \delta \mathbf{q}_{\tau i}^T (\mathbf{K}_0^{ij\tau s} + \mathbf{K}_{T_1}^{ij\tau s} + \mathbf{K}_{\sigma}^{ij\tau s}) \delta \mathbf{q}_{s j} \\
&= \delta \mathbf{q}_{\tau i}^T \mathbf{K}_T^{ij\tau s} \delta \mathbf{q}_{s j}
\end{aligned} \tag{2.25}$$

Thus, the tangent stiffness matrix *fundamental nucleus* is given by the sum of three different matrices:

$$\mathbf{K}_T^{ij\tau s} = \mathbf{K}_0^{ij\tau s} + \mathbf{K}_{T_1}^{ij\tau s} + \mathbf{K}_{\sigma}^{ij\tau s} \tag{2.26}$$

where $\mathbf{K}_0^{ij\tau s}$ is the linear component, the same of eq. (2.16), and the other two matrices are the non-linear components. In order to obtain the expression for $\mathbf{K}_{T_1}^{ij\tau s}$ and $\mathbf{K}_{\sigma}^{ij\tau s}$ too, the second line of eq. (2.25) must be developed more. The virtual variation of the stress vector is present in the first term, and can be expressed, remembering eq. (2.11), as:

$$\delta \boldsymbol{\sigma} = \delta(\mathbf{C}\boldsymbol{\epsilon}) = \mathbf{C}\delta\boldsymbol{\epsilon} = \mathbf{C}(\mathbf{B}_l^{sj} + 2\mathbf{B}_{nl}^{sj})\delta \mathbf{q}_{s j} \tag{2.27}$$

And hence, considering the first term of the second line of eq. (2.25), one has:

$$\begin{aligned}
\langle \delta \boldsymbol{\epsilon}^T \delta \boldsymbol{\sigma} \rangle &= \delta \mathbf{q}_{\tau i}^T \langle (\mathbf{B}_l^{\tau i} + 2\mathbf{B}_{nl}^{\tau i})^T \mathbf{C}(\mathbf{B}_l^{sj} + 2\mathbf{B}_{nl}^{sj}) \rangle \delta \mathbf{q}_{s j} \\
&= \delta \mathbf{q}_{\tau i}^T \mathbf{K}_0^{ij\tau s} \mathbf{q}_{s j} + \delta \mathbf{q}_{\tau i}^T (2\mathbf{K}_{lnl}^{ij\tau s}) \mathbf{q}_{s j} + \delta \mathbf{q}_{\tau i}^T \mathbf{K}_{nll}^{ij\tau s} \mathbf{q}_{s j} + \delta \mathbf{q}_{\tau i}^T (2\mathbf{K}_{nlnl}^{ij\tau s}) \mathbf{q}_{s j} \\
&= \delta \mathbf{q}_{\tau i}^T (\mathbf{K}_0^{ij\tau s} + \mathbf{K}_{T_1}^{ij\tau s}) \delta \mathbf{q}_{s j}
\end{aligned} \tag{2.28}$$

Thus, $\mathbf{K}_{T_1}^{ij\tau s}$ is a linear combination of three of the matrices already encountered in eq. (2.16):

$$\mathbf{K}_{T_1}^{ij\tau s} = 2\mathbf{K}_{lnl}^{ij\tau s} + \mathbf{K}_{nll}^{ij\tau s} + 2\mathbf{K}_{nlnl}^{ij\tau s} \tag{2.29}$$

The $\mathbf{K}_{\sigma}^{ij\tau s}$ matrix is evaluated operating on the term $\langle \delta(\delta \boldsymbol{\epsilon}^T) \boldsymbol{\sigma} \rangle$. The full

demonstration is not reported here and can be find in [22]; let's just say that the final form is:

$$\mathbf{K}_{\sigma}^{ij\tau s} = \mathbf{K}_{\sigma_l}^{ij\tau s} + \mathbf{K}_{\sigma_{nl}}^{ij\tau s} = \langle \text{diag}((\mathbf{B}_{nl}^*)^T(\boldsymbol{\sigma}_l + \boldsymbol{\sigma}_{nl})) \rangle \quad (2.30)$$

where $\boldsymbol{\sigma}_l = \mathbf{C}\boldsymbol{\epsilon}_l$ and $\boldsymbol{\sigma}_{nl} = \mathbf{C}\boldsymbol{\epsilon}_{nl}$. It is a diagonal matrix composed by the elements of the vector $(\mathbf{B}_{nl}^*)^T(\boldsymbol{\sigma}_l + \boldsymbol{\sigma}_{nl})$.

Given the *fundamental nucleus* $\mathbf{K}_T^{ij\tau s}$, as already done for the secant stiffness matrix and the loading vector, the elemental tangent stiffness matrix is obtained by expanding the indexes $\tau, s = 1, \dots, M$ and $i, j = 1, \dots, p + 1$. Then, the global \mathbf{K}_T is given by the classical FEM theory.

Chapter 3

Preliminary results

In this chapter, the non-linear analyses of some preliminary cases are introduced. The problems that are here exposed are presented in ascending order of difficulty: at first, a simple beam with a square cross-section is analyzed, then the cross-section is transformed into a "C", and at last, some holes are made along the C-Beam length.

In some cases, in addition to the usual CUF analysis, other analyses involving Abaqus are performed.

3.1 Square Beam

The following analysis has as objective the study of the non-linear behavior of a classical cantilever beam with a square cross-section. As a literature reference, the work of Pagani and Carrera can be seen [22].

The beam geometry is showed in Fig. 3.1 and its related properties are listed below:

- $L = 100 \text{ mm}$;
- $h = 10 \text{ mm}$;
- $E = 75000 \text{ Mpa}$;
- $\nu = 0.33$
- $I = \frac{h^4}{12} = 833.3333 \text{ mm}^4$.

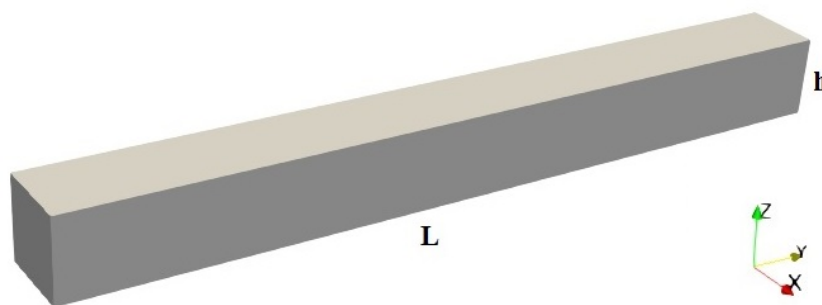


Figure 3.1: Cantilever square beam geometry. L is the length, h the height

As one can see, the beam has got a square cross-section with side equal to h , and its length is denoted with L . E and I are respectively the Young modulus and the inertia momentum of the cross-section.

The beam is clamped at one edge and free at the opposite one; in this case, the free edge is the one with the outgoing y -axis, i.e., the one located at $y = 100 \text{ mm}$ (on the right in Fig. 3.1).

This particular cantilever beam has a length-to-height ratio equal to $\frac{L}{h} = 10$, then it can be classified reasonably as short, and a non-linear analysis is much more essential. In fact, in the case of slender beams, the classical Euler-Bernoulli theory can approximate the real beam behavior for a much more extensive range of deflection, but for short beams, this is no longer true.

3.1.1 CUF Model

This section presents the CUF model adopted for the current analysis.

Material

For this analysis, only one material needs to be created; its properties are shown in Tab. 4.1.

$E(MPa)$	ν
$75 \cdot 10^3$	0.33

Table 3.1: Square beam material properties

As this analysis deals with an isotropic and homogeneous material, the lamination matrix has only one element as well.

Nodes

The current analysis is made using 20 B4 elements along the y -axis of the beam. Thus, a total amount of 61 nodes are present along the longitudinal length of the beam. The 61 nodes are enumerated in ascending order starting from the one at $y = 0$, which is #1, until the one at $y = 100$, which is #61. This simple formula gives the coordinate of the N -th node:

$$y(N) = \frac{L}{60}(N - 1)$$

The number of elements adopted is the same as the one used in literature [22]. In this way, a direct comparison can be made.

Mesh

A single $L9$ element has accomplished the cross-section meshing. Thus, the total amount of nodes along the whole structure is equal to:

$$N^{\circ} \text{ nodes} = 9 \cdot 61 = 549$$

Each node has got 3 degrees of freedom (i.e., displacements along the three axes), then:

$$N^{\circ} \text{ DOF} = 3 \cdot 549 = 1647$$

This meshing is the same as in literature, too [22].

BCs and Loads

Since the problem deals with a clamped-free beam, the displacements of all the nodes located in the plane $y = 0$ must be set at zero. Meanwhile, a concentrated force is applied in the central node of the cross-section in the plane $y = 100$, pointing toward the positive z -direction. The intensity of the force is variable during the non-linear analysis, and the initial value is given later in Sec. 3.1.2.

3.1.2 Analysis

A non-linear static analysis (sol. 108) is elaborated.

Taking as a reference the analysis made previously on the same problem by Pagani and Carrera [22], an initial load step equal to $p_{ref} = 1250 \text{ N}$ was chosen. In this way, the dimensionless load is, remembering the geometry values given in Sec.3.1, $\frac{p_{ref}L^2}{EI} = 0.2$. p_{ref} is the value of the force introduced in Sec. 3.1.1 and, as will be clearer later, looking at the results, it is small enough to obtain a smooth load-deflection curve.

Before starting the non-linear analysis, it is recommended first to try the code by launching a linear analysis (sol.101). In this way, it can immediately be seen whether the input files regarding the geometry and the BCs have been written correctly; moreover, by looking at the *Connectivity* file, the number of the DOF to be monitored during the non-linear analysis can be easily found. In order to make this linear analysis, a load equal to $P = 18750 \text{ N}$ was chosen, corresponding to a dimensionless load of $\frac{PL^2}{EI} = 3$.

In the section concerning the results, both kinds of analysis are taken into account.

3.1.3 Results

This section deals with the results of the previously described analysis.

Under the effect of the growing load introduced in Sec. 3.1.2, the cantilever beam deflects in the way shown in Fig. 3.2. There can be seen that a huge deflection is reached in the last step of the analysis.

More details about the load-displacement curve are represented in Fig.3.3. It shows the results of both the linear and non-linear analysis made, together with an analytical reference one based on Euler-Bernoulli beam model [4]. The displacement and the load are made dimensionless in order to stay the most generic possible.

By looking at the graphic, an extreme similarity between each of the non-linear solutions can be seen: the yellow line representing the current Mul² solution is very close to the reference model for all the curve path. Moreover, the simple linear analysis can predict well the displacement for small deflections.

In conclusion, this analysis has confirmed the ability of the CUF theory to deal



Figure 3.2: Deformed shape for three different load values - square beam

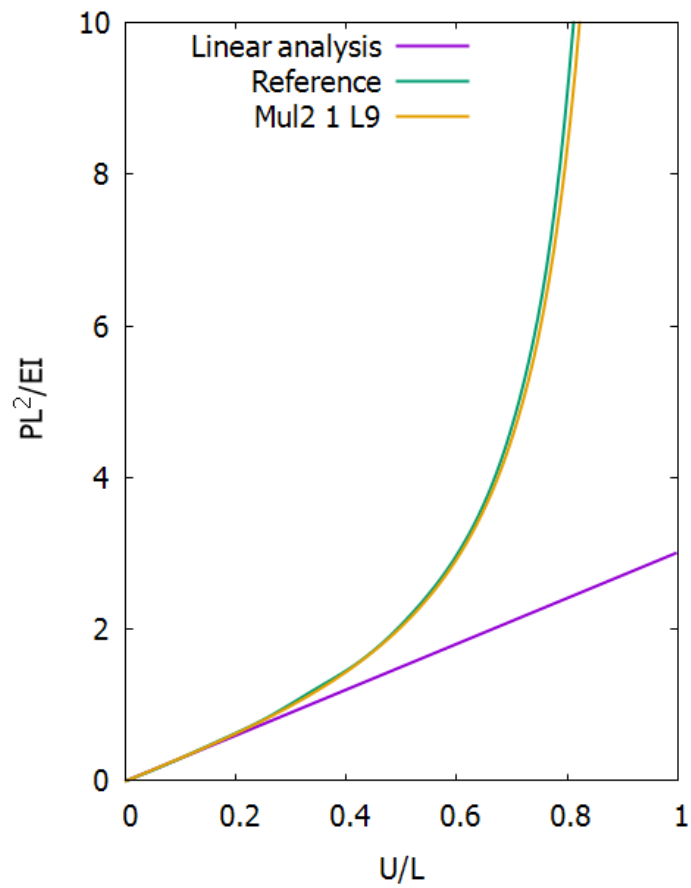


Figure 3.3: Square beam load-deflection curve, reference from [4]

with classical beam problems for both linear and non-linear cases. In fact, the solution obtained here perfectly reflects the analytical solution based on Euler-Bernoulli beam model.

3.2 C-Beam

This section deals with the non-linear analysis of a cantilever beam with a C-shaped cross-section. The aim of this study is the comparison between the load-deflection curve obtained by an Abaqus model and by a CUF model. Moreover, different kinds of elements are used in Abaqus in order to see how the solutions change.

Two different length-to-height ratios are adopted, too, in order to show also how the CUF model works with either short or long beams. Actually, $\frac{L}{h} = 3$ and $\frac{L}{h} = 30$ geometries are considered.

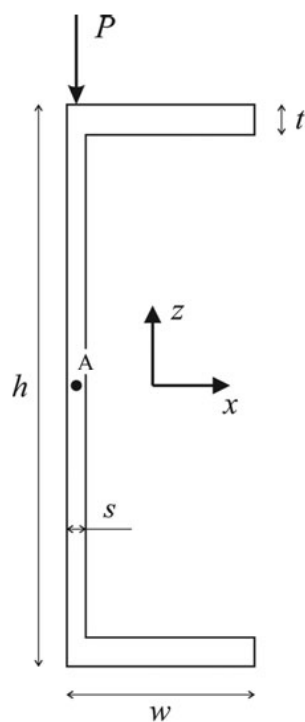


Figure 3.4: C-beam cross-section. Points for load application and displacement monitoring are included

The cross-section, which is the same for both the length-to-height ratios, is showed in Figure 3.4. The dimensions of all parameters are reported below:

- $h = 30 \text{ cm}$
- $w = 10 \text{ cm}$
- $t = 1.6 \text{ cm}$
- $s = 1 \text{ cm}$

Given the value of the height, the length of the beam is, for the two configurations, $L_1 = 90 \text{ cm}$ and $L_2 = 900 \text{ cm}$.

In Figure 3.4 the applied load P is also visible; as we can see, the force is applied along the medium plane of the vertical face (please note that in case of shell elements the medium plane coincides with the face itself), and points toward the negative z-direction. Moreover, the point A represents the node used for the displacement measurement.

Finally, the material adopted for the beam is such that $E = 21,000 \text{ kN/cm}^2$ and $\nu = 0.3$.

3.2.1 Abaqus model

As already anticipated in Section 3.2, the current Abaqus analysis is carried out employing two different types of elements: solid and shell. The utilization of solid elements usually produces a better solution than the one which can be obtained by shell elements, but a more expensive analysis is needed in terms of duration and memory occupation.

In the following, the subdivision of the section is made by analyzing the short and the long beam configuration separately.

Short beam ($\frac{L}{h} = 3$)

The short beam configuration holds a length of the beam equal to $L_1 = 90 \text{ cm}$. For both the solid elements and the shell elements models the mesh created is the same, and it is shown in Figure 3.5: there are ten elements for each cross-section, and 18 elements along the axial direction, for a total amount of 180 elements.

As can be reasonably seen by looking at Figure 3.5, the distance between two consecutive nodes (i.e., the dimension of an element) is the same along all the three axes. Please pay some particular attention to the fact that two elements are

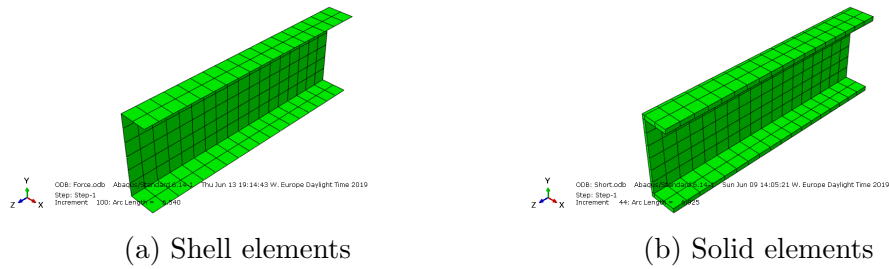


Figure 3.5: C-beam, short configuration - Shell and solid elements mesh comparison - 10x18 elements

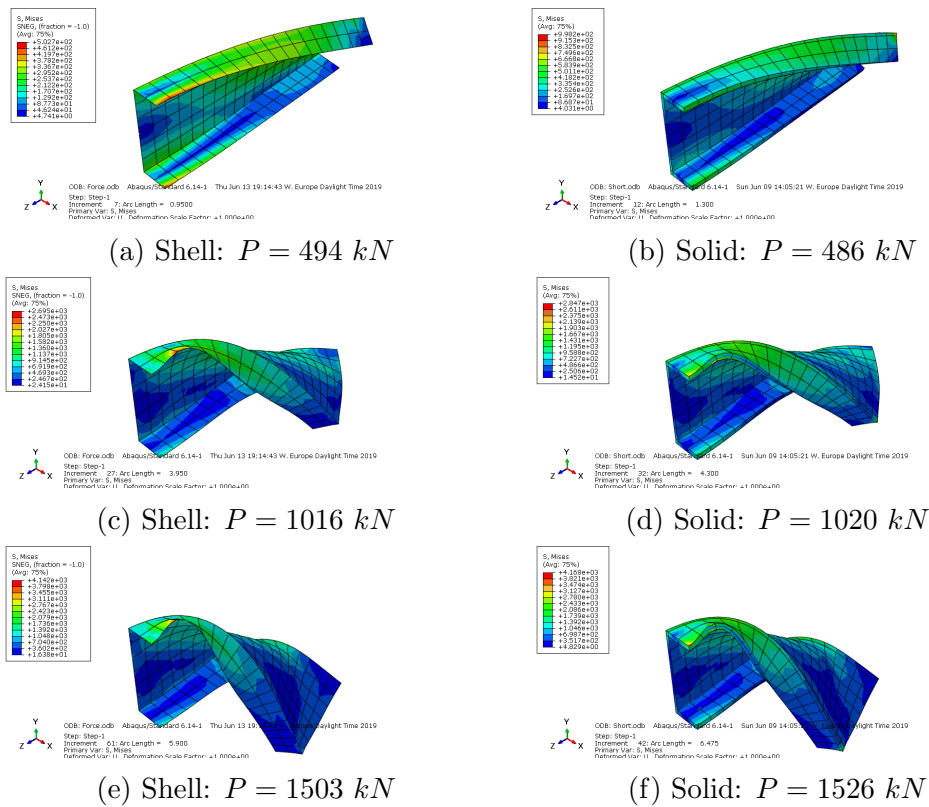


Figure 3.6: C-Beam, short configuration - Deformed shapes for different load values

present in the top and bottom faces of the cross-section; this, as will be seen, is a finer choice for the mesh than the one adopted for the CUF model as will be discussed later in Section 3.2.2.

It is commonly known that the shear center of a C-section is located, taking as reference Figure 3.4, on the left of the vertical face. It is then reasonable to foresee the deformation that the beam will have when subjected to the load: in fact, the direction of application of the load does not pass from the shear center; in this way, the beam rotates and translates simultaneously.

What has just been said is confirmed by Figure 3.6, which shows the deformed shapes of the two types of beams, subjected to growing loads.

By comparing the various figures it is possible to evaluate broadly if any differences between the shell and the solid model are encountered: this do not seem to be the case, because both models looks very similar to each other.

In Section 3.2.3 the load-deflection curve will be presented for both element types in order to understand the differences between the two models better.

Long beam ($\frac{L}{h} = 30$)

The total length of the long configuration is $L_2 = 900 \text{ cm}$. Here, unlike the previous subsection, two different meshes are used: the one adopted for the shell configuration is composed of 5 elements on the cross-section and 90 along the beam axis, whereas the solid configuration has got ten elements on the cross-section and 180 along the beam axis. In Figure 3.7, these meshes can be seen.

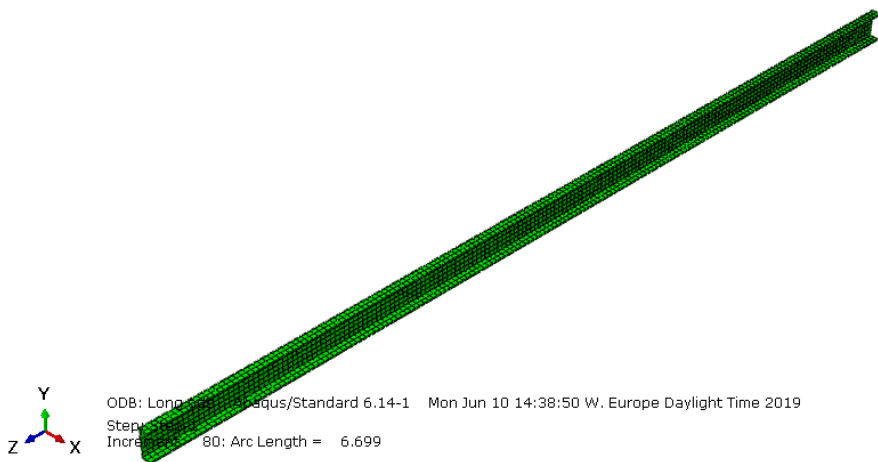
These two very different meshes will permit us to see more clearly the differences between the two types of elements. Moreover, the mesh selected for the shell configuration is as fine as the one chosen for the CUF model, and this is a further verification for that model.

For the same reasons already discussed in Section 3.2.1, the beam, when subjected to the load, will deflect and rotate. This behavior is confirmed by the deformed shapes showed in Figure 3.8.

As can be seen by looking at those figures, the solid elements beam is not as rigid as the equivalent shell elements one. In fact, when subjected to the same load, the solid elements beam rotate much more than the shell one; for example, in Figure 3.8b, the beam has already passed the buckling load, while in Figure



(a) Shell elements - 5x90 elements



(b) Solid elements - 10x180 elements

Figure 3.7: C-Beam, long configuration - Shell and solid elements mesh comparison

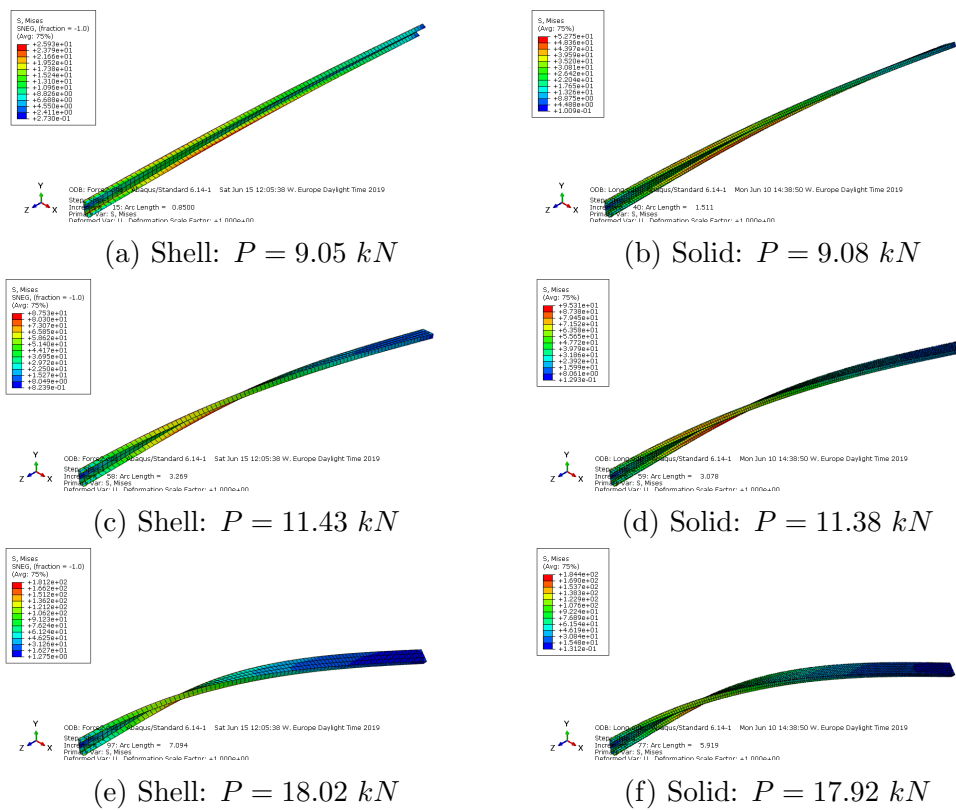


Figure 3.8: C-Beam, long configuration - Deformed shapes for different load values

3.8a the instability has not been encountered yet. This peculiar behavior will be more clearly explained later in Section 3.2.3.

3.2.2 CUF model

In this section is described the CUF model adopted for the current analysis. The main relevance is given to the explanation of the axial and cross-sectional mesh utilized.

Material

For the sake of completeness, the material features are here reported again.

$E(kN/cm^2)$	ν
$21 \cdot 10^3$	0.3

Table 3.2: C-Beam material properties

As for the material, only one lamination is adopted.

Nodes

Along the beam axis, 20 B4 elements are utilized, for a total amount of 61 nodes. The distance between each node is $d = \frac{L}{60}$. The length of the beam L is different from the short and the long beam configuration, whereas the number of nodes does not vary; this implies a finer longitudinal mesh for the short beam compared to the long one.

$$d_1 = \frac{L_1}{60} = 1.5 \text{ cm} \quad d_2 = \frac{L_2}{60} = 15 \text{ cm}$$

The following expression finally gives the coordinate along the y-axis of each node:

$$y(N) = d(N - 1) \quad N = 1, \dots, N_{nodes}$$

The finer mesh used for the short beam is compensated by the fact that, for a small length-to-height ratio, beam elements are not as accurate as for longer beams. For this reason, a finer mesh can improve the solution.

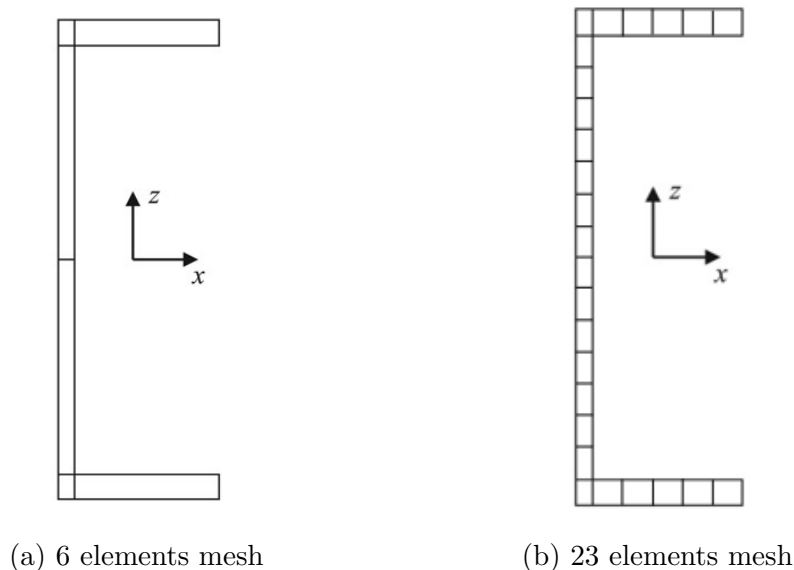
Mesh

Figure 3.9: C-Beam - Cross-section CUF meshes

The cross-section mesh initially created is showed in Figure 3.9a. Here each rectangle represents an L9 polynomial element of the mesh. As one can see, there are 6 L9 elements for a total amount of 39 nodes; furthermore, the nodes for the application of the load and the displacement measure are not explicitly visible, as they are at the center of the top borderline of their respective element. These nodes coordinates are given here:

$$\begin{array}{ll} x_P = -7 & x_A = -7 \\ z_P = 15 & z_A = 0 \end{array}$$

The mesh is finer at the corner of the section, which is probably the most peculiar part of the "C" in terms of deformations.

After a first analysis, it was found out that a too big difference appears, in the case of short beam configuration, between the CUF and Abaqus solutions (this little accurate solution is reported in Sec. 3.2.3). Thus, a convergence analysis was carried out, and a second mesh was created, as showed in Fig. 3.9b. Here 23 L9 elements are disposed on the cross-section, for a total amount of 159 nodes.

The nodes for the load application and displacement monitoring are not changed.

Loads and BCs

The concentrated force is applied, as already discussed, in point P, whose coordinates are given in Subsection 3.2.2. The intensity of the load is not a defined number, but it varies according to the non-linear analysis evolution. For the short beam configuration, its maximum value is imposed at 1700 kN , whereas for the long configuration at 18 kN .

The beam is clamped-free, hence all the nodes of the fixed section (the one at $y = 0$) have displacements and rotations imposed at zero.

Note that Figure 3.9 represents the fixed section, as the y -axis is pointing into the plane of the page; The points A and P are located on the face at $y = L$.

3.2.3 Results

In this section, the results of the analysis are finally given. At first, the short beam configuration is taken into account, and then the long configuration one.

The analyses with the CUF model are carried out using, when possible, both the old and the new version of the code MUL², but since the two curves obtained are nearly indistinguishable from each other, only one curve is represented hereafter. Precisely, the old code gave results for both the configuration, while the new code converged only for the short beam.

Note that the load and the displacement are directed toward the negative direction of the z -axis but, to simplify the visibility of the graphics and to be able to compare these results with literature, P and U_z are considered as positive (i.e., it is plotted P and $-U_z$).

Short beam ($\frac{L}{h} = 3$)

The P-U curve of the short beam is shown in Figure 3.10. The Abaqus analyses are represented by the green and purple lines, while the MUL² analysis by the blue and yellow lines. Here, as already anticipated, two CUF analyses have been carried out because convergence was not obtained with the first one.

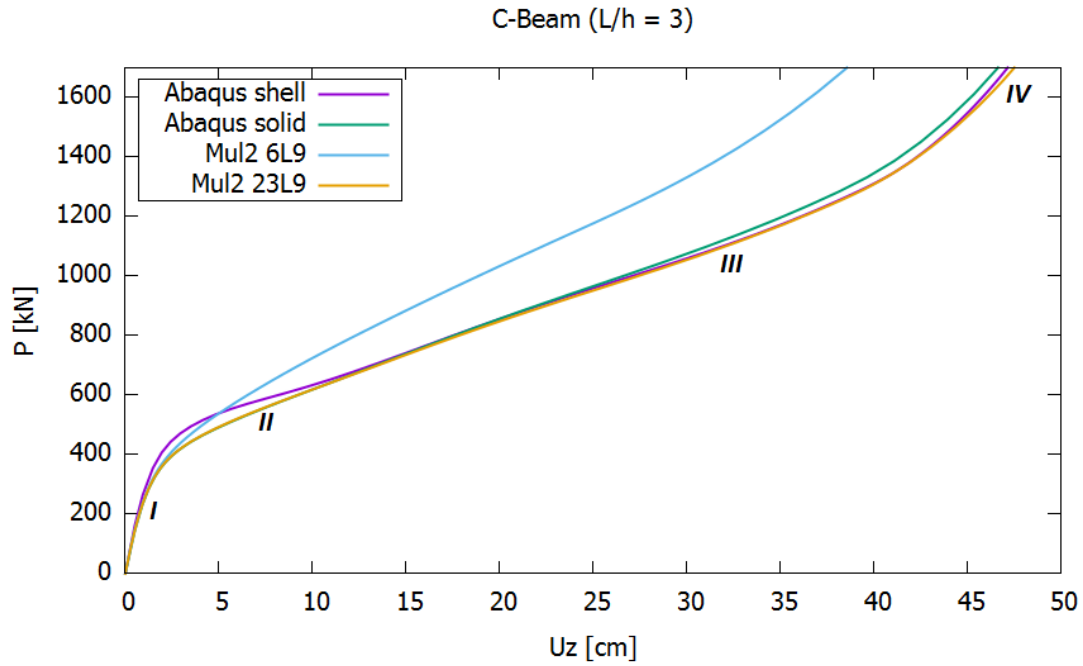


Figure 3.10: C-Beam load-deflection curve ($\frac{L}{h} = 3$)

The not-convergence of the Mul^2 analysis with six elements on the cross-section is visible in Fig. 3.10, where the blue curve is sharply apart from the others. Nevertheless, a good result is reached in the pre-buckling region, where the blue curve matches very well the Abaqus ones; thus, critical buckling load can be sufficiently well predicted with a very coarse mesh already.

On the other hand, the CUF analysis with 23 elements on the cross-section gives excellent results also in the post-buckling region. A fascinating behavior can be noted by looking carefully at the curves: the CUF solution matches the Abaqus solid one perfectly until a displacement value of about 20 *cm* and then follows the shell curve.

An evident difference may also be seen between the Abaqus shell and solid model: the structure modeled by shell elements presents a more significant buckling load than the solid elements model; moreover, the shell curve is not as smooth as the solid one in that zone.

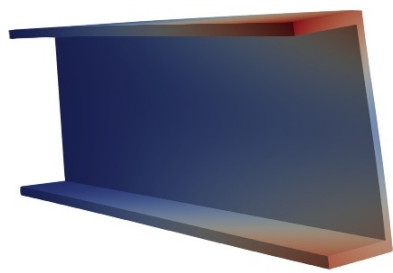
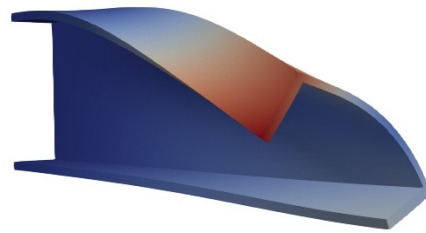
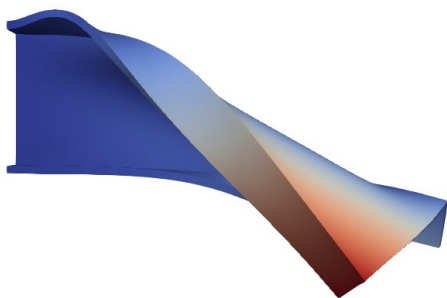
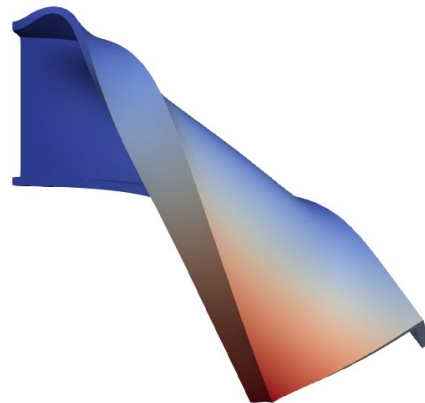
(a) Case I: $P = 200 \text{ kN}$ (b) Case II: $P = 500 \text{ kN}$ (c) Case III: $P = 1000 \text{ kN}$ (d) Case IV: $P = 1600 \text{ kN}$

Figure 3.11: C-Beam deformed CUF models

Long beam ($\frac{L}{h} = 30$)

The P-U curve of the long beam is shown in Figure 3.12. The Abaqus curves are represented by the purple and green lines, while the MUL² analysis by the blue one.

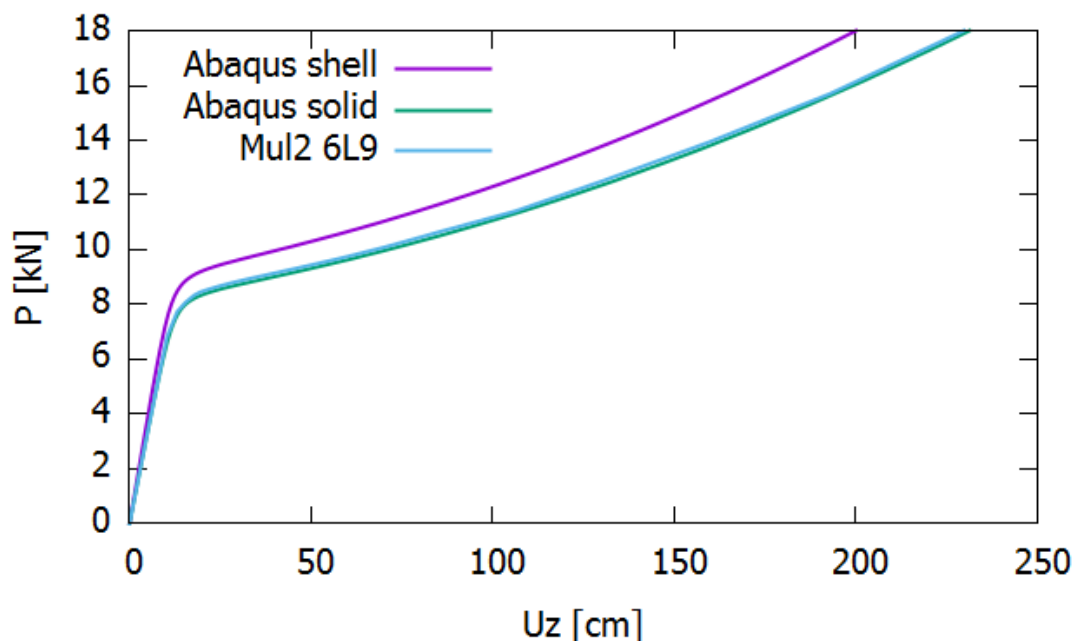


Figure 3.12: C-Beam load-deflection curve ($\frac{L}{h} = 30$)

The first thing that stands out immediately is the perfect correspondence between the CUF curve and the solid elements Abaqus curve. This is such a great result because it is demonstrated that a simple CUF model based on B4 beam elements can obtain precisely the same results as a more complex Abaqus model with solid elements, with significant savings in terms of calculation time.

The shell elements Abaqus model has the same behavior as the one already registered for the short beam in Subsection 3.2.3: the buckling load is bigger than the one obtained by the solid elements model. Apart from this difference, the curve shape is nearly the same as the other two ones.

Finally, a last comment regarding the buckling behavior shall be made: all the curves suggest a clear boundary between the linear and non-linear zone; this implies that the structure is highly rigid until the buckling load is reached, and

from that point on large deflections can be obtained for small load increments.

3.3 C-Beam with holes

This section is an evolution of the previous one, since some holes are added to the C-Beam already analyzed. Initially, the force applied to the structure is the same as the previous section, when the core of the beam was without any hole; successively, two forces are applied in the direction of the insoles (i.e., along the x-axis), simulating the folding behavior of the structure.

In fact, many deployable structures of this kind are folded using some holes disposed suitably, as can be seen in Fig. 3.13. For further information about this kind of structures, an interesting work by Mallikarachchi [17] can be used as a reference.

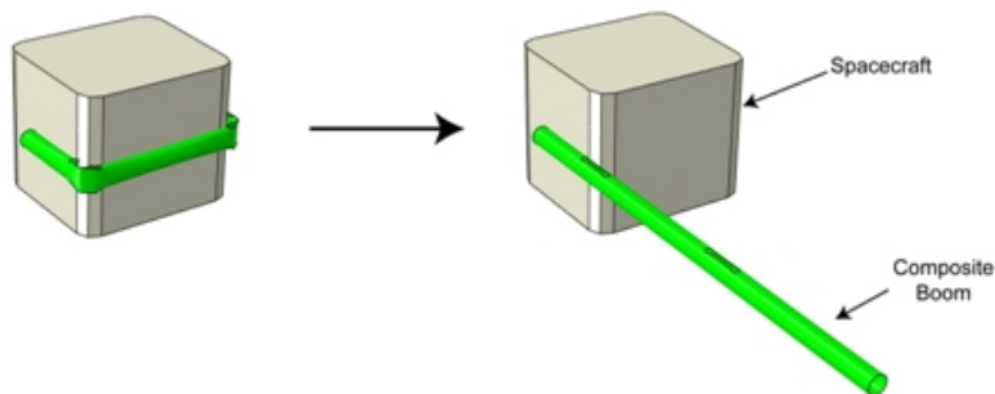


Figure 3.13: Booms unfolding [18]

A series of analyses with different loads and geometries are now presented separately.

3.3.1 Load in the plane of the core

Two analyses are performed in this section: geometry and loads are the same as in Sec. 3.2, but in the core of the beam are present either one or two holes. This is the

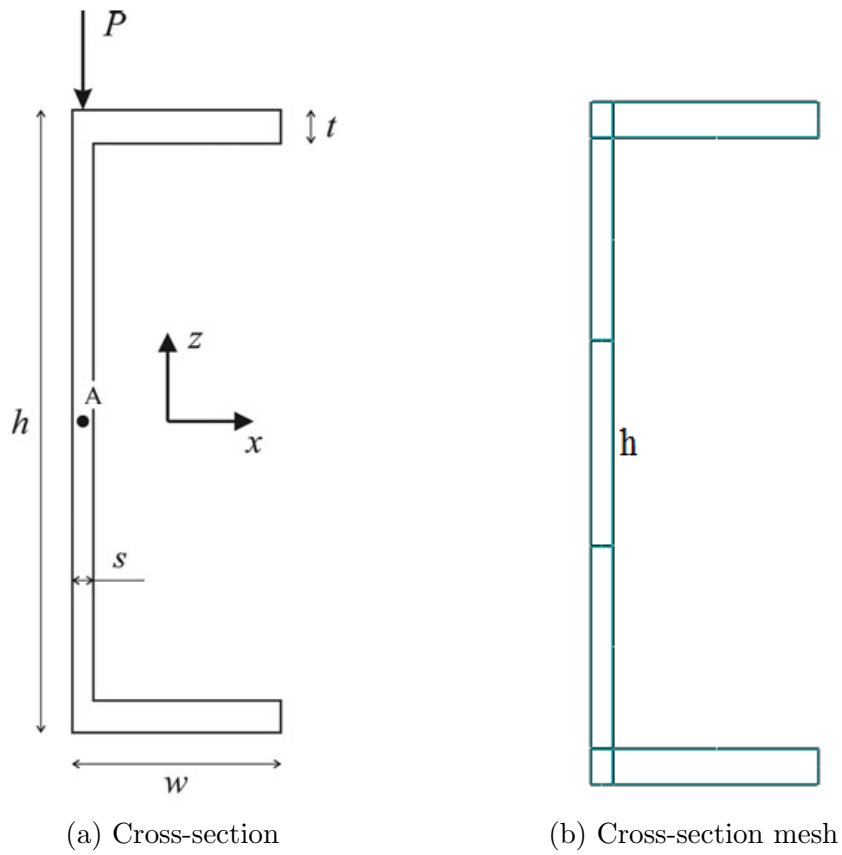
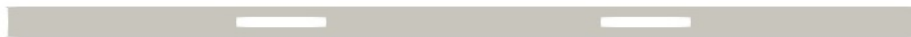


Figure 3.14: C-Beam with holes load and control point disposition (left), and cross-section mesh 7 L9 (right)



(a) C-Beam with one hole



(b) C-Beam with two holes

Figure 3.15: Holes disposition in C-Beam

plane in which the structure is most likely to work, and then a good resistance in this direction is essential. For the sake of completeness, the cross-section with the load is reported again here and is visible in Fig. 3.14a. The point of application of the load and the control point for the displacement are not varied from the previous analysis.

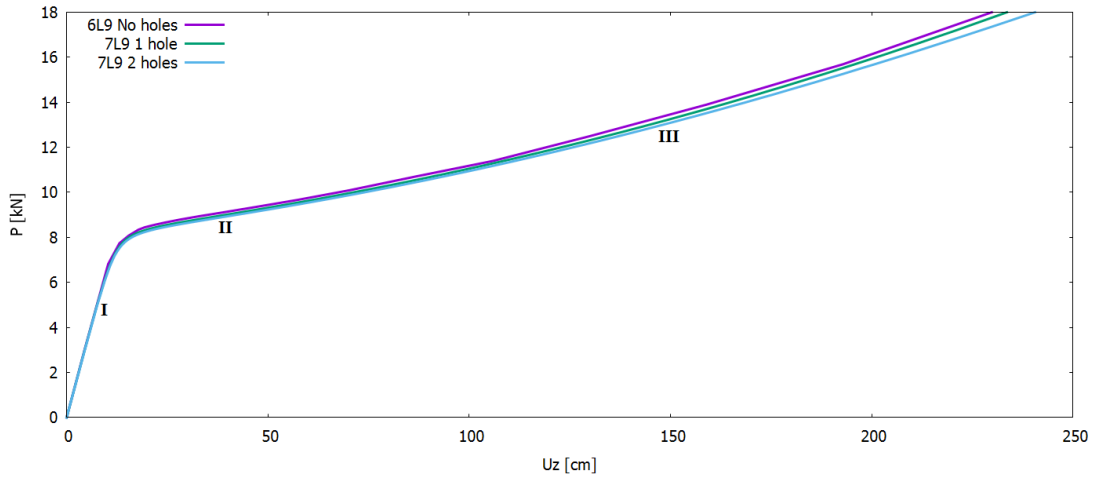


Figure 3.16: Holed C-beam equilibrium curve due to a load directed along the core direction

The mesh adopted here is a little different from the one used in Sec. 3.2, due to the presence of the hole, which requires the addition of an extra element. The mesh chosen for the cross-section is visible in Fig. 3.14b. The element denoted with the letter "h" is present in the sections without the hole, while it is absent where the hole is located; this means that the cross-section mesh is composed of 6 L9 elements where there is the hole and 7 L9 elsewhere. This is the reason why the hole dimension is the same as the dimension of the element h collocated in the center of the core and 9 *cm* high.

The position of the hole along the longitudinal axis instead is determined by which of the 20 B4 elements has got the 6 L9 cross-section mesh: in the beam with one hole, the pierced elements are the 10TH and the 11TH, while in the beam with two holes they are the 6TH, the 7TH, the 14TH and the 15TH.

The results of the non-linear analysis carried out are shown in the graph of Fig. 3.16. Here the curve named "6L9 No holes" is the same as in Fig. 3.12. The graph shows that the presence of the holes does not compromise the ability



(a) Deformed shape, case I



(b) Deformed shape, case II



(c) Deformed shape, case III

Figure 3.17: Deformed shapes of the C-Beam with two holes, load along the core direction

of the structure to withstand loads directed along the core direction. In fact, the three curves are really close to one another, and in the linear region, they are even indistinguishable. Moreover, a more marked buckling due to the presence of the holes is not visible too.

In Fig. 3.17 are visible the deformed shapes of the beam in the points indicated in the corresponding graph. The torsional-bending behavior is the same as the beam with no holes, and this confirms that the holes do not affect the correct functioning of the structure.

3.3.2 Load out of the plane of the core

The analysis carried out now deals with the lateral flexing of the C-Beam subjected to a load perpendicular to the plane of the core. Testing the behavior of the beam bending in this plane is functional to the prediction of the folding process, which is intended to take place in this way.

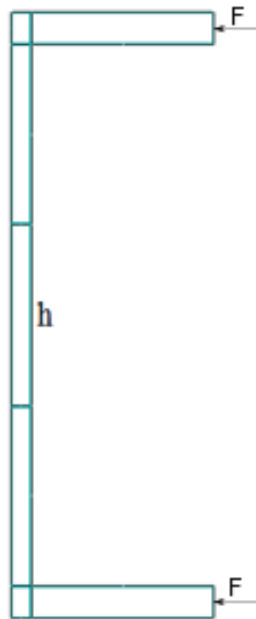


Figure 3.18: Holed C-beam cross-section mesh with lateral forces, 7L9

A total of three new analyses are presented here: C-Beam with no holes, one hole, and two holes. The mesh along the beam axis is the same as the previous section, depending on whether it is the case with one or two holes. The mesh on

the cross-section is unchanged too, but the same cannot be said for the load. Fig. 3.18 shows the position and the direction of the two applied forces, located at the free edge of the beam, i.e., the section with $y = 900 \text{ mm}$; the other edge remains with an encastre as the boundary condition. In this way, the two forces have as resultant a load passing by the symmetry axis of the cross-section, and then by the shear center; thus, a simple bending deflection, without any torsion, is foreseen.

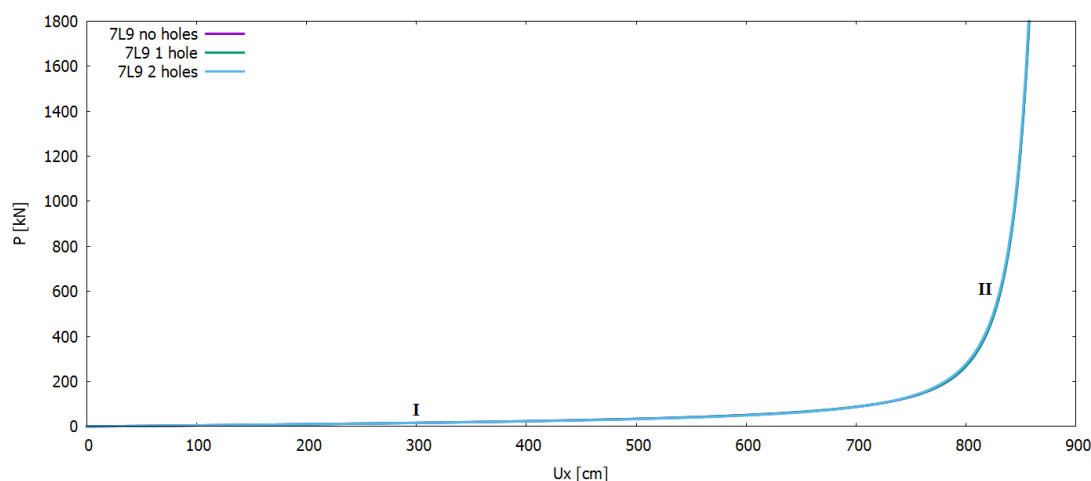


Figure 3.19: Equilibrium curve for a load directed out of the plane of the core

The equilibrium curves of the three analyses are shown in Fig. 3.19. They have a shape very similar to the load-deflection curve of the square beam analyzed in Sec. 3.1. Moreover, a perfect match is immediately detectable, as the three curves are completely overlapped and indistinguishable from one another. As it was already discovered for the square beam, a clear buckling behavior is not visible here too.

By looking at Fig. 3.20 it is immediately apparent that the deflection of the beam does not take place in the zone where one of the holes is present, but the beam merely bends itself as if the holes were not present at all. This behavior suggests that perhaps to achieve a buckling effect, one should change the loads and BCs disposition, as it will be done in the next analysis by applying a moment instead of a force at the extremity.

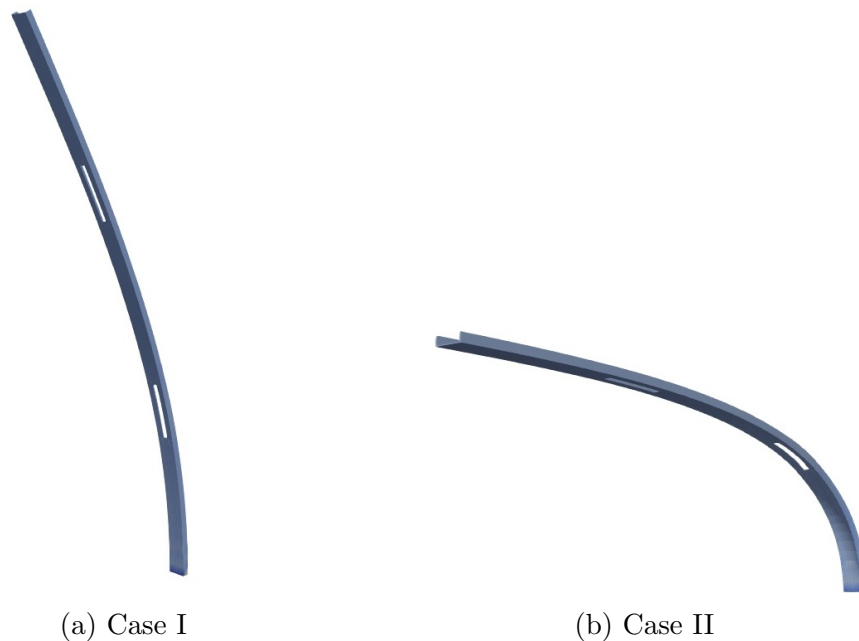


Figure 3.20: C-Beam with two holes and load directed out of the plane of the core - deformed shapes

3.3.3 Bending moments applied to the edges of the beam

The current analysis is a bit different from the last two described ones: the BCs are no more the ones for a clamped-free beam but, as already done in chapter 4.1, the beam is only able to rotate around the x-axis in one edge, and also to translate along the y-axis in the other one. In order to achieve these BCs, some nodes on the two cross-sections of the extremities have some DOF blocked, as it will be explained shortly. The main reason why this analysis is done is that with the previous two ones the buckling configuration was not reached, so this new attempt with a moment should give better results in that sense.

The overall geometry is the same as in the previous two sections, and thus it is not reported here again. The mesh along the longitudinal axis of the beam is also the same (20 B4), always according to the fact that where the hole is present, the cross-section mesh is different from the other parts. Note that here, unlike chapter 4.1, the geometry has not been elongated with the two rigid edges, because it is supposed that, due to the already thick cross-section, local forces should not imply very high local strains.

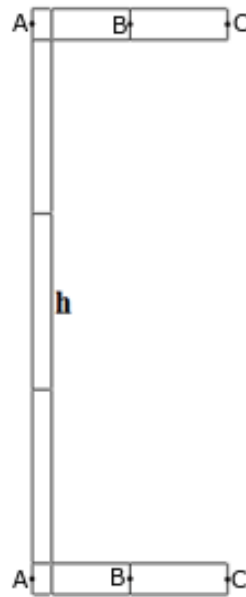


Figure 3.21: Holed C-beam with two moments applied, Cross-section mesh, 9 L9; loads are applied in points A and C, boundary conditions in points B

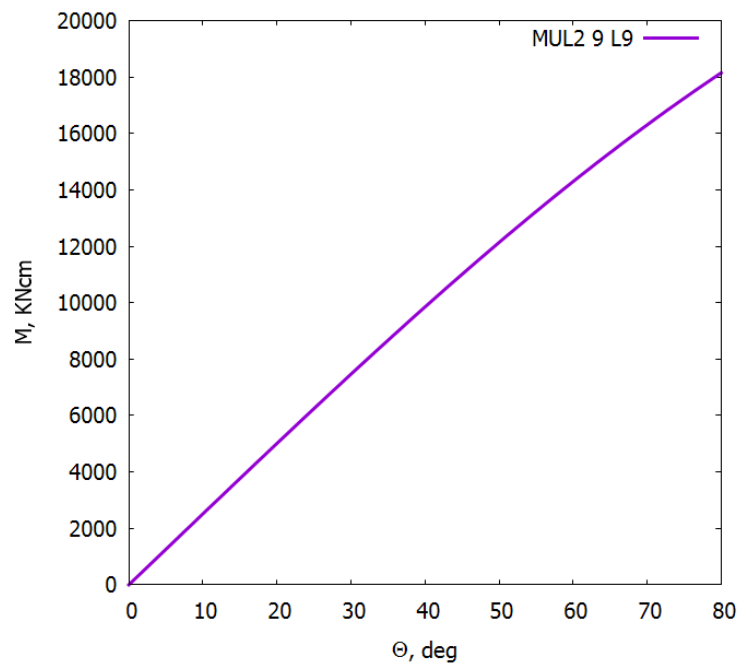


Figure 3.22: Holed C-beam equilibrium curve due to two moments applied at the extremities of the structure

The cross-section mesh is showed in Fig. 3.21, where the presence of 9 L9 elements is visible (remember that the element denoted with the letter "h" is not present in the parts where the holes are located). Some relevant points are also indicated, where the BCs and loads are applied. In particular, concerning the cross-section whit $y = 0 \text{ mm}$, in points A there are two forces (one for each point) directed towards the inside of the page, in C two forces directed to the outside of the page, and in points B the BC assuming all the displacement equal to zero (remember that in the other edge cross-section, where $y = 180 \text{ mm}$, the movements along the y-axis are permitted). The four applied forces have the same value, in order not to create undesired moments.

The equilibrium curve obtained for this analysis is shown in Fig. 3.22, even if it is not of particular relevance. It is substantially a straight line, without any non-linear behavior; in fact, the little deflection detectable for angles of rotation greater than 60° is attributable only to the way the moment is calculated:

$$M = F * t * \cos \frac{\theta}{2} \quad (3.1)$$

where F is one of the forces applied as explained before, t is the distance between the two points A (or B , equivalently), and θ is the angle in abscissa. Thus, as the angle increases, the factor $\cos \frac{\theta}{2}$ makes the moment decrease. This is the reason for the little decrement of the curve visible in Fig. 3.22 and, to avoid this problem, from now on, all the curves subjected to this formula for the moment calculation will be limited to $\theta = 60^\circ$.

Graphical results of this analysis are showed in Fig. 3.23. Although the pronounced rotation, the deformed beam follows an arc of a circle, without any particular discontinuity due to a possible collapse in the hole region. This can be because the cross-section of the beam is still very thick, not allowing the establishment of the buckling behavior; for this reason, the subsequent analysis will be carried out with a very smaller thickness of the cross-section, and a little bigger hole.

3.3.4 Bending moments with thin cross-section

This analysis is an evolution of the previous one, as it is a further attempt to establish a buckling behavior in the beam subjected to a bending moment. Thus,

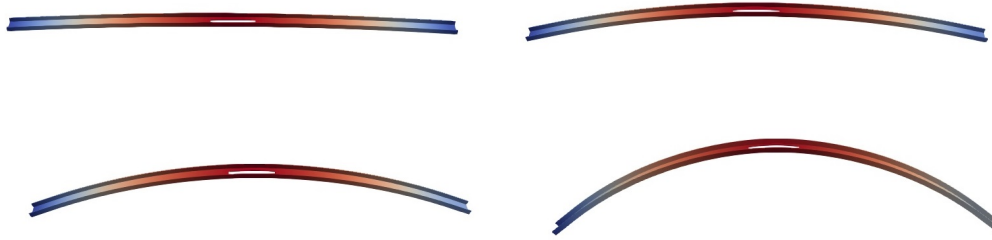


Figure 3.23: C-Beam with one hole and moments applied to the two extremities - deformed shapes

the cross-section of the C-Beam has been considerably thinned, and the dimensions of the hole have been increased.

The new geometry of the cross-section, together with its mesh, is showed in Fig. 3.24. Some of the dimensions indicated in this figure are changed from the previous analysis, and all of them are reported here for convenience:

- $h = 30 \text{ cm}$
- $w = 10 \text{ cm}$
- $t = 1.6 \text{ mm}$
- $s = 1 \text{ mm}$
- $W = 5 \text{ cm}$
- $H = 10 \text{ cm}$

The hole is located at the center of the vertical side of the "C" and, in the holed elements, its corresponding element is not present, reducing the mesh to 8 L9. The mesh along the axis of the beam is not varied from the last analysis as regards the number of elements (20 B4), but the hole has been enlarged, and now it occupies the 9TH, 10TH, 11TH and 12TH elements. The result of the disposition of the hole can be seen in Fig. 3.25.

Forces and BCs are imposed using the same nodes as in the previous analysis; thus, regarding Fig. 3.21, in points *A* and *C* two sets of two forces each are located,

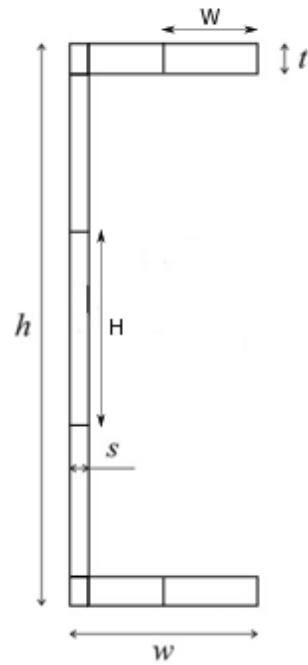


Figure 3.24: Holed C-beam with thin cross-section mesh, 9 L9



Figure 3.25: Thin C-beam, hole location

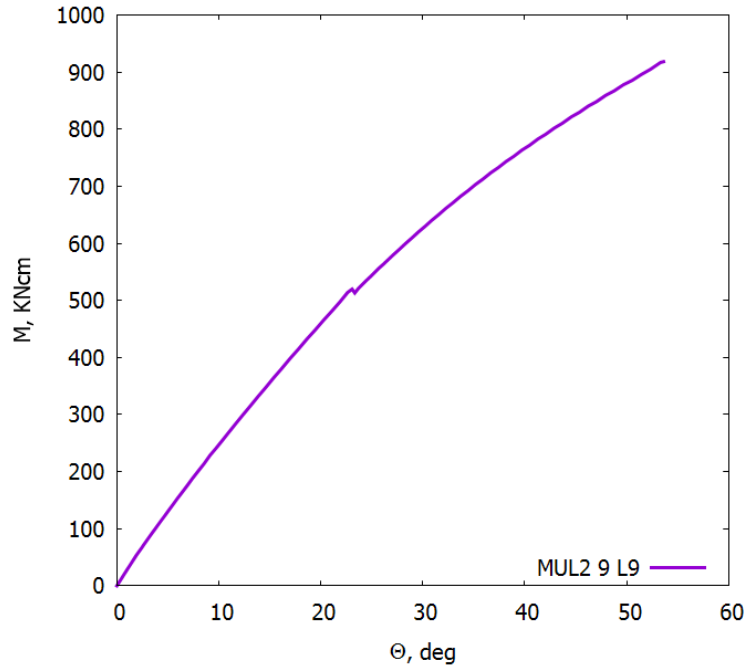


Figure 3.26: Holed C-beam equilibrium curve with the thin structure and bending moments applied

creating a bending moment around the vertical z -axis, while in points B the BCs bind the structure to move as already described in Sec. 3.3.3.

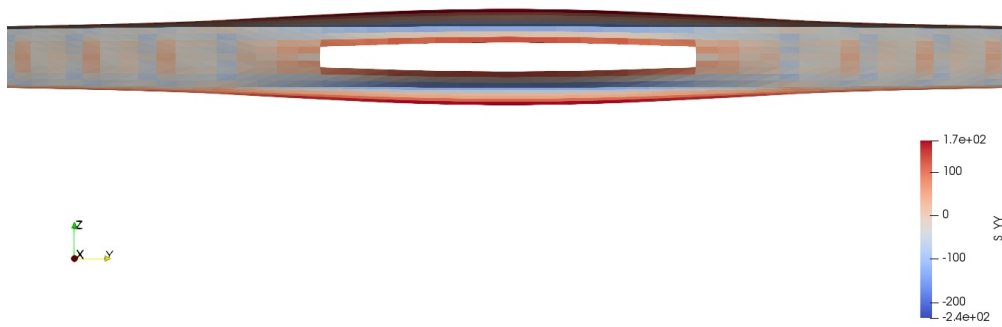
The equilibrium curve of this analysis is shown in Fig. 3.26. The straight path obtained in the analysis with the thick cross-section is a bit modified here, as the curve leaves the linear behavior already for little angles of rotation; moreover, the curve has got a discontinuity near the middle of its length, a symptom that something new is going on.

The graphical result in Fig. 3.27 confirms that the buckling is taking place. In Fig. 3.27a the global deformation of the structure can be seen, and one can notice that the shape is no more a perfect arc of a circle, but a more marked curvature appears in the hole zone, together with a constriction of the side profile. Fig. 3.27b shows in detail the hole zone, where one can see that the insoles are diverging from each other, flattening the whole section, and the hole itself is growing in dimensions. In this figure are also reported the normal stresses σ_{YY} in the zone of the hole, and can be noticed how their intensity grows a lot on the free edges of the hole and the insoles, which are probably the most problematic

regions.



(a) Global deformation



(b) Hole deformation with normal stresses

Figure 3.27: C-Beam with one hole, thin cross-section and bending moment - Deformation

In conclusion, the buckling behavior has been finally registered, and in this case, it appears under a bending moment of approximately 900 kNcm ; under that value, the structure can work quite good without losing its rigidity too much.

Chapter 4

Analysis of tape spring structures

In this chapter, thin-walled structures are finally introduced, together with their linear and non-linear analysis. The structure chosen as an example to study the bending behavior of thin deployable structures is a simple tape spring measure, as the one visible in Fig. 4.1. These are widespread deployable means for the unfolding of space instruments, as already demonstrated in chapter 1.



Figure 4.1: Tape spring measure ready to be tested, courtesy of CalTech

The study is subdivided here into three parts, the first of which deals with a beginning linear analysis, the second one with the non-linear analysis of different types of tape structures, and in the end an experimental test carried out at the CalTech is presented together with the numerical results obtained with the CUF model.

4.1 Linear analysis

The purpose of the following FEA is to evaluate the rotation of a tape spring subjected to a specific torque in the pre-buckling (i.e., linear) region, and for this reason, the post-buckling behavior is out of interest at the moment (it is discussed later in chapter 4.2). The same analysis is made both with Abaqus and with a CUF model. The two models are presented, and the comparison is made in the end.

4.1.1 Geometry

This analysis has been conducted on the tape spring structure of the same kind as the one showed in Fig. 4.1. The total length of the tape is $L = 170 \text{ mm}$, and it is made of steel with $E = 210 \text{ GPa}$ and $\nu = 0.3$. The cross-section shape is represented in Fig. 4.2, and it is composed of an arc of a circle with two straight segments at its extremities.

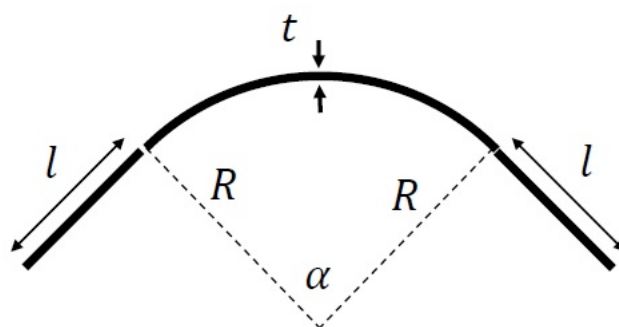


Figure 4.2: Tape spring measure cross-section geometry

The values of the geometrical parameters showed in Fig.4.2 are as follows:

- $R = 12.3 \text{ mm}$;
- $l = 6.1 \text{ mm}$;
- $t = 0.114 \text{ mm}$;
- $\alpha = 62.0^\circ$.

4.1.2 Abaqus analysis

In this section, the discussion of the results obtained by the Abaqus aided analysis is made. First, the mesh and the load application are introduced, and then the results in terms of strains.

Mesh, loads, and BCs

For the discretization of this model is adopted a 16x113 shell elements mesh, as shown in Fig.4.3.

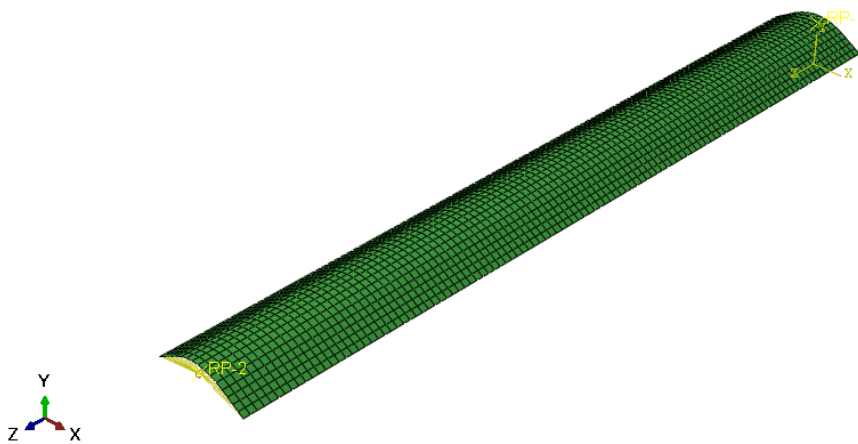


Figure 4.3: Tape spring measure Abaqus model, 16x113 shell elements. RP1 and RP2 are the rotation points

In the previous figure, two points are visible, named as RP-1 and RP-2: these are the rotation points of the edge sections, and they are used to apply loads and BCs as described afterward. Only by looking at Fig.4.3, one can say that the mesh is pretty fine, and so the results should be accurate.

As already anticipated, loads and BCs have applied thanks to the RPs. Precisely, two moments, one for each RP, are present. The intensity of each moment is settled at $M = 400 \text{ N} \cdot \text{mm}$, in order to work in the linear field. Hereafter it is defined section 1 the section corresponding to RP-1, and section 2 the one corresponding to RP-2. Section 1 is free to translate along the z-axis, while section 2 is completely fixed; both the sections can rotate around the x-axis only. The

BCs then can be written as:

$$\begin{aligned} u_x^1 &= u_y^1 = 0 \\ \phi_y^1 &= \phi_z^1 = 0 \\ u_x^2 &= u_y^2 = u_z^2 = 0 \\ \phi_y^2 &= \phi_z^2 = 0 \end{aligned}$$

The apexes denote the number of the section. Similarly, the applied torques in the current reference system are:

$$\begin{aligned} M_x^1 &= 400 \text{ n} \cdot \text{mm} \\ M_x^2 &= -400 \text{ n} \cdot \text{mm} \end{aligned}$$

Note: torques are positive if concordant with the positive x-axis following the right-hand rule.

Results

The graphical result of the static linear analysis done is represented by the deformed tape in Fig.4.16, where different colors mean different u_y displacements. It must be specified that the representation is not in scale, but amplified in order to see the displacement better.

The rotation to which each of the two edge cross-sections is subjected is equal to 1.304° . Thus, the total rotation, given as the double of the number written right now, is:

$$\theta = 2.608^\circ$$

4.1.3 MUL² analysis

In this section is described the CUF Model adopted to do the analysis and the results obtained.

Before starting to talk about the CUF Model, it is necessary to make some annotations: the purpose of this work is to do a static linear analysis of the structure preparatory for a successive non-linear analysis; Mul² code is not able to do a non-linear analysis with concentrated torques, but only with concentrated

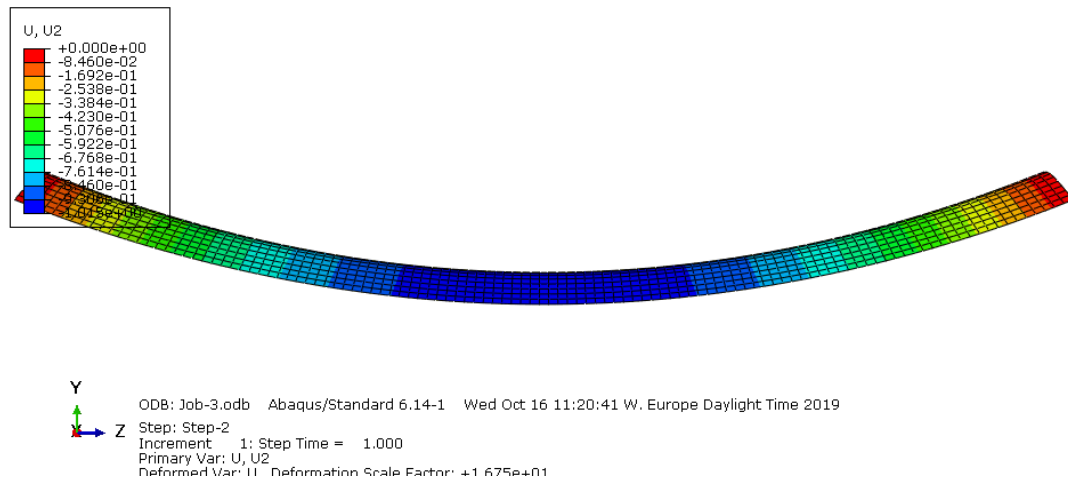


Figure 4.4: Tape spring measure Abaqus model deformation; colors scale stands for the vertical displacement

forces. For this reason, in order to prepare the input files for the successive analysis, the torques applied at the tape edges are transformed into a set of concentrated forces in some particular nodes, as it is discussed in Section 4.1.3.

Applying concentrated forces unfortunately creates a new problem: local deformations. In order to minimize these errors a 5 mm length piece of structure will be added at both edges of the tape, with a Young modulus 100 times greater than the rest of the structure. In this way, local strains at the edges of the tape are negligible, and the edge effects are reduced. This trick is repeated every time the bending of a structure involves a set of concentrated forces, like in chapter 4.2.

Finally, it is also important to emphasize that the reference system here is different from the one adopted for the Abaqus model, and from now on, the longitudinal axis will be the y-axis, while the x-axis and the z-axis will be on the cross-section; the origin is the circumference arc center.

CUF Model

Material For the reasons discussed previously, two different isotropic materials are created; their properties are listed in Tab. 4.1.

Material ID#	$E(MPa)$	ν
1	$210 \cdot 10^3$	0.3
2	$210 \cdot 10^5$	0.3

Table 4.1: Tape spring measure CUF model material properties

Given these two materials, two different laminations are created, one for each material. Please note that in this case, creating a lamination is useful just because Mul² code needs it; otherwise, as we are working with isotropic materials, a lamination is mostly superfluous.

Nodes Along the y -axis of the beam, different spacing between nodes is made for the central 170 mm and the lateral 5 mm : 10 B4 elements are created for the central part, whereas 1 B3 element is created for each of the lateral parts. There is, therefore, a total amount of 35 nodes and 12 elements.

B3 elements are adopted for the lateral parts because they are only 5 mm long, less than each element of the central part (spacing between each node is 2.5 mm in the lateral parts and 5.67 mm in the central part).

Mesh On the cross-section of the beam is created a mesh composed of 14 L9 elements, positioned as shown in Fig.4.5.

The nodes denoted with the letters A and B are of particular relevance: B-nodes have the same z -coordinate as the RP-point of the Abaqus model, whereas the A-nodes have the same z -distance from B as the C-node ($z_A = 8.38 \text{ mm}$, $z_B = 10.34 \text{ mm}$, $z_C = 12.3 \text{ mm}$). It must be specified that the nodes indicated with the letters are the ones arranged along the middle layer of the section, i.e., at an equal distance between the top and bottom surfaces. Moreover, it is also used hereafter the subscript 1 for the section at $y = 0$, and the subscript 2 for the one at $y = 180$. The reasons because of this particular mesh will be cleared in Section 4.1.3.

BCs and Loads In order to recreate as accurately as possible the boundary conditions of the Abaqus analysis, on this model are applied four node-located constraints:

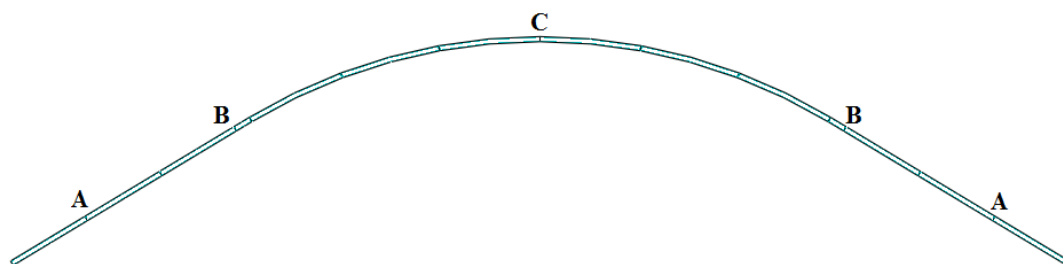


Figure 4.5: Tape spring measure CUF cross-section mesh, 14 L9; forces are applied in points C and A, BCs in points B

- 2 hinge joints in B_1 nodes;
- 2 sliding joints (y-free) in B_2 nodes.

In this way BCs are applied exactly at the same z-coordinate as the RP-points.

A torque load must be applied to both edges of the beam, but, as already discussed previously, there is the need to decompose the torques into a set of concentrated forces. The loads' composition visible in Tab. 4.2 is then created (positive sign if concordant with positive y-axis).

Intensity	Location	Quantity
$-F$	A_1	2
$2F$	C_1	1
F	A_2	2
$-2F$	C_2	1

Table 4.2: Loads applied on the tape

There is a total amount of 6 concentrated forces, disposed in order to give as resultant only the torque needed. In fact, on both edge sections, the equilibrium

equation along y-axis gives:

$$R = 2F - F - F = 0$$

To calculate the intensity of F an equilibrium equation around x-axis must be made:

$$T = 400 = 2F \cdot (z_C - z_A)$$

$$F = 51.0204 \text{ N} \cdot \text{mm}$$

Results

The graphical result of the deformed shape of the beam is shown in Fig.4.6, where a scale factor is adopted to point out the curvature better.



Figure 4.6: Tape spring measure CUF model deformed shape; colder colors indicate higher vertical displacement

The mechanical result object of this work is the rotation angle θ around the x-axis. In order to calculate it, the U_y displacements must be taken into account, especially of the particular nodes listed in Tab. 4.3.

Node ID#	x	y	z	U_y [mm]
1	0	5	12.357	0.046695
2	0	5	12.3	0.045415
3	0	5	12.243	0.044029

Table 4.3: Longitudinal displacements of some relevant nodes

By making the hypothesis of small rotations and planar deformed shape of the cross-section, the θ rotation can therefore be calculated as:

$$\theta = \frac{U_{y,1} - U_{y,3}}{z_1 - z_3} = 1.33957^\circ \quad (4.1)$$

This is the rotation around the x-axis of the beam section located at $y = 5 \text{ mm}$, so the first real section of the structure (as the first 5 mm must not be considered). Please note that Node 2 in Tab. 4.3 coincides with Node C_1 .

4.1.4 Comparison between Abaqus and MUL² solutions

Finally, a comparison between Abaqus and Mul² solutions can be made. It is still necessary to double up the angle θ obtained in Eq. (4.1), as we need the sum of both edges rotation. The overall rotation then is:

$$\theta^* = 2 \cdot \theta = 2.6798^\circ$$

The comparison between the Abaqus and the Mul² solutions is visible in the next table:

θ_{Abq}	2.608°
θ_{CUF}	2.680°

Table 4.4: Comparison between the rotations obtained with Abaqus and Mul²

The two rotations are very close to each other, and the difference is about 2%. This gap could probably be filled if the hypothesis of small rotations had not been adopted when the θ_{CUF} was calculated in Eq. (4.1). For the non-linear analysis carried out in chapter 4.2, a different way for computing the rotation is utilized since this hypothesis is no longer valid.

4.2 Non-linear analysis and sensitivity versus curvature radius

In this section, the non-linear behavior of the tape structure is described, with particular reference to the effects of the radius of curvature changing. To do that, all other parameters, that is the material and the length of the two sides of the tape (L and l), are maintained constant.

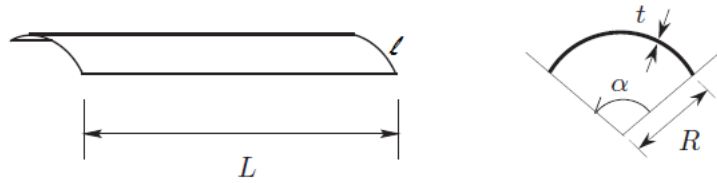
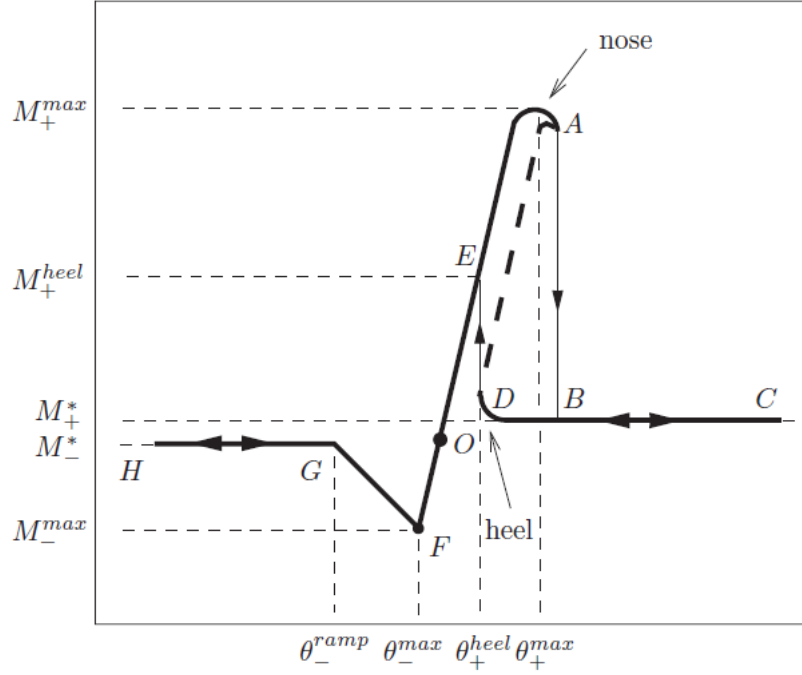


Figure 4.7: General tape geometry [28]

In literature, an in-depth study of this problem has already been done by Seffen and Pellegrino in 1997 [28]. Previously, analytical solutions to this problem was find by Rimrott (1966) [25] and Mansfield (1973) [19]. Later, numerical results was find by Fischer (1995) [12] and Seffen himself (1997) [29]. Thus, the aim of this section is not to explain how the tape structures work in the post-buckling field, but how the CUF model can predict this behavior accurately. The comparison is made with the Abaqus solution obtained for the same problem. Finally, in the last section, a complete study carried out with Abaqus is given.

Usually, the equilibrium curve of a tape structure subjected to a bending moment is of the kind showed in Fig. 4.8. Here are visible some characteristic quantities, such as the opposite sense critical moment M_+^{max} , the equal sense critical moment M_-^{max} , and the post-buckling moment M_+^* . The slope of the curve in the linear region represents the initial stiffness of the structure. Hence, the curve follows at the beginning a straight path, identified with the pre-buckling (nearly-linear) region; there is successively an unstable region, from A to D, where the moment and the rotation decrease both; at last, the post-buckling region is represented by a horizontal line.

Semi-analytical expressions for all the parameters visible in Fig. 4.8 are pre-

Figure 4.8: Tape typical M- θ diagram [28]

sented in [28]. For example, the expression for M_+^* is:

$$M_+^* = (1 + \nu)D\alpha \quad (4.2)$$

where ν is the Poisson's ratio, α is the angle subtended by the circular arc of the cross-section, and D is a function of the material and the thickness of the tape, i.e.:

$$D = \frac{Et^3}{12(1 - \nu^2)}$$

For all the following analysis $E = 210 \text{ GPa}$, $t = 0.114 \text{ mm}$, and $\nu = 0.3$, hence $D = 28.491 \text{ Nmm}$.

4.2.1 CUF validation

The purpose of this section is to compare a specific CUF model with the same Abaqus model, in order to demonstrate the correct behavior of the first one. To do this, the radius of curvature chosen is equal to 100 mm , and the opposite sense

bending is taken into account. The length l of the middle layer of the cross-section is constant for all the analyses and equal to 25.5 mm . The angle α can be easily computed with the relation $\alpha = \frac{l}{R}$; for $l = 100 \text{ mm}$, its value is $\alpha = 14.6^\circ$. The thickness t is maintained constant and equal to 0.114 mm , and the length of the tape is $L = 170 \text{ mm}$.

The following subsections present the models created for the Abaqus and Mul² analysis. These models are, apart for some little changes in the cross-section geometry, the same for all the analyses reported hereafter.

Abaqus model

The Abaqus model is showed in Fig. 4.9. The mesh is composed of 1020 shell elements, of which 12 along the short edge, and 85 along the long edge. Two moments are applied, on the two edges of the tape, through a set of coupling constraints that connect the cross-section kinematics to the movements of its center of mass. The position of the center of mass is given by the formula $Y_G = \frac{R \sin \alpha}{\alpha}$, where the origin $Y = 0$ is fixed at the center of the arc of a circle representing the cross-section.

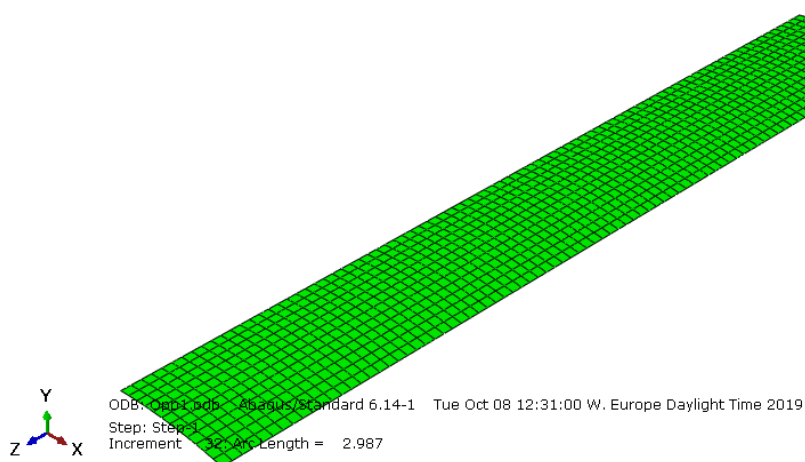


Figure 4.9: Abaqus model tape R100, 12x85 shell elements

CUF model

The CUF model is composed of 22 B4 elements along the longitudinal y -axis of the beam and 10 L9 elements on the cross-section. The cross-section mesh is visible in Fig. 4.10.

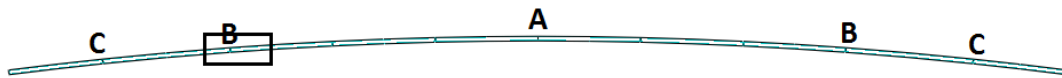


Figure 4.10: CUF model tape R100, 10 L9

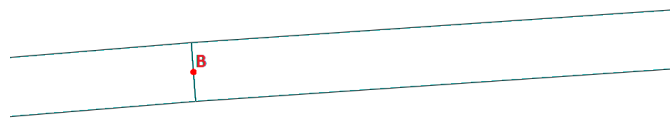


Figure 4.11: Detail of Fig. 4.10

For the reasons already discussed in a previous chapter, when the linear analysis of the tape spring was carried out, Mul^2 code can not deal with moments, but only with concentrated forces. Thus, an analogous mesh is here done, in which a series of points are identified. By looking at Fig. 4.11 it is visible that these points lie on the middle layer of the shell. A force equal to F is applied in point A , and forces equal to $\frac{F}{2}$ are applied in the points C creating, depending on their verse, a moment that will bend the tape in the opposite or equal sense. In points B ,

the constraints are present; remembering the notation of that previous chapter, in points B_1 only the rotation around x-axis is permitted, while in points B_2 also the translation along the y-axis.

The total length of the beam here is 180 mm, in order to eliminate the local effects of the concentrated forces (in fact, the first and last 5 mm are composed by a material with a Young modulus 100 times greater than the rest of the beam).

Numerical results

The comparison between the two models is shown in the graph of Fig. 4.12.

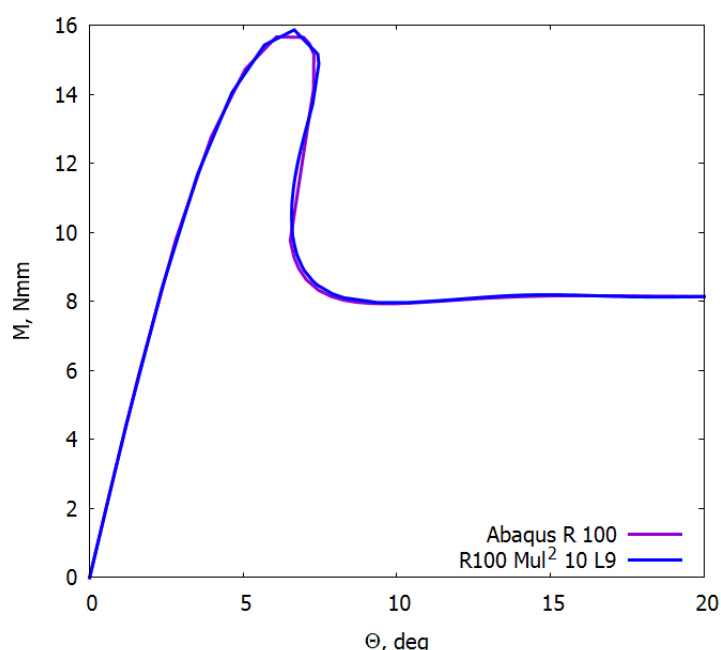


Figure 4.12: Equilibrium curve, tape R100, Abaqus shell and CUF models

The Mul^2 solution predicts very well the Abaqus one, especially in the pre-buckling and post-buckling region. On the other hand, in the unstable region are present some minimal differences, perhaps due to the different steps adopted by Abaqus and Mul^2 in that region. Nevertheless, the overall result is quite excellent, and it is then proved that the CUF model can predict very well this kind of problem.

With the help of Eq. (4.2), the analytical M_{\dagger}^* should be equal to $M_{\dagger}^* =$

9.44 Nmm . The value predicted by both the Abaqus and Mul² analysis is slightly lower (a little more than 8 mm), but the difference is still acceptable.

4.2.2 CUF analysis

Once the Mul² code is validated, a series of analyses can be made with it in order to establish how the equilibrium curve of the tape modifies itself when the radius of curvature changes. The results of these analyses are shown in the graph of Fig. 4.13.

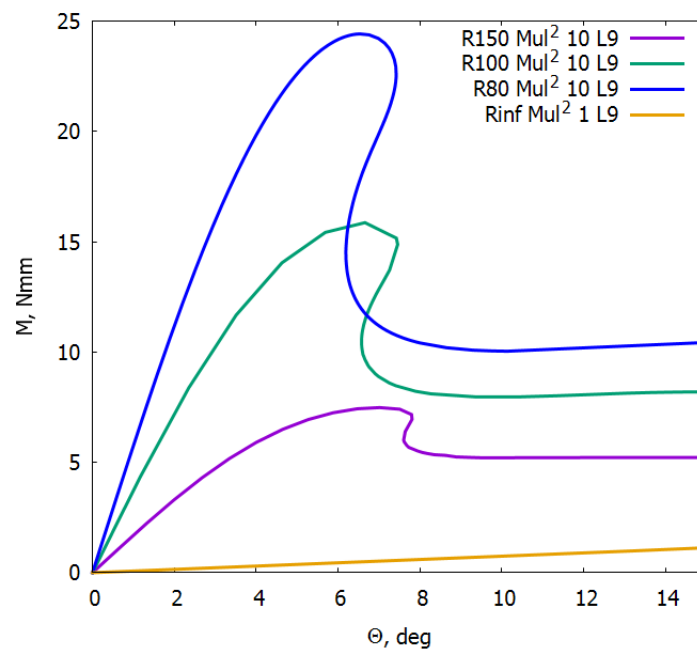


Figure 4.13: Effect of radius of curvature on the tape equilibrium curve, various CUF models

The R100 model is the same as described in Sec. 4.2.1, while the mesh on the cross-section of the other models is shown in Fig. 4.14.

The mesh in Fig. 4.14c represents a flat tape. In that case, only two forces, of equal intensity, are applied in each of the end cross-section, in points A and C ; these points are respectively positioned on the top surface and the bottom surface. On the other hand, the two constraints are maintained the same as the other models, but points B are moved to the side edges of the cross-section (still on the



(a) R80, 10 L9



(b) R150, 10 L9



(c) $R\infty$, 1 L9

Figure 4.14: Tape CUF meshes, different curvature radius and number of elements

middle layer).

The behavior of the flat tape equilibrium curve is quite peculiar: it is practically a straight line as if the deformation takes place in a linear context; a direct consequence is that the critical load is absent, as well as the unstable region.

With a decreasing radius of curvature, the initial stiffness of the tape increases rapidly, as well as the critical load and the post-buckling load. Moreover, also the unstable region becomes more and more evident. In Tab. 4.5 are listed some of these particular numbers.

R [mm]	K_0 [$\frac{Nmm}{deg}$]	M_+^{max} [Nmm]	θ_+^{max} [deg]	M_+^* [Nmm]	$\frac{M_+^{max}-M_+^*}{M_+^{max}}$
80	5.817	24.42	6.529	10.04	58.89%
100	3.733	15.87	6.662	7.963	49.81%
150	1.700	7.485	7.012	5.209	30.40%
∞	0.07471	NA	NA	NA	NA

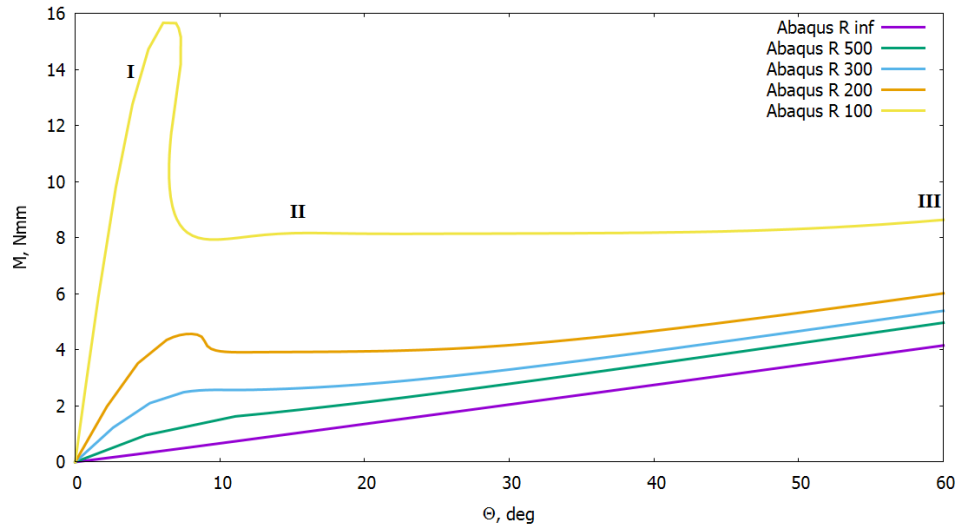
Table 4.5: $M - \theta$ curve parameters variation due to curvature radius changing

From these analyses, it is clear that by imposing curvature on the tape, its stiffness grows considerably, together with its critical buckling load. However, and this is usually not convenient, the buckling "leap" increases too, bringing to a more severe buckling snap.

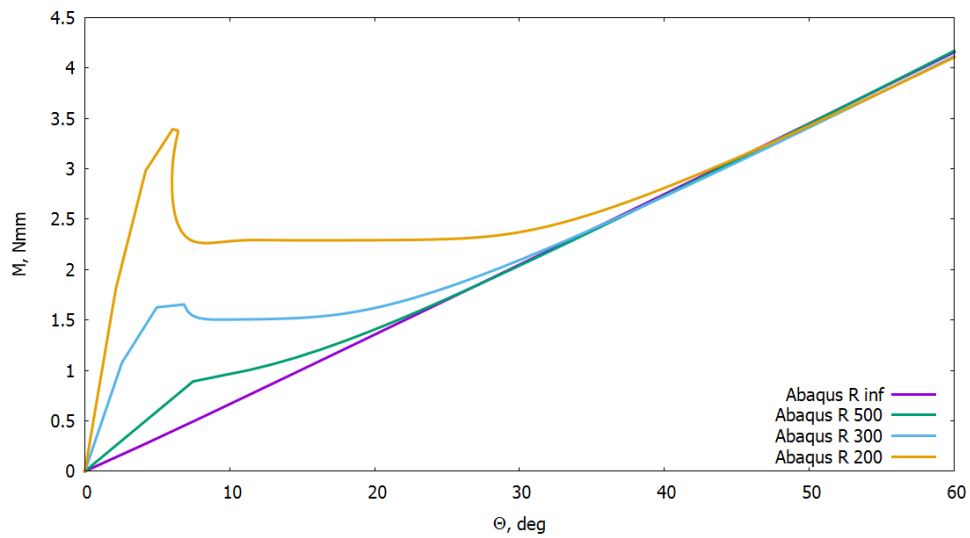
4.2.3 Abaqus analysis

In this section, a complete analysis carried out with Abaqus is presented for both the opposite and equal sense bending. Graphical results are visible in Fig. 4.15.

Fig. 4.15a shows the behavior of the tape subjected to an opposite sense bending (the R100 curve is the same as in Fig. 4.12). It is confirmed the fact that the higher is the radius of curvature, the greater are the buckling load, the stiffness, and the snap jump; in fact, for radius bigger than 300 mm, the buckling is not even present. Another fascinating behavior takes place for high bending angles: all the equilibrium curves, either directly or after the typical "plateau", tend to take the same slope as the flat tape curve, but still maintaining a certain

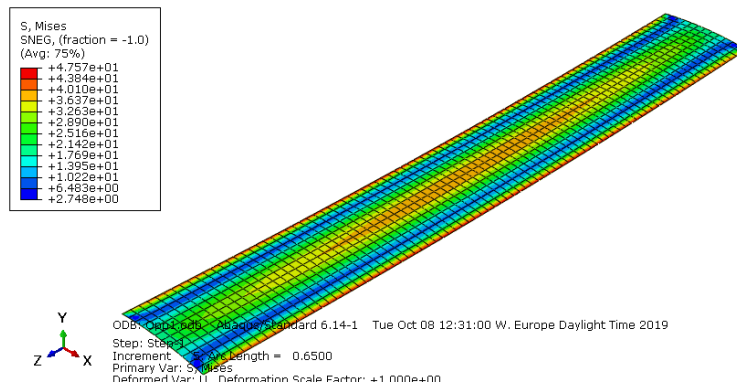


(a) Opposite sense

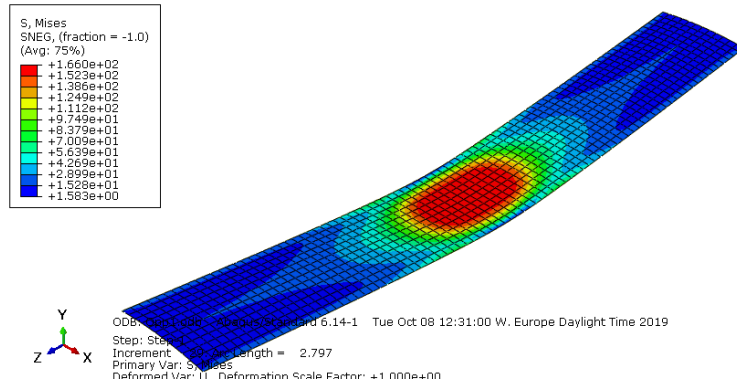


(b) Equal sense

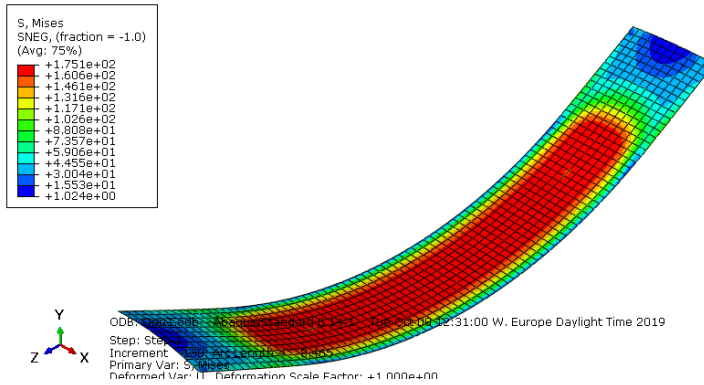
Figure 4.15: Effect of the radius of curvature on the tape equilibrium curve, Abaqus shell models



(a) Point I, pre-buckling



(b) Point II, post-buckling



(c) Point III, far post-buckling

Figure 4.16: Tape R100, Abaqus shell models deformation in the points indicated in Fig. 4.15a

distance from one another. This behavior was not highlighted before with the CUF models, because the analyses have been stopped before reaching it.

Fig. 4.15b shows the equal sense case instead. All the considerations made for the opposite sense bending are still valid, except one: the curves continue to take on the same slope as the flat tape curve, but now there is no more the distance from one another found for the opposite case.

In general, the initial stiffness is nearly the same both for the opposite and the equal sense bending, but the buckling load is slightly higher in the first case. The last comment should be made about the quasi-linear far post-buckling behavior: this could be because the tape, originally curved, begins to flatten out during the bending, assuming a behavior more and more similar to the flat tape; this behavior can be easily seen in Fig. 4.16.

The deformed shapes show that the maximum Von Mises stresses are initially concentrated on the lateral edges and in a narrow area in the center of the tape. Once the buckling takes place, the central part of the tape is flattened, and the stresses are increased a lot. Continuing to bend the tape, the flat zone widens to include nearly all the tape.

4.3 Comparison with experimental analysis

The tape spring measure already introduced in the linear analysis of Sec. 4.1 is now retrieved in order to explain the experimental analysis carried out on it, and the numerical results obtained.

4.3.1 Experiment

The purpose of this section is to explain how the experimental tests have been achieved. Thus, the experimental method adopted by the Caltech (Pasadena, California) is introduced.

The structure used for the tests is, as already anticipated, a typical commercial tape spring made of steel and a thin layer of coating all around. The coating is neglected since it was proved that it does not affect the mechanical properties of the structure; thus, only the steel is considered. Wanting to define as accurately as possible the geometry of the selected tape, a FaroArm scanner has been used. This



Figure 4.17: Commercial tape spring

is because even tiny imperfections in the material surface can lead to anomalies in the mechanical behavior of the structure. Thus, after cutting a piece of tape 170 *mm* long, the cross-section geometry stemmed from the scanner analysis is the one already used for the analysis of Sec. 4.1.



Figure 4.18: FaroArm scanner

On the other hand, measurements of the tape thickness were made by a needle caliber, doing a series of measures, and taking the average value as a result. All these measurements were made after the removal of the coating surface employing sandpaper. The average thickness found out is 0.114 ± 0.007 *mm*.

The sample is then prepared for the testing machine with the adding of two circular acrylic plates, as shown in Fig. 4.19. These plates are then clasped to the

Fischer's machine [12] used for the test, visible in Fig. 4.20.



Figure 4.19: Tape spring sample, courtesy of Caltech

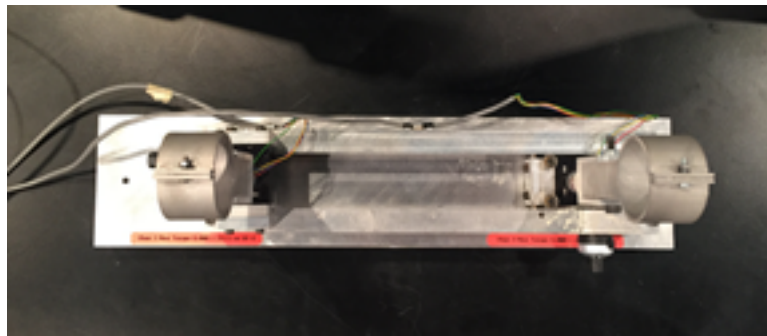


Figure 4.20: Fischer's machine, courtesy of Caltech

The moment is then applied thanks to two control dials. Moreover, one of the machine sides is fixed, while the other end is allowed to translate along the axis. The machine can determine by itself the moment and the rotation measured in each control dial. The test procedure then takes place as follows: the dials rotate with a rotation-control method, and the relative moment is read on the amplifiers of the machine; sometimes, when desired, the machine is stopped, and the two dials rotation is slightly modified in order to have the moments on the two amplifiers as equal as possible; at this point, the moment is read together with the sum of the two rotations, and these data are reported on the $M - \theta$ diagram. This procedure is repeated many times until both sides of the machine are in contact. At last, the rotation obtained is slightly modified, since the adapters of the machine are subjected to elastic deformation during the rotation; this means that the overall rotation is the sum of the base rotation and the elastic one, $\theta = \theta_{el} + \theta_{base}$.

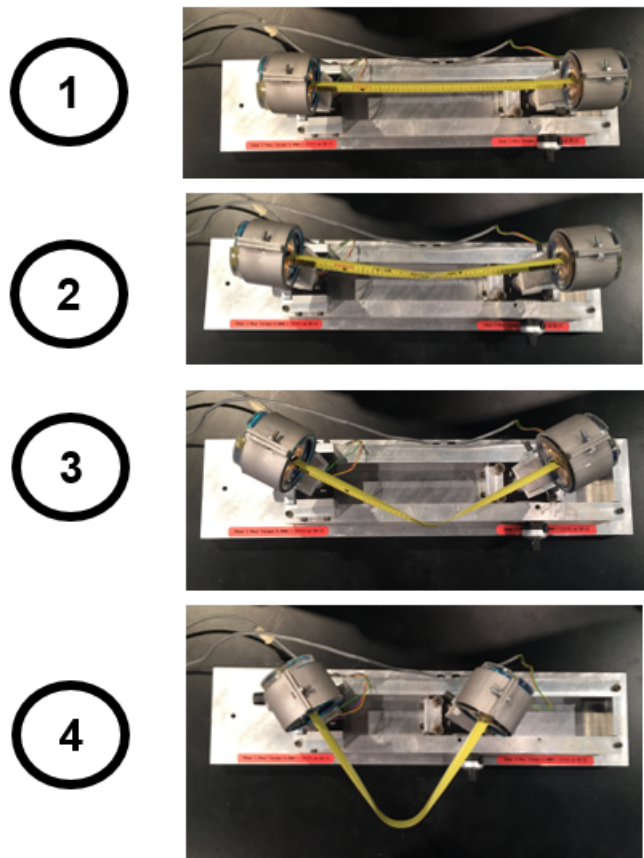
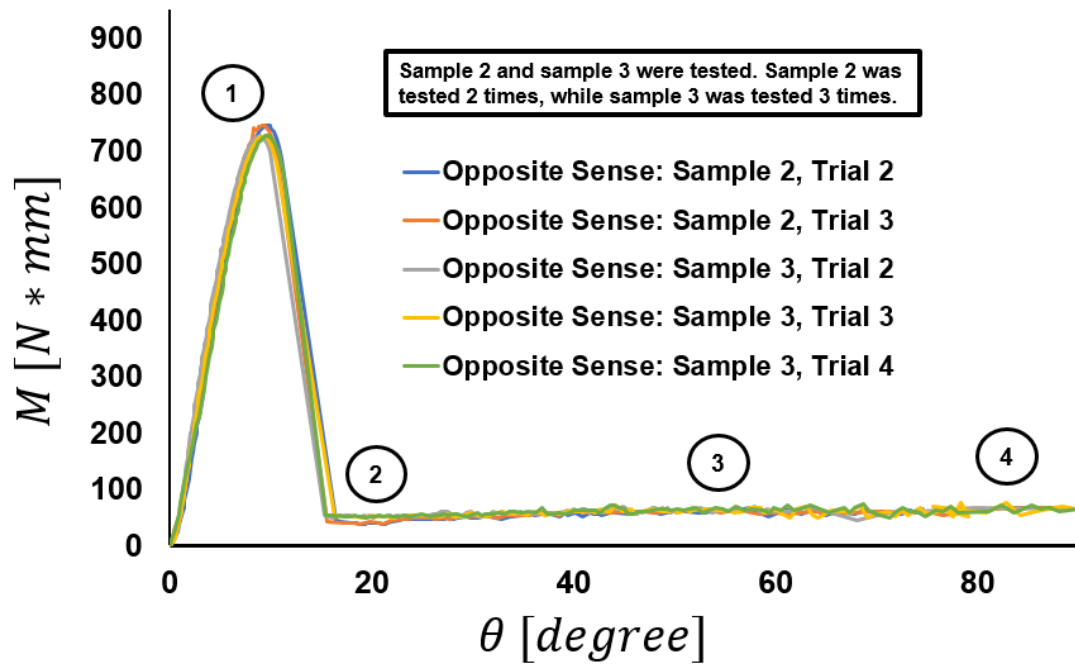


Figure 4.21: Experimental results, opposite sense bending, courtesy of Caltech

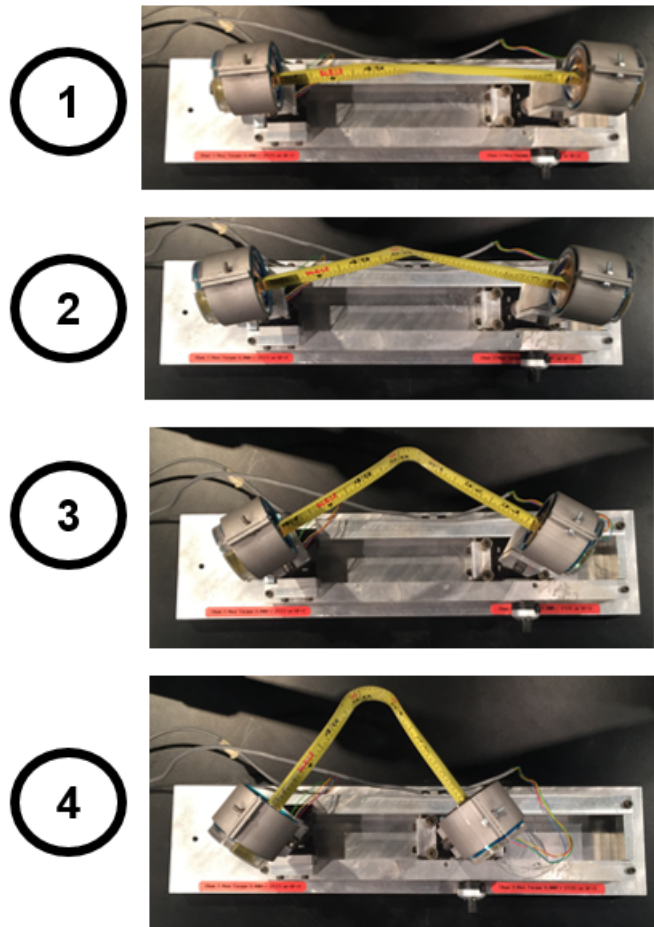
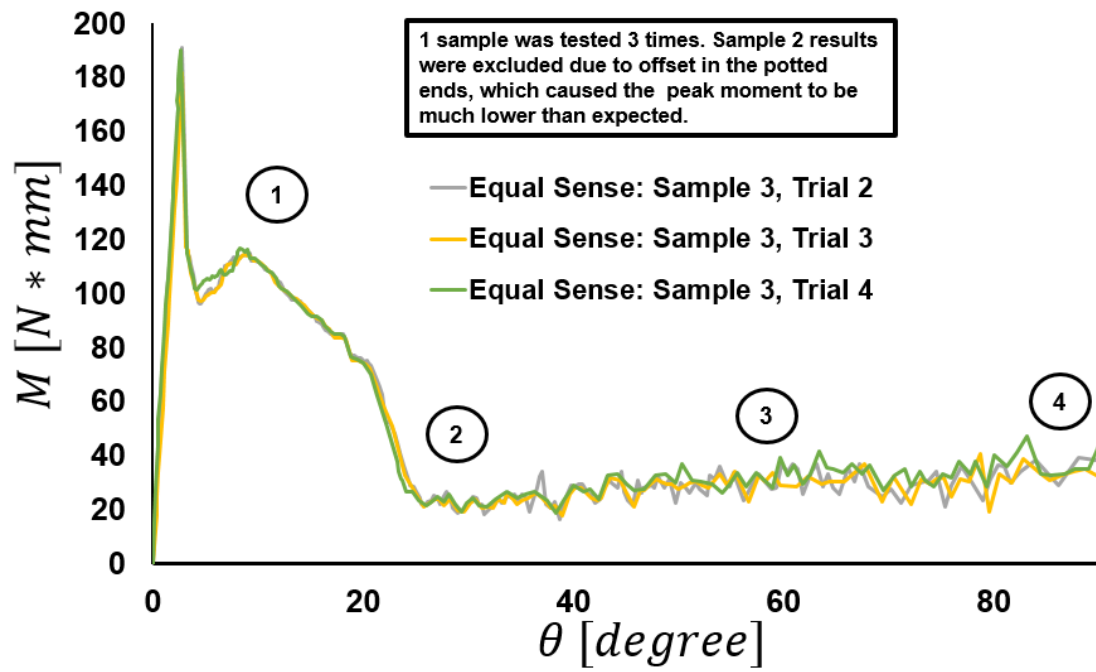


Figure 4.22: Experimental results, equal sense bending, courtesy of Caltech

Finally, the two graphs showing the opposite and equal sense bending are obtained and visible in figures 4.21 and 4.22. Five different measurements have been made for both the bending senses, using different samples, and doing several trials. The figures showing the deformed shapes of the tape highlight how the instabilities take place in many ways: apart from the classical bending buckling, a torsional buckling is also encountered in some configuration, and even the bending is not always at the tape center, but unbalanced toward one or the other end. This unusual behaviour, probably derived from some material irregularities, can not be predicted by mathematical models, which are realized as perfect structures; thus, some of the differences in the equilibrium curve between experimental and mathematical analysis can be due to this fact. A further problem can be identified in the correct estimation of the material mechanical properties, that have been assumed to be the ones owned by classical steel, but in the real sample can be slightly different.

4.3.2 Numerical results

Here a final deep study of the non-linear behavior of the tape spring structure is carried out, ending with the achievement of the complete equilibrium curve. The same problem is addressed with both Abaqus and CUF models to compare the results; moreover, in the final graph also the comparison with the experimental solution just described is reported.

Models

Both the Abaqus and the CUF models used in the current analysis are the same as the ones adopted previously for the linear analysis (apart from a very little difference in the longitudinal mesh of the CUF model) of Sec. 4.1, and, hence, an in-depth presentation of them is not written here again. However, for the sake of completeness, some important information is still provided here to help the reader's work.

Abaqus model is composed of 16x113 shell elements, as shown in Fig. 4.3. CUF model, on the other hand, is composed of only 14 L9 elements on the cross-section, and 12 B4 elements along the axis. Thus, again, the mesh of the Abaqus model is pretty finer than the CUF one but, as can be seen soon, results are good for both

the cases.

Equilibrium curve

The complete equilibrium curve can be seen by looking at the graph in Fig. 4.23, where both the equal sense and the opposite sense bending are shown together with some experimental results.

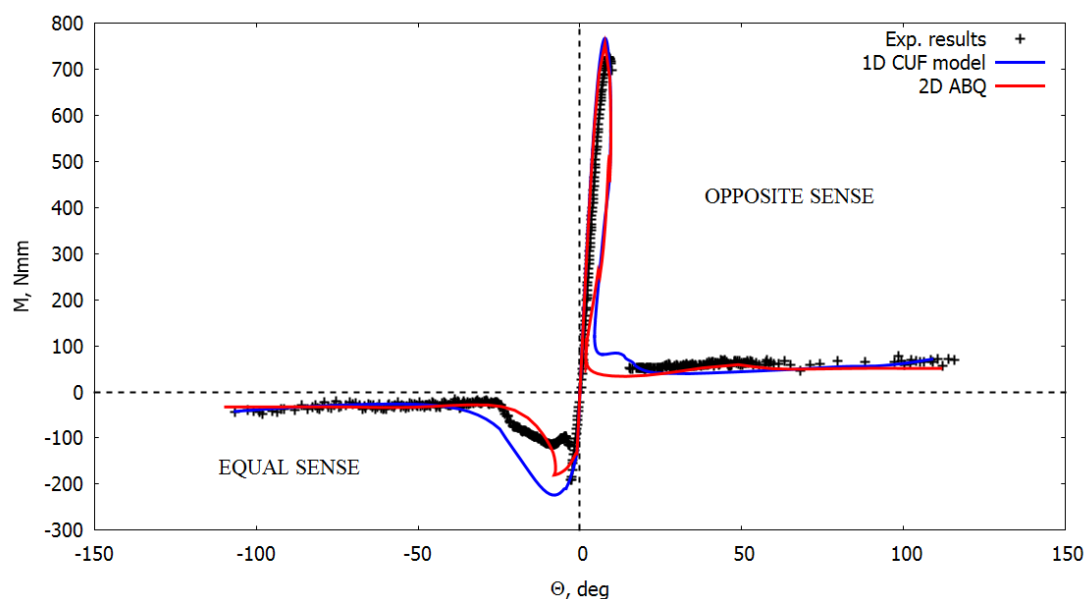


Figure 4.23: Tape spring measure complete equilibrium curve

As it is written in the graph, the opposite sense region is the first quadrant, whereas the equal sense is in the third one. The black dots represents the experimental test results, as it is described in the previous section. The curve is thoroughly developed, as the post-buckling constant-moment region has already been reached for all three curves.

As can be seen even at first sight, both the Abaqus and the CUF solutions match well enough the experimental solutions. In fact, both the Abaqus 2D model and the CUF 1D model can predict very well the critical load, especially in the opposite sense bending; the equal sense bending critical load is slightly overestimated, but the difference remains very little. Moreover, the curve shape obtained with the CUF model matches very well the theory exposed by Seffen and Pellegrino

([28]). The most critical region is undoubtedly that of the equal sense bending, where there is the transition region between the pre-buckling and post-buckling.

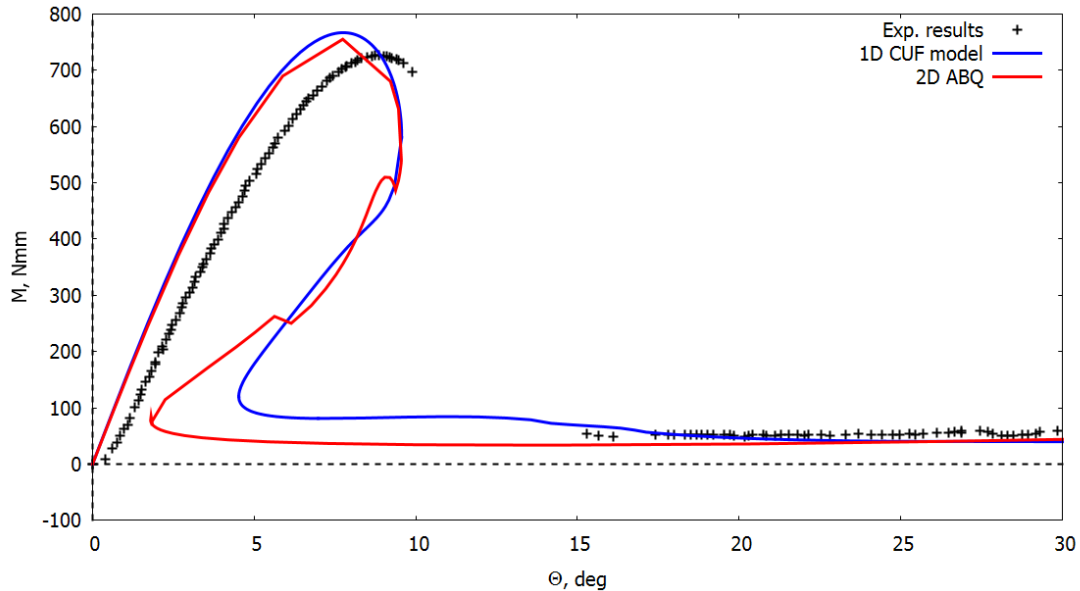


Figure 4.24: Tape spring measure equilibrium curve - opposite sense detail

Fig. 4.24 shows, as it is written in its caption, the detail of the right side of the complete equilibrium curve, representing the opposite sense bending. This figure highlights a small difference between the numerical solutions and the experimental tests also in the pre-buckling region: this can be due to several factors, like the presence of small imperfections in the samples (not provided in the numerical models), or the wrong assumption of its Young modulus. In fact, as already told in the previous section, the physical samples together with the bending behavior show also a torsional movement, not predicted with the numerical models, whose deformed shapes are shown in Fig. 4.25 using Abaqus. The peculiar behavior registered in the first of the three pictures, where the tape is flexed to form three humps, is completely absent in the experimental test; the three humps then merge into a single hump, which remains the same for all the deformation process, becoming home to the greatest stress values.

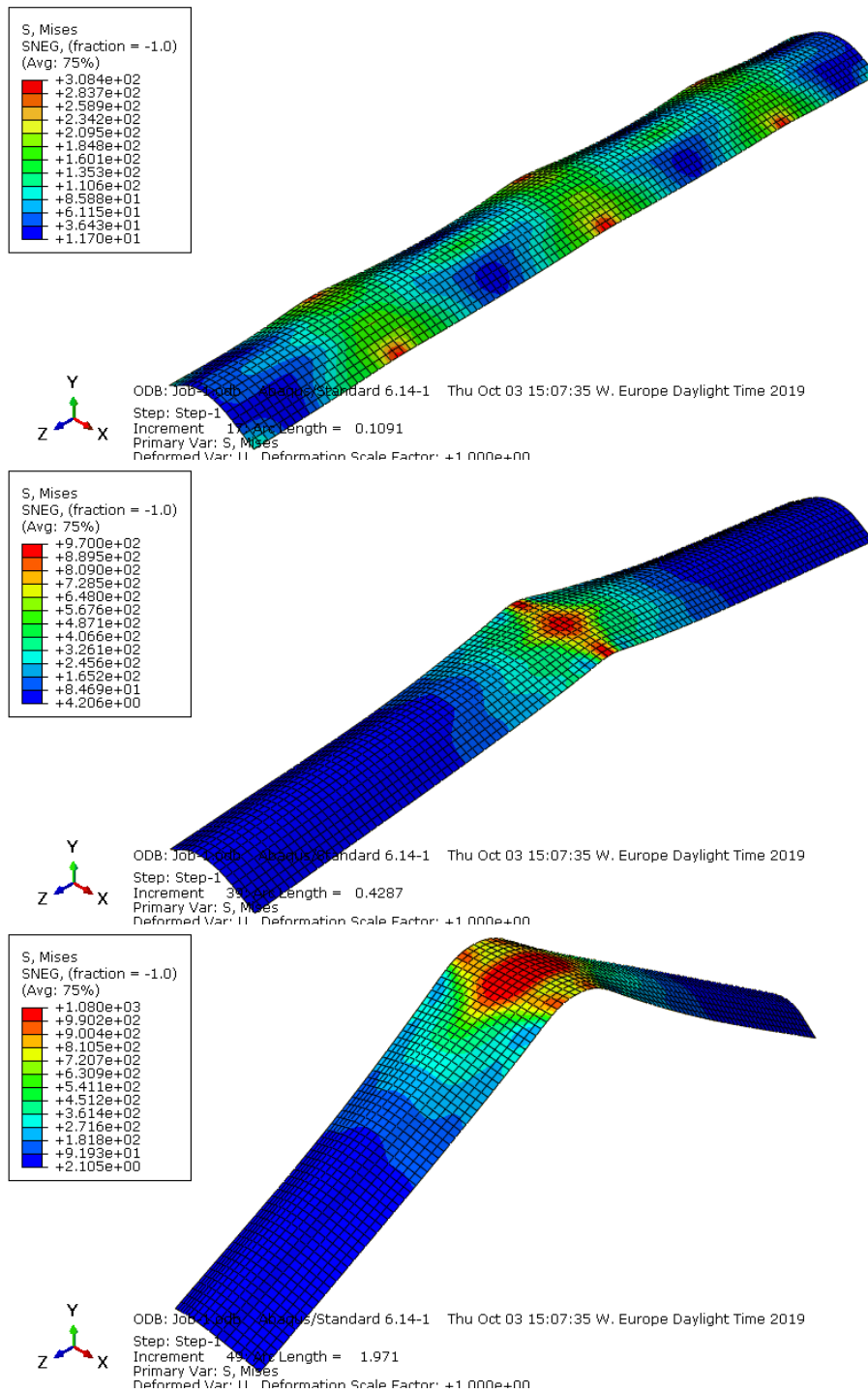


Figure 4.25: Tape spring measure deformed shapes with Abaqus, 16x113 shell elements

Chapter 5

Analysis of TRAC boom structures

This chapter wants to introduce and study the main applications of the TRAC booms and to evaluate their equilibrium curves. The chapter begins describing possible applications of these structures and goes on with a series of analyses, including a parametric analysis where the boom length is changed in order to study its effects on equilibrium curves.

5.1 Introduction

The Triangular Rollable And Collapsible boom (TRAC) is another kind of structure widely used in spacecraft applications, due to its lightweight and coiling properties. The name itself gives suggests how its shape must look, and its shape is shown in both the closed and open configuration in Fig. 5.1. This truss is usually coiled around a central hub, as showed in Fig. 5.2.

One of the most diffused application is the supporting structure for large planar deployable membranes, carrying solar cells, antennas, or used as solar sails. Fig. 5.3 shows, for example, the configuration of a solar sail, where the TRAC booms are colored green, and represents the diagonals of the square sail; such booms when folded are coiled around a hub staying in the center of the sail, which rotating produce the folding process resulting in the stowed configuration visible in Fig. 5.4.

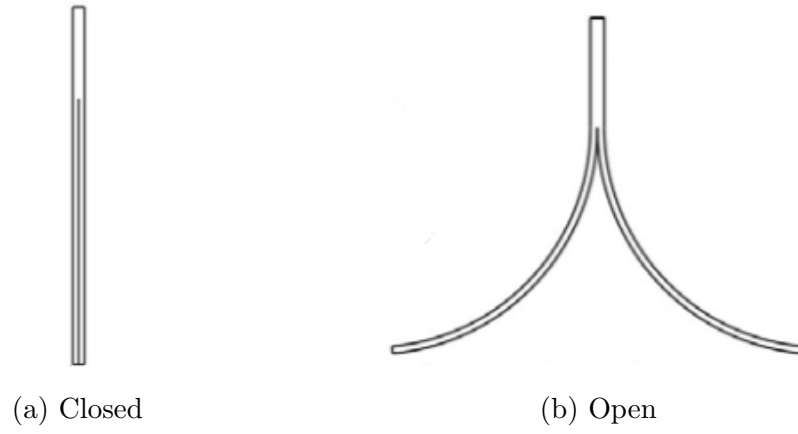


Figure 5.1: TRAC geometry in the open and closed configuration (modified from [2])

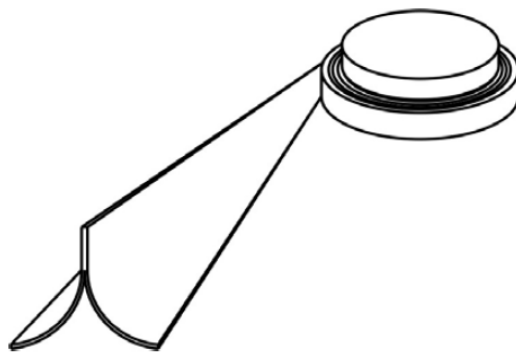


Figure 5.2: TRAC boom with central hub mechanism [2]

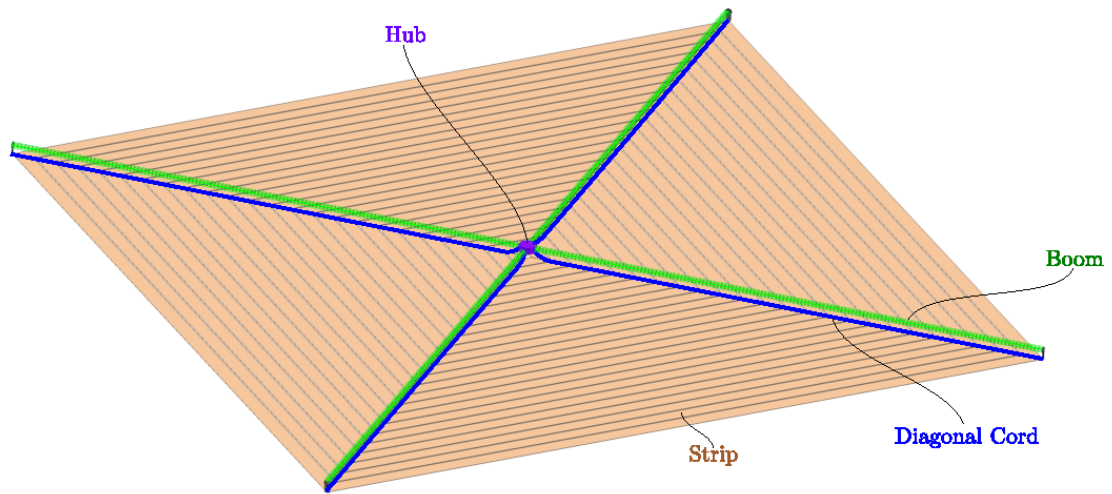


Figure 5.3: Typical TRAC application in membranes supporting [1]

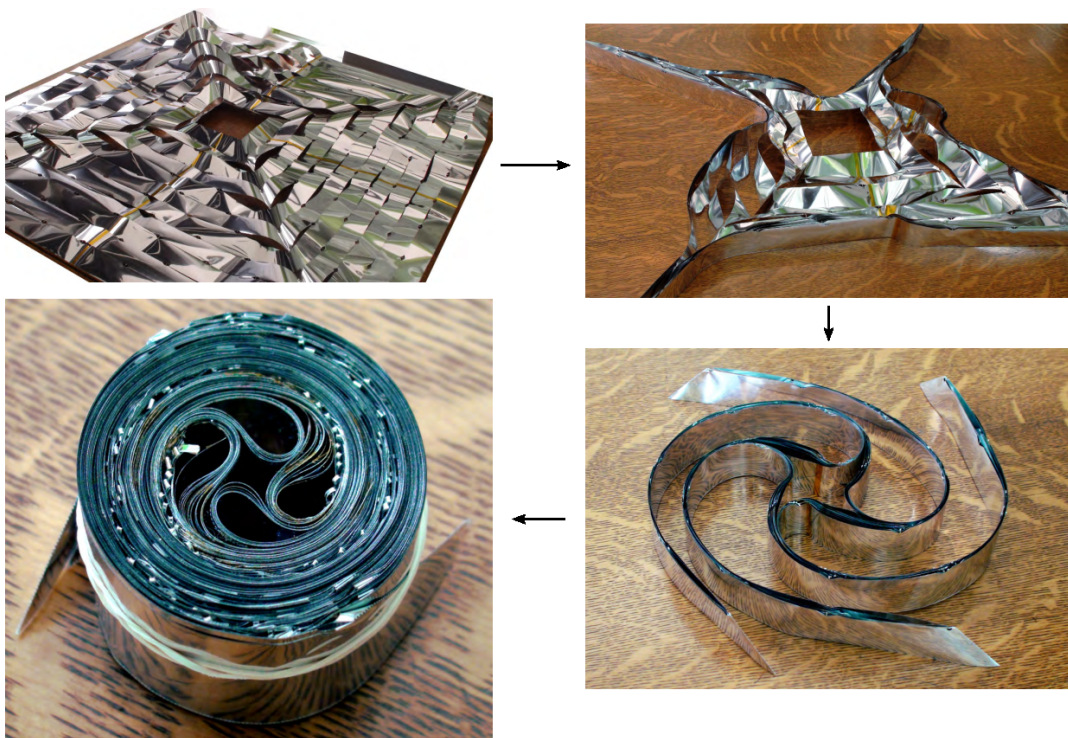


Figure 5.4: Membrane folding process thanks to TRAC booms [1]

It has also been established by Roybal [27] that TRAC structures work better than comparable CTM and STEM ones, and hence this is the reason for further studies about these particular booms. More information in the literature about the argument can also be taken from the works of Leclerc and Pellegrino ([15], [16]).

Geometry All the analyses described in this chapter will refer to the general cross-section geometry represented in Fig. 5.5, whose parameters are equal to:

- $w = 8 \text{ mm}$;
- $t = 0.08 \text{ mm}$;
- $r = 12.7 \text{ mm}$;
- $\theta = 90^\circ$.

It is composed by a vertical web and two flanges, all of them with a very little thickness; these three components together make the triangle that gives the name to the structure. The length of the beam is a parameter that will be changed in the various analysis, from 500 mm to 1500 mm , in order to study how this quantity affects the structure behavior.

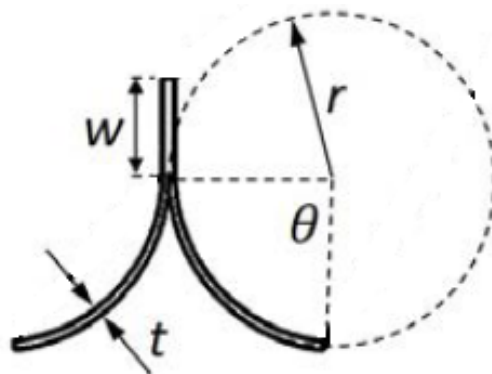


Figure 5.5: TRAC cross-section geometry with main parameters denomination (modified from [16]). $w = 8 \text{ mm}$, $t = 0.08 \text{ mm}$, $r = 12.7 \text{ mm}$, $\theta = 90^\circ$

5.2 Linear analysis

This section contains the results of some preliminary linear analysis carried out on the TRAC structure, subjected to three different load conditions. Every analysis is described separately in a dedicated subsection. Each subsection begins with the description of the various meshes adopted in the following analysis, both the linear and non-linear ones. Nevertheless, every time a new analysis is described in the following sections, the corresponding mesh is called back.

The overall geometry of the boom, apart from the cross-section already given in Fig. 5.5, is showed in Fig. 5.6, where the orientation of the axis is also visible. This particular boom is 500 *mm* long, but the length is the only property that will be changed further on.



Figure 5.6: TRAC boom geometry with orthogonal axis orientation

Moreover, despite the different lengths of the booms, the longitudinal mesh is also the same, and it is composed of 21 B4 elements. The first element is made by a more rigid material than the other 20 elements, in order to delete possible effects of the concentrated forces; moreover, the 20 "normal" elements compose the total length of the boom, while the first rigid element is added to the first part of it. The material chosen for all the analyses is steel, with $E = 210 \text{ GPa}$ ($E = 21000 \text{ GPa}$ for the rigid element). That said, in all the linear analyses only the 500 *mm* configuration boom has been considered, and thus the total length of the boom composed of 21 elements amounts to 525 *mm* (this means that the rigid element is 25 *mm* long).

Hereafter, with the terms X-bending and Z-bending will be called the bending

respectively around the X-axis and Z-axis.

5.2.1 Z-bending

The cross-section mesh used for the Z-bending load configuration is shown in Fig. 5.7, where every purple triangle represents the end of one element. For the sake of clearness, the detail of the vertical straight flange is also visible in Fig.5.8. As can be seen, the vertical flange has got two series of elements along its thickness, while the two curved flanges have only one series. In conclusion, the cross-section mesh is composed of 32 L9 elements, ten on each of the curved flanges, and 12 in the vertical one, for a total amount of 185 nodes.

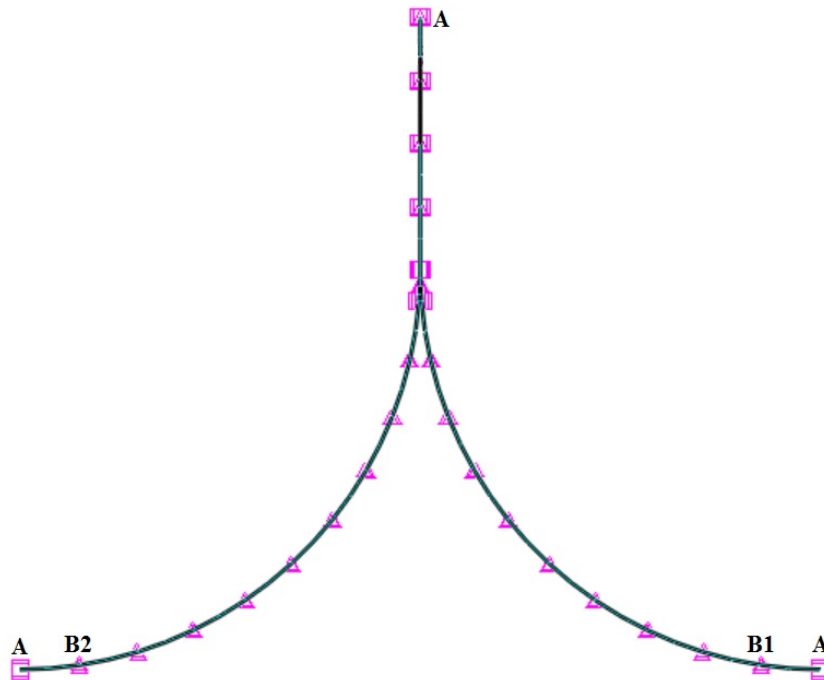


Figure 5.7: TRAC boom cross-section mesh for the Z-Bending configuration. Each of the triangle represents the edge of an element. Letters indicate the nodes upon which BCs and loads are applied, BCs in A, loads in B. 32 L9

Loads and BCs are applied to the nodes marked with letters of Fig. 5.7. Here letters *A* indicate the nodes upon which the BCs are present, while letters *B* where the loads are. Naturally each load and BC is applied on the central node of the trio each letter can identify. In points *A*, only the translation along the Y-axis is



Figure 5.8: Detail of the vertical flange of the cross-section of Fig. 5.7, together with the conjunction zone. 12 L9 elements on this flange

permitted, while the others are locked; in this way, torsional rotation of the cross-section is not permitted. The total moment desired for this linear analysis is equal to $M = 1000 \text{ Nmm}$, and in order to obtain this load, as the distance between the two points B is equal to $d = 21.6262 \text{ mm}$, in each of the points is applied a force equal to $F = 46.24 \text{ N}$. The sign of each force depends on the rotation one wants to obtain: for a positive rotation around the Z -axis, B_1 has a positive force, while B_2 a negative one. On the other edge of the boom, the cross-section is clamped in all its nodes. In Tab. 5.1 and Tab. 5.2 all the loads and the BCs on the frontal cross-section are summarised for more clarity.

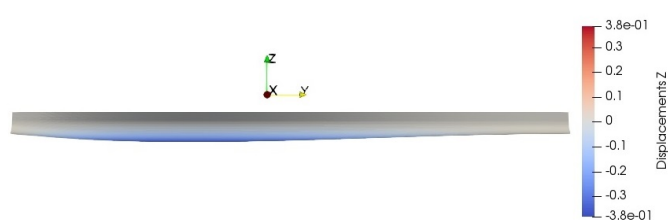
Location	F_X	F_Y	F_Z
B_1	0	46.24	0
B_2	0	-46.24	0

Table 5.1: TRAC boom Z-bending loads (expressed in $[N]$)

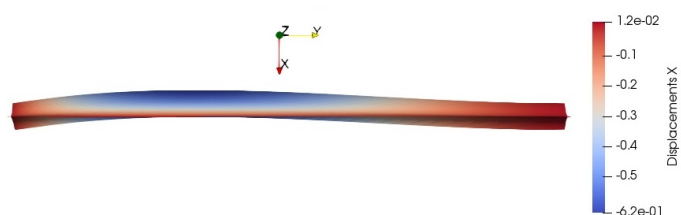
Location	U_X	U_Y	U_Z
A	0	<i>free</i>	0

Table 5.2: TRAC boom Z-bending boundary conditions

The graphical result of the analysis is shown in Fig. 5.9, where a scale factor of 20 is applied. The two sub-figures represent the side and the top view, and the color contour shows the U_Z and the U_X , respectively. As can be seen, the boom correctly rotates around the Z-axis, and the deformed shape presents a pronounced hunchback at about the 30% of its length. Curiously, the vertical flange is nearly undeformed at all, maybe due to the loads and BCs dispositions. Another interesting thing to underline is that a slight downward bend is also visible from the side view, in the same position as the lateral hunchback already described. On the other side, not visible in the figure, the bend is upward.



(a) Side view. Contour represents U_Z



(b) Top view. Contour represents U_X

Figure 5.9: Deformed shape of the TRAC boom subjected to $M_Z = 1000 \text{ Nmm}$, linear static analysis. Scale factor of 20

The rotation measured in the frontal cross-section is equal to $\theta_Z = 0.282^\circ$. This result will be compared later with the equilibrium curve obtained with the non-linear analysis on the same structure.

5.2.2 X-bending

In the X-bending, due to the asymmetry of the problem, both the positive and negative rotation must be analyzed. Nevertheless, the mesh is the same for both

the load configuration, and the only things that change are the signs of the loads.

The cross-section mesh, differently from the one adopted for the Z-bending, has got 34 L9 elements, for a total amount of 195 nodes. This addition of two elements is due to a reason of loads balancing, in order to have the resulting force exactly in the same location of the resulting BC. Thus, the cross-section mesh is visible in Fig. 5.10, with the vertical flange detail in Fig. 5.11. Here, again, the purple triangles indicate the edges of the elements. The only difference from the mesh with 32 L9 used in the Z-bending is in the top part of the vertical flange, where the first element has been further fractioned; the remaining parts of the mesh are unchanged.

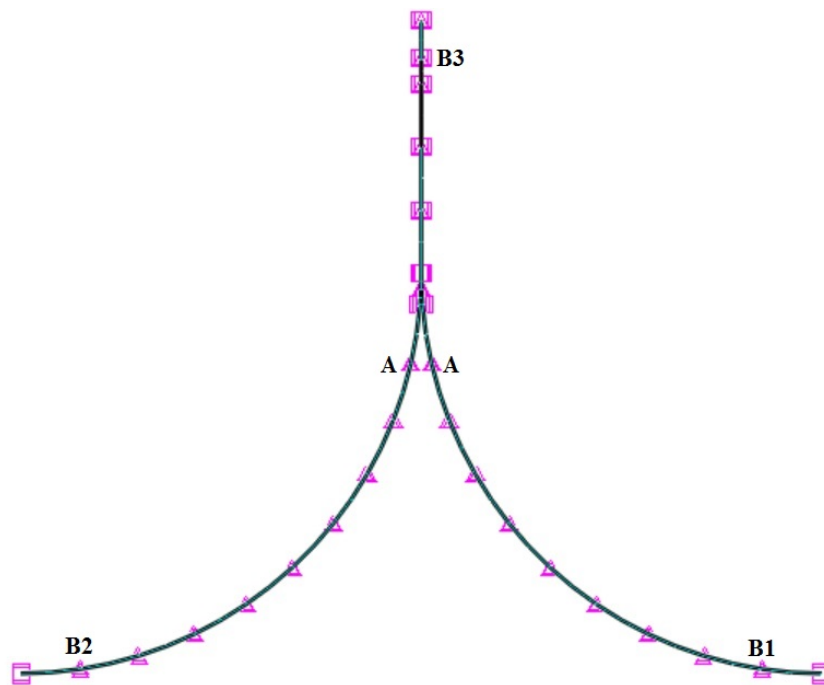


Figure 5.10: TRAC boom cross-section mesh for the X-Bending configuration. Each of the triangle represents the edge of an element. Letters indicate the nodes upon which BCs and loads are applied, BCs in A, loads in B. 34 L9

In points *A* the BCs are applied, and only the translation along the *Y*-axis is permitted, avoiding any torsional rotation; in points *B* are the concentrated forces, according to Tab. 5.3, which describes how a positive moment is created (for a negative one, one changes the signs). This set of forces is created in order to obtain a moment equal to $M_X = 2000 \text{ Nmm}$, given the *Z*-distance of the top



Figure 5.11: Detail of the vertical flange of the cross-section of Fig. 5.10, together with the conjunction zone. 14 L9 elements on this flange

and bottom forces equals to $d = 19.36104 \text{ mm}$.

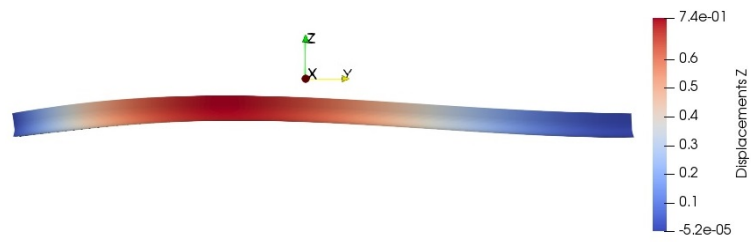
Location	F_X	F_Y	F_Z
B_1	0	51.65	0
B_2	0	51.65	0
B_3	0	-103.3	0

Table 5.3: TRAC boom X-bending loads (expressed in $[N]$). For a negative moment the all the signs must be changed

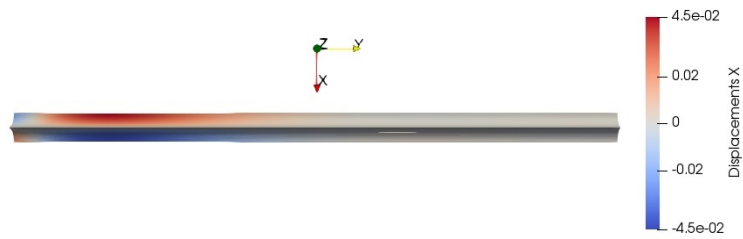
Location	U_X	U_Y	U_Z
A	0	<i>free</i>	0

Table 5.4: TRAC boom X-bending boundary conditions

The deformed shapes of the TRAC boom are visible in Fig. 5.12 and Fig. 5.13, which show equal sense and opposite sense bending, respectively. When the moment is positive, the boom correctly bends upward, always in the same part where it twists when subjected to M_Z ; curiously, looking at the top view, one can see that in the first part of the boom is visible a constriction, which makes the

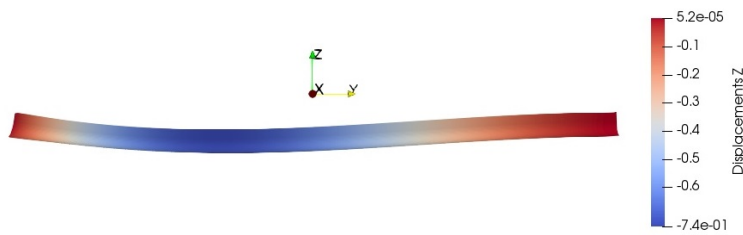


(a) Side view. Contour represents U_Z

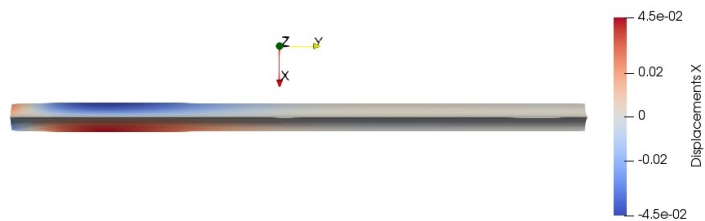


(b) Top view. Contour represents U_X

Figure 5.12: Deformed shape of the TRAC boom subjected to $M_X = 2000 \text{ Nmm}$, linear static analysis. Scale factor of 20



(a) Side view. Contour represents U_Z



(b) Top view. Contour represents U_X

Figure 5.13: Deformed shape of the TRAC boom subjected to $M_X = -2000 \text{ Nmm}$, linear static analysis. Scale factor of 20

two curved flanges approach each other. Apart from this peculiar behavior, no other buckling deformation is encountered. On the other hand, when a negative moment is applied, the effect is the opposite of the one just described: the boom is flexed downward, and the curved flanges flatten, moving away from each other.

The measured rotation due to $M = \pm 2000 \text{ Nmm}$ is equal to $\theta_X = \pm 0.451^\circ$. The rotation is hence the symmetrical with respect to the zero. This property must then be confirmed by the equilibrium curve obtained with the non-linear analysis.

5.3 Linearized buckling analysis

In this section, some graphical results given by the linearized buckling analysis are described. Three different analyses have been carried out, under three different load conditions: uniform compression, positive X-bending, positive Z-bending. The deformed shapes corresponding to the most interesting modes are shown in Fig. 5.14, Fig. 5.15 and Fig. 5.16, which represent the compression, M_X , and M_Z , respectively.

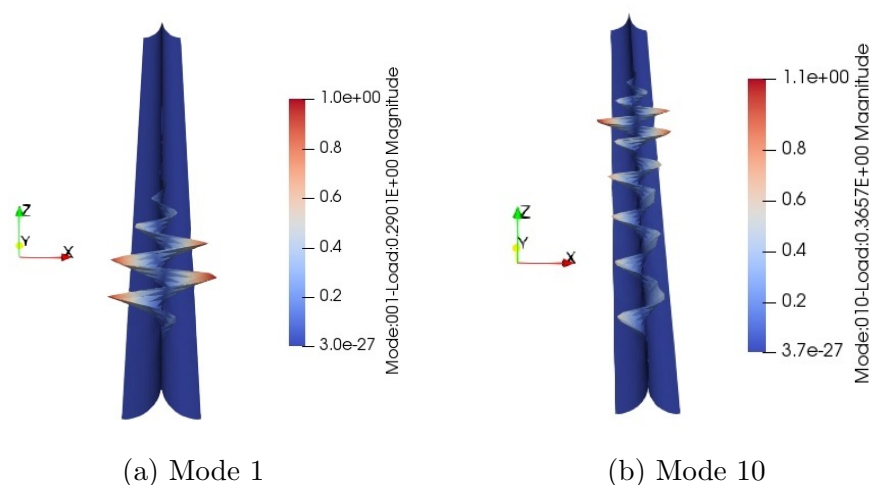


Figure 5.14: Deformed shapes of the TRAC boom subjected to uniform compression, buckling analysis. Scale factor of 20

All of the analyses have been carried out on the TRAC boom in the 500 mm long configuration. Thus, calling back the meshes already described in Sec. 5.2,

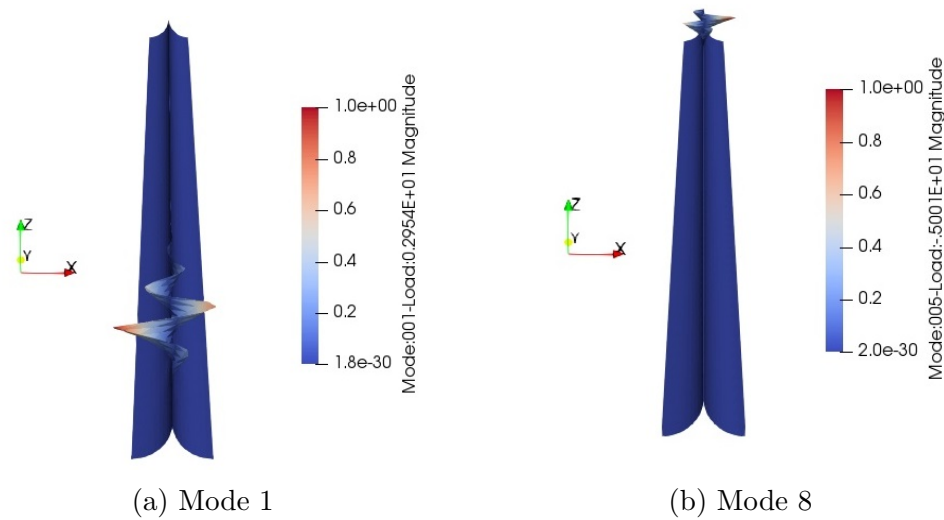
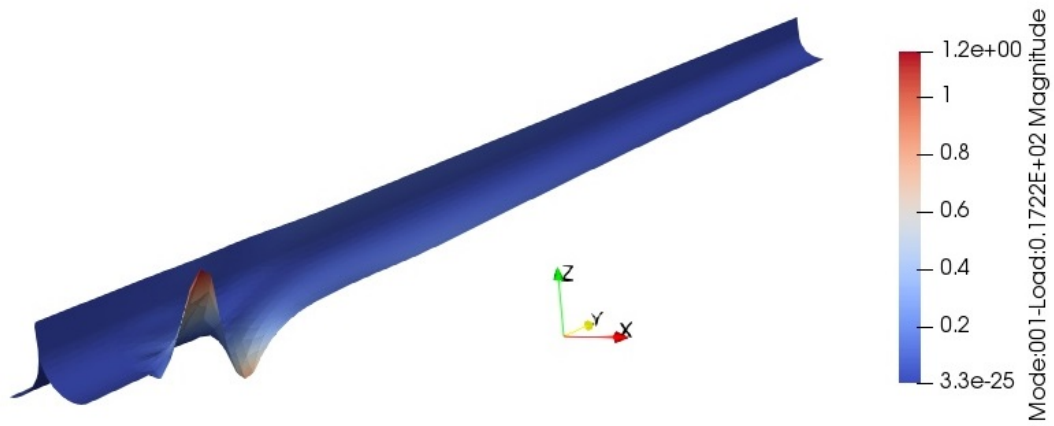


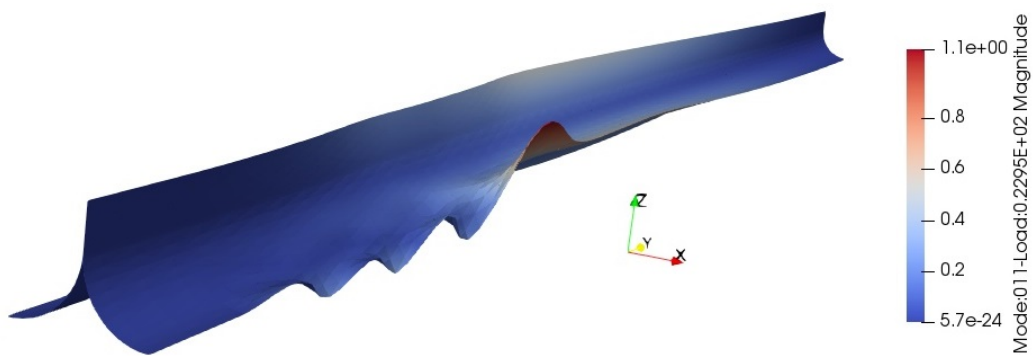
Figure 5.15: Deformed shapes of the TRAC boom subjected X-bending, buckling analysis. Scale factor of 20

21 B4 elements are present along the longitudinal axis (the first is more rigid than the others), and the cross-section located at the end of the boom (where the Y-axis is outgoing) is clamped. Depending on the load configuration, meshes and loads on the frontal cross-section are different: for the X-bending, a 34 L9 mesh is adopted (Fig. 5.10), while for the Z-bending a 32 L9 mesh is preferred (Fig. 5.7). On the other hand, a different approach is used for the compression case: in order to simulate a uniform pressure, on every node of the cross-section mesh a force has been applied; having adopted the 32 L9 mesh, 185 concentrated forces are created, as much as the number of the nodes on that cross-section. BC in the frontal cross-section is imposed to make it only slide along the Y-axis.

The first 10 critical loads are listed in Tab. 5.5.



(a) Mode 1



(b) Mode 6

Figure 5.16: Deformed shapes of the TRAC boom subjected Z-bending, buckling analysis. Scale factor of 20

Mode	Compression [N]	X-bending [Nmm]	Z-bending [Nmm]
1	53.67	-295	1722
2	54.06	-302	1879
3	57.26	-346	1955
4	57.61	-358	2060
5	60.44	-403	2169
6	60.96	-421	2295
7	63.42	-476	2394
8	64.25	500	2459
9	66.56	517	2564
10	67.65	628	2725

Table 5.5: TRAC boom first critical loads

Fig. 5.14 shows that the buckling with a compression load associated with Mode 1 takes place in the first part of the boom, producing a series of waves in the vertical flange. The waves amplitude decreases moving toward the end of the boom and stops completely near the middle of the total length. As the modes advance, the waves move toward the end of the boom, until all the length is wavy.

Very similar behavior is noticed when a negative X-bending is applied, aimed at compressing the vertical flange, even if the waves are less pronounced. On the other hand, the effect produced by a positive M_X is the opposite, as it creates the waves in the final part of the boom, where it is clamped.

Different is the buckling behavior when a Z-bending is applied, as shown in Fig. 5.16. Here the flange where the waves are registered is the one on the right, and they take place, in Mode 1, immediately after the end of the rigid element, extinguishing themselves in a few crests. Increasing the number of the mode waves move again toward the end of the boom, and a deflection of the vertical flange can be seen too.

In conclusion, the buckling shapes obtained with this linearized buckling analysis show that usually instabilities take place in the flanges, which tend to bend into a series of waves in the first part of the boom. In the next section, dealing with the non-linear static analysis, these statements will be investigated.

5.4 Non-linear analysis and sensitivity versus boom length

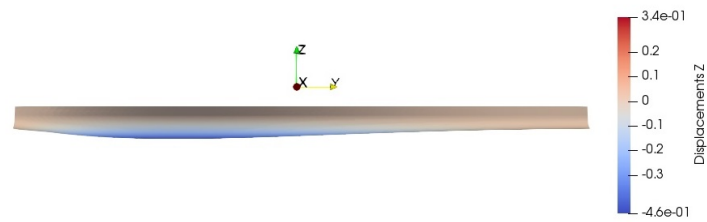
In this section, the non-linear analyses of the TRAC boom structure are documented, starting from the meshes and loads conditions adopted in the linear analyses described in the previous section. For this reason, every time a new analysis is presented, the corresponding mesh is referred to thanks to the figures of Sec. 5.2, and the figure is not repeated here again. As it was already done in that section, this one is subdivided into two main subsections, describing the Z-bending and the X-bending. Each subsection begins with a first non-linear curve corresponding to the 500 mm boom, and also reporting the result of the linear analysis obtained in Sec. 5.2; afterward, a parametric analysis is made, studying the effect of the boom length on the equilibrium curve.

5.4.1 Z-bending

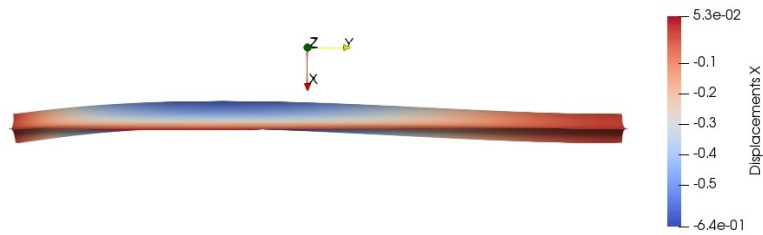
The geometry and the mesh of the cross-section, together with the loads and BCs disposition, are not varied with respect to the linear analysis of Sec. 5.2.1. For this reason, the geometry is the one in Fig. 5.5, the mesh is shown in Fig. 5.7 and Fig. 5.8, and the load disposition is the same as already described in that section. The intensities of the forces are not the same as the one in Tab. 5.1, because now a non-linear analysis must be carried out, and the intensity changes during the analysis itself; the only thing that must remain unchanged is the equality between the two moduli. The axial mesh is also the same and consists of 21 B4 elements, the first more rigid than the other 20 ($E = 21000 \text{ GPa}$ instead of $E = 210 \text{ GPa}$).

Comparison with linear and buckling analysis

The graphical result of the non-linear analysis, at the same moment intensity of $M_Z = 1000 \text{ Nmm}$ as the one used for the linear analysis, is shown in Fig. 5.17. The deformed shape is the same as the one obtained in the linear analysis and visible in Fig. 5.9: the central part of the boom is subjected to a flex-torsional movement, which makes deflect downward the curved flange on the positive side of the X-axis. Again, no buckling is yet encountered on the vertical flange.



(a) Side view. Contour represents U_Z



(b) Top view. Contour represents U_X

Figure 5.17: Deformed shape of the TRAC boom subjected to $M_Z = 1000 \text{ Nmm}$, Non-linear static analysis. Scale factor of 20

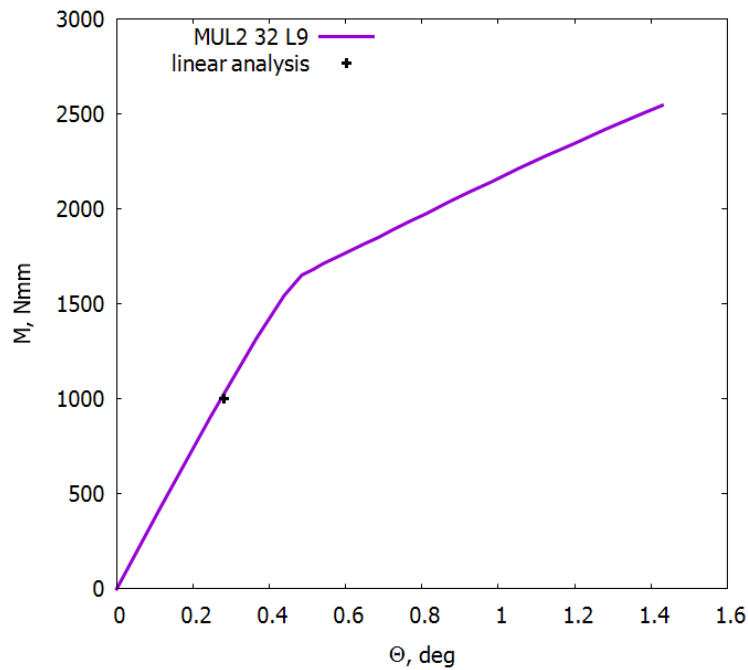


Figure 5.18: TRAC boom 500 mm long, equilibrium curve under Z-bending. Linear analysis result is included

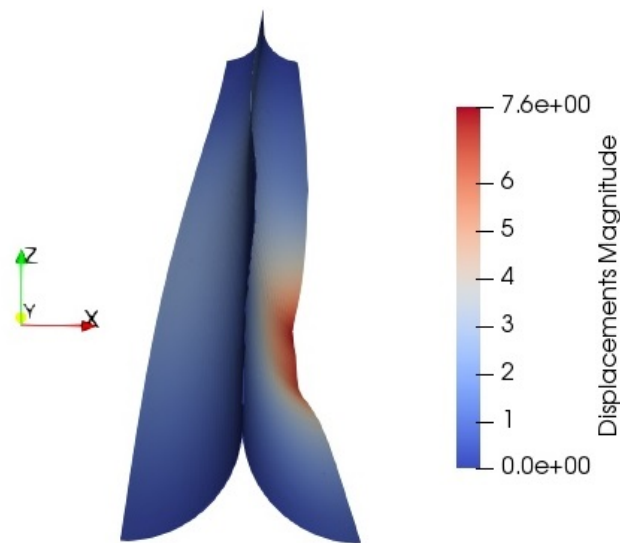


Figure 5.19: TRAC boom 500 mm long deformed shape at the end of the equilibrium curve ($M_Z = 2546 \text{ Nmm}$, $\theta = 1.43^\circ$)

The equilibrium curve is represented in Fig. 5.18, where also the result of the linear analysis is enclosed. As can be seen with the curve, the buckling load is reached at about $M = 1700 \text{ Nmm}$, where the curve sharply deflects from the linear trend had so far. This fact is consistent with the fact that the linear and non-linear analyses do not differ from each other at a lower moment. Over that intensity, as said, the buckling occurs, and the rigidity of the boom drops.

At the end of the curve, the situation is the one in Fig. 5.19. The shape has become completely asymmetric, as the right flange is collapsed under the compression to which it is subjected, while the left flange, subjected to traction, has flattened itself. The vertical flange is not entirely straight anymore, but some ripple is visible. Probably, if the analysis should go on, the boom would collapse in the red region and bend there. This result is also in agreement with the linearized buckling analysis, where the first critical buckling load obtained was 1722 Nmm ; moreover, the region where the right flange collapses coincides with the region where the waves were noticed in Fig. 5.16.

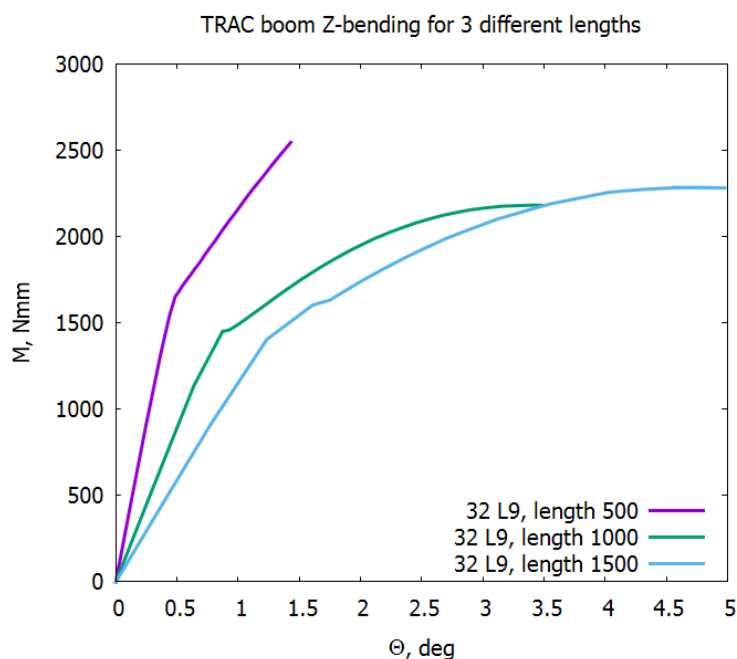


Figure 5.20: TRAC boom equilibrium curve under Z-bending for three different lengths

Parametric analysis

It is now the moment to change the length of the boom and see how it afflicts the equilibrium curve. Thus, in addition to the already presented analysis of the 500 *mm* boom, two new analyses dealing with a 1000 *mm* and a 1500 *mm* long booms are carried out and presented hereafter. The cross-section mesh is the same as before, the only thing that slightly changes is the longitudinal mesh, which remains composed of 21 B4 elements, but now the first rigid element is shorter than the others: the rigid element is maintained 25 *mm* long, while the rest of the boom is subdivided into equal parts (for example, in the 1000 *mm* boom there are 20 B4 elements each 50 *mm* long).

The results of the analyses are contained in the graph of Fig. 5.20. It shows that the more is the length, the less is the rigidity of the structure, as the linear slope of the curve is inversely proportional to the length. Also, the buckling load slightly decreases with the length, reaching a value of about 1500 *Nmm* for the 1500 *mm* configuration. The two new curves, unlike the 500 *mm* one, over the

buckling load begin to flatten, reaching a horizontal trend.

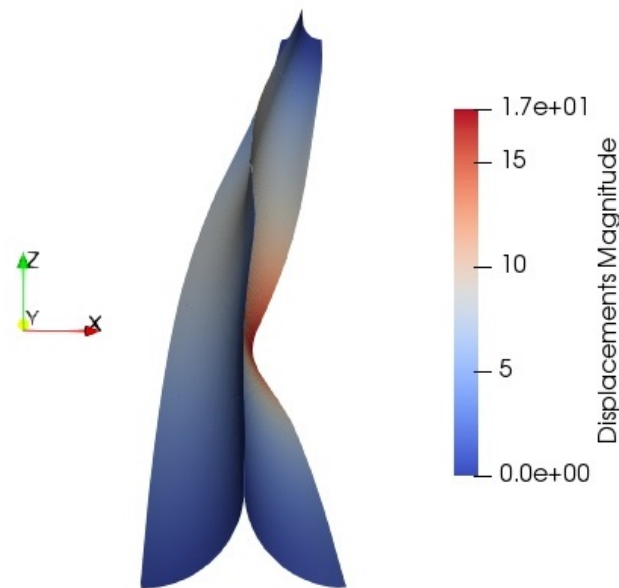


Figure 5.21: TRAC boom 1000 *mm* long deformed shape at the end of the equilibrium curve ($M_Z = 2185 \text{ Nmm}$, $\theta = 3.40^\circ$)

In Fig. 5.21 and Fig. 5.22 the two deformed shapes at the end of the equilibrium curve, for the 1000 *mm* and the 1500 *mm* respectively, are shown.

The deformed shape relative to the 1000 *mm* long boom is quite similar to the one of Fig. 5.19, but the right flange collapse here is even more pronounced, and in addition to the downward bending also an inward one can be seen; the vertical flange is also definitely deformed, mainly following the boom rotation, but with several little local buckling along its length.

Rising the value of the length to 1500 *mm* the right flange collapse is not alone anymore, but a new bending, this time upward, is registered a little further downstream. Moreover, the vertical flange is wholly deformed, with the most significant deformation right in correspondence of the collapses of the right flange. The further rotation could lead to even more collapsing, extended over all the boom length.

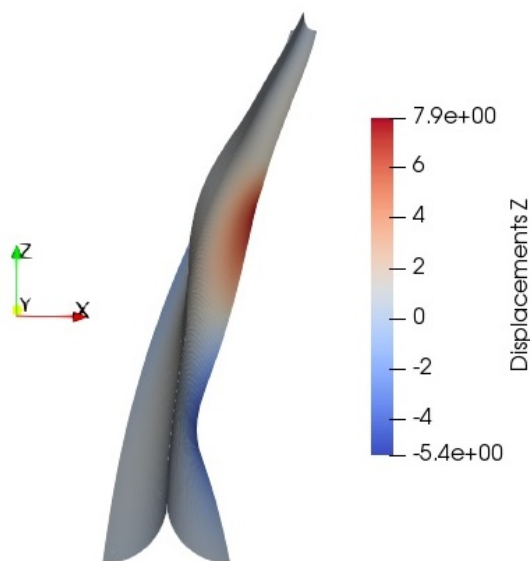


Figure 5.22: TRAC boom 1500 *mm* long deformed shape at the end of the equilibrium curve ($M_Z = 2293 \text{ Nmm}$, $\theta = 4.71^\circ$)

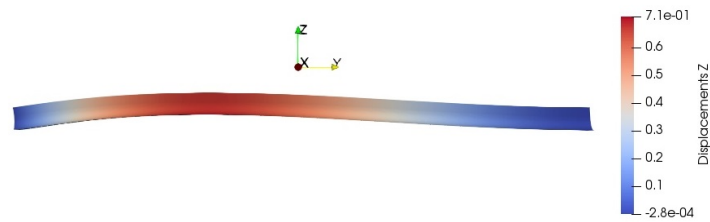
5.4.2 X-bending

The geometry, the cross-section mesh, the loads and BCs disposition, and the materials are not changed with respect to the linear analysis. Fig. 5.5, Fig. 5.10 and Fig. 5.11 can thus give all the useful information about the analysis. Hence, the cross-section mesh consists of 34 L9 elements, and the axial mesh of 21 B4 elements (the first of them is 100 times more rigid than the others, and it is 25 *mm* long independently from the boom length). The loads are not constant but vary during the analysis proceeding. Moreover, one must remember that for the X-bending both the positive and the negative moments must be taken into account.

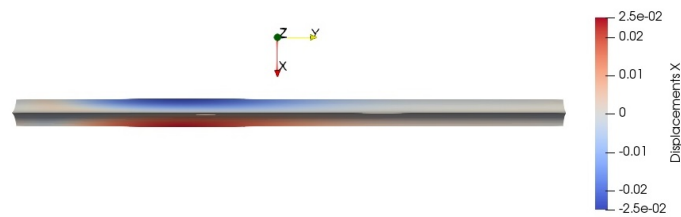
Comparison with linear and buckling analysis

The deformed shapes associated with the moment $M_X = \pm 2000 \text{ Nmm}$, the same value as the linear analysis, are shown in Fig. 5.26 and Fig. 5.27, which represent the equal sense and the opposite sense bending, respectively.

The results for the equal sense bending are quite unexpected, as the curved flanges, which in the linear analysis were approaching each other (Fig. 5.12), here

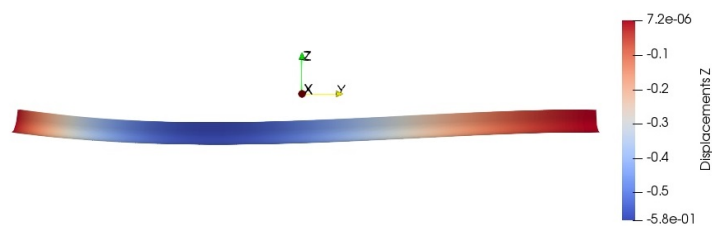


(a) Side view. Contour represents U_Z

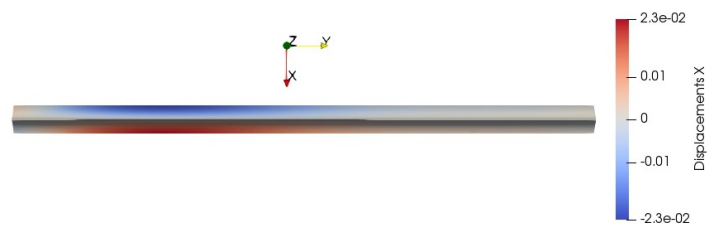


(b) Top view. Contour represents U_X

Figure 5.23: Deformed shape of the TRAC boom subjected to $M_X = 2000 \text{ Nmm}$, Non-linear static analysis. Scale factor of 20



(a) Side view. Contour represents U_Z



(b) Top view. Contour represents U_X

Figure 5.24: Deformed shape of the TRAC boom subjected to $M_X = -2000 \text{ Nmm}$, Non-linear static analysis. Scale factor of 20

tend to flatten themselves, with a behavior that is precisely the opposite than before. No changes are visible for the opposite sense bending; instead, it deforms the same as the linear analysis (Fig. 5.13). Thus, the linear analysis was not able to capture the flattening of the curved flanges correctly.

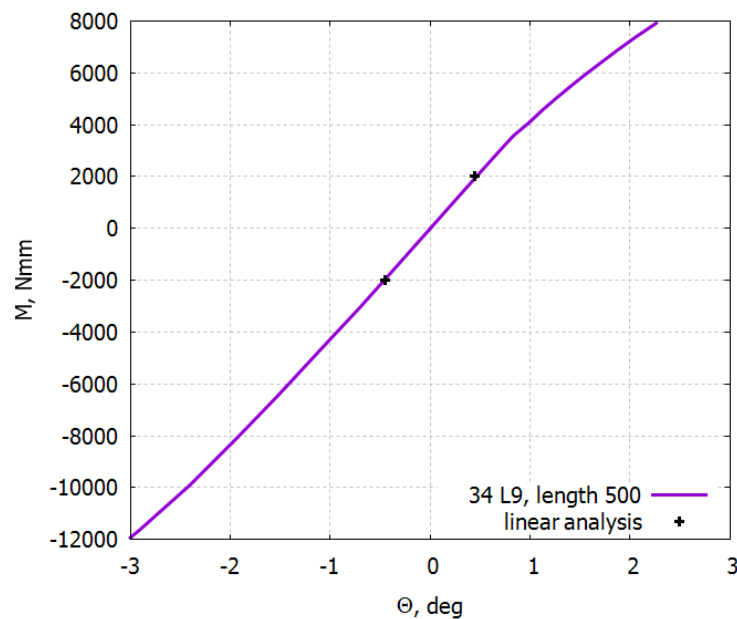


Figure 5.25: TRAC boom 500 *mm* long, equilibrium curve under X-bending. Linear analysis result is included

In Fig. 5.25 the equilibrium curve is shown, together with the linear analysis results. Despite the differences encountered in the deformed shape, the linear solution matches the non-linear one. On the other end, the buckling analysis gave as results that the first critical load was equal to -295 Nmm , much more content than the moments encountered here. In fact, the non-linear equilibrium curve is not very irregular, and only a minimal decrease in the rigidity is registered for high moment values. This fact is also in agreement with the deformation shapes at the two ends of the curve, shown in Fig. 5.26 and Fig. 5.27, where a proper buckling can not be seen. In fact, in the equal sense case, there is only a pronounced hunchback in the first part of the boom (right after the rigid element), but no other particular irregularities are encountered. In the opposite sense bending the deflection of the flanges is outward, and only in the very final part of the boom a

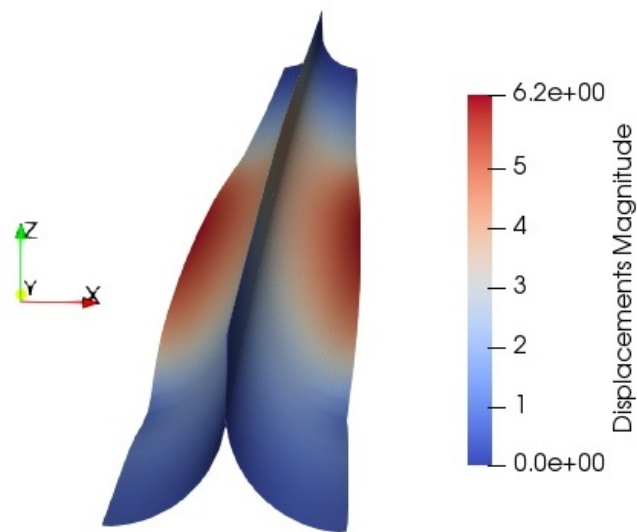


Figure 5.26: TRAC boom 500 mm long deformed shape at the end of the equilibrium curve ($M_X = 7923 \text{ Nmm}$, $\theta = 2.26^\circ$)

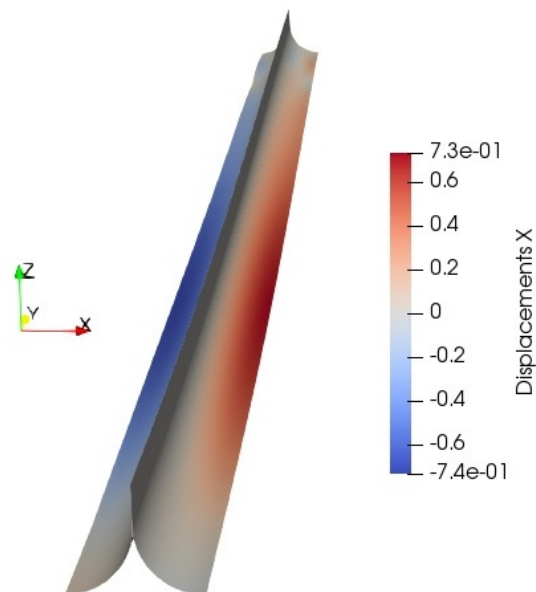


Figure 5.27: TRAC boom 500 mm long deformed shape at the end of the equilibrium curve ($M_X = -11597 \text{ Nmm}$, $\theta = -2.89^\circ$)

counter-deflection is visible. In both cases, the vertical flange is always undeformed and follows a nearly straight line. None effects at all are visible on the vertical flange, in both cases, and this is not in agreement with the buckling analysis, which expected a series of waves on it.

In conclusion, X-bending is highly influenced by geometry and loads defects, and in their absence the buckling could not verify. If some instabilities take place, on the other hand, the equilibrium curve could deflect from the linear trend earlier.

Parametric analysis

The effects of the variation of the boom length are visible in the graph of Fig. 5.28, where the equilibrium curves of the 1000 mm and 1500 mm configurations are added to the one already described relative to the 500 mm boom.

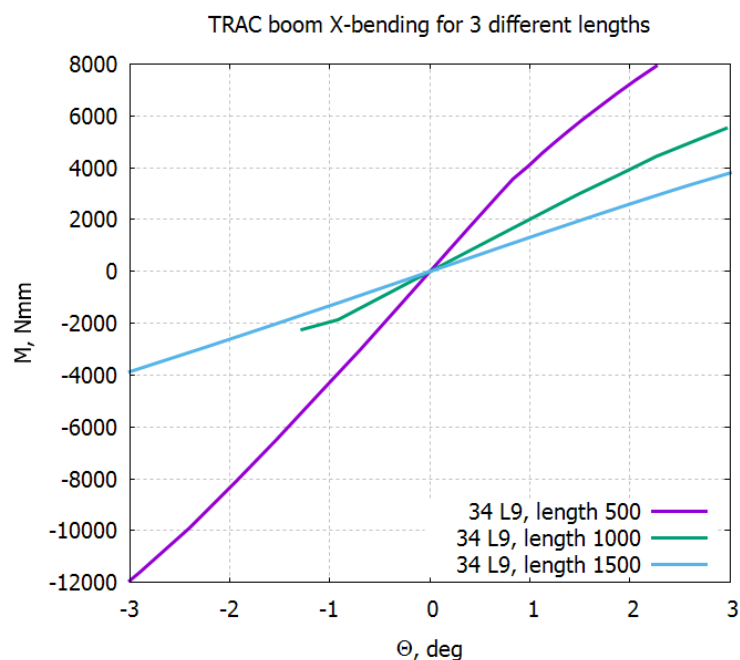


Figure 5.28: TRAC boom equilibrium curve under X-bending for three different lengths

According to Fig. 5.28 the rigidity of the TRAC booms decrease with increasing lengths, making the structure easier to bend. On the other hand, the buckling load does not seem to have easily predictable behavior, as the green curve relative to

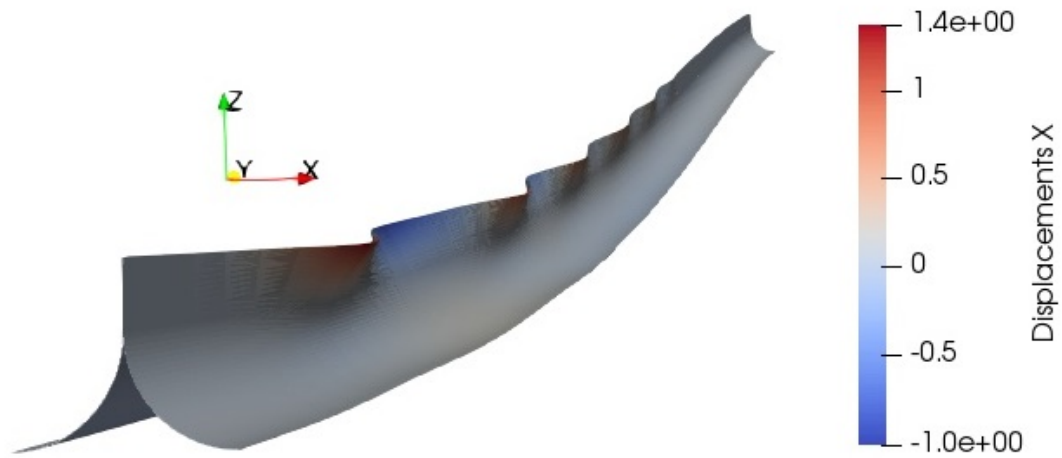


Figure 5.29: TRAC boom 1000 *mm* long deformed shape at the end of the equilibrium curve in the opposite sense bending ($M_X = -2238 \text{ Nmm}$, $\theta = -1.28^\circ$). Scale factor of 5

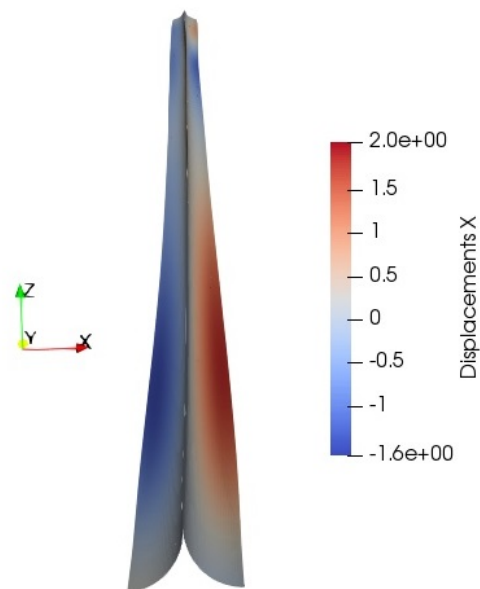


Figure 5.30: TRAC boom 1500 *mm* long deformed shape at the end of the equilibrium curve in the opposite sense bending ($M_X = -10366 \text{ Nmm}$, $\theta = -9.55^\circ$)

the 1000 *mm* boom, for example, has got a sharp early buckling for a relatively low moment, whereas the 1500 *mm* boom is practically linear in all the rotation range considered. Further studies on this problem could lead to the addition of a defect to the structure, which could anticipate the buckling in the curve.

The deformed shapes are visible in Fig. 5.29 and Fig. 5.30. They represent only the opposite sense bending, as the equal sense has not registered any specific behavior, maintaining a pre-buckling shape. On the other hand, very interesting is the result obtained in the 1000 *mm* case, where the vertical flange is completely in post-buckling, with a series of waves visible with the scale factor of 5. This behavior is strictly connected to the unusual shape of the corresponding equilibrium curve, and hence this must be a typical unstable solution. Much more regular is the 1500 *mm* long boom instead, where the only thing that stands out is a little bend near the end of the boom, which deflects downward the right flange.

Conclusions

The present work dealt mainly with the analysis of thin-walled structures having the first property to be deployable, an essential feature in space applications. The study on deployable structures provided the tools needed to order and classify different kinds of space objects, determining their application fields, and discovering some important realizations.

The CUF theory has been proved to be very versatile, and all sorts of structures can be easily modeled with the use of Lagrangian and beam elements on the cross-section and axis, respectively. A very impressive characteristic of the CUF modeling is that the cross-section can be built in a completely separated way from the axis mesh, and this thing is a significant work simplification.

The work went on with the actual applications of the CUF modeling on the analysis of typical space deployable structures. In the beginning, some preliminary analysis carried out on standard shaped beams, allowed to demonstrate the ability of the Mul² code to replicate very well the results present in the literature on these simple structures analysis. In the following chapter the analysis of tape spring structures permitted to evaluate all the peculiarities of the equilibrium curve of these particular deployable elements accurately; Mul² code gave the proof to be very reliable also for these highly thin structures, matching the curves obtained by the Abaqus software in all cases treated. Successively, further comparison with an experimental test proved that the non-linear post-buckling behavior of tape spring measures could be reasonably well replicated too. In the final chapter, a series of analyses on TRAC boom structures permitted to evaluate their buckling properties, with a focus on the effects of the boom length on the mechanical features.

All of the analyses made in this work have been carried out on isotropic metallic structures, and future development could be the extension to composite materials,

which need a much more significant amount of calculation time using the Mul² code. Moreover, only two typical deployable structures have been analyzed; this work can then continue with the study of different structures, such as membranes, for example. The ability to predict as accurately as possible the behavior of these deployable structures is essential, because the projects involving these elements need to know how the structure moves, and the forces needed to the folding and unfolding processes.

In conclusion, an in-depth study on deployable structures for space applications made understand all possible fields in which these structures can be used, and how the CUF theory can be adapted to model them, with a relatively high level of simplicity and accuracy of results.

Bibliography

- [1] Manan Arya, Nicolas Lee, and Sergio Pellegrino. Ultralight structures for space solar power satellites. 01 2016.
- [2] Jeremy Banik and Thomas Murphey. Performance validation of the triangular rollable and collapsible mast. 2010.
- [3] Klaus-Jürgen Bathe. *Finite element procedures*. Klaus-Jurgen Bathe, 2006.
- [4] K. E. BISSHOPP and D. C. DRUCKER. Large deflection of cantilever beams. *Quarterly of Applied Mathematics*, 3(3):272–275, 1945.
- [5] E Carrera. A study on arc-length-type methods and their operation failures illustrated by a simple model. *Computers & structures*, 50(2):217–229, 1994.
- [6] Erasmo Carrera, Maria Cinefra, Marco Petrolo, and Enrico Zappino. *Finite element analysis of structures through unified formulation*. John Wiley & Sons, 2014.
- [7] Erasmo Carrera, Gaetano Giunta, and Marco Petrolo. *Beam structures: classical and advanced theories*. John Wiley & Sons, 2011.
- [8] Erasmo Carrera and Marco Petrolo. Refined beam elements with only displacement variables and plate/shell capabilities. *Meccanica*, 47(3):537–556, 2012.
- [9] Michael A Crisfield. A fast incremental/iterative solution procedure that handles “snap-through”. In *Computational Methods in Nonlinear Structural and Solid Mechanics*, pages 55–62. Elsevier, 1981.

- [10] Leonhard Euler. *Methodus inveniendi lineas curvas maximi minimive proprietate gaudentes*. apud Marcum-Michaelem Bousquet, 1744.
- [11] Giulia E Fenci and Neil GR Currie. Deployable structures classification: A review. *International Journal of Space Structures*, 32(2):112–130, 2017.
- [12] Annette Fischer. *Bending instabilities of thin-walled transversely curved metallic strips*. University of Cambridge, Department of Engineering, 1995.
- [13] RE Freeland, GD Bilyeu, GR Veal, and MM Mikulas. Inflatable deployable space structures technology summary. 1998.
- [14] Gokhan Kiper and Eres Soylemez. Deployable space structures. In *2009 4th International Conference on Recent Advances in Space Technologies*, pages 131–138. IEEE, 2009.
- [15] Christophe Leclerc and Sergio Pellegrino. Ultra-thin composite deployable booms. In *Proceedings of IASS Annual Symposia*, volume 2017, pages 1–9. International Association for Shell and Spatial Structures (IASS), 2017.
- [16] Christophe Leclerc, Lee L Wilson, Miguel A Bessa, and Sergio Pellegrino. Characterization of ultra-thin composite triangular rollable and collapsible booms. In *4th AIAA Spacecraft Structures Conference*, page 0172, 2017.
- [17] Chinthaka Mallikarachchi and Sergio Pellegrino. Design and validation of thin-walled composite deployable booms with tape-spring hinges. *Collection of Technical Papers - AIAA/ASME/ASCE/AHS/ASC Structures, Structural Dynamics and Materials Conference*, 04 2011.
- [18] H. M. Y. C. Mallikarachchi. Thin-walled composite deployable booms with tape-spring hinges. 2011.
- [19] Eric Harold Mansfield. Large-deflexion torsion and flexure of initially curved strips. *Proceedings of the Royal Society of London. A. Mathematical and Physical Sciences*, 334(1598):279–298, 1973.
- [20] Koryo Miura. Method of packaging and deployment of large membranes in space. *Title The Institute of Space and Astronautical Science Report*, 618:1, 1985.

- [21] Koryo Miura. Concepts of deployable space structures. *International Journal of Space Structures*, 8(1-2):3–16, 1993.
- [22] A. Pagani and E. Carrera. Unified formulation of geometrically nonlinear refined beam theories. *Mechanics of Advanced Materials and Structures*, 25(1):15–31, 2018.
- [23] Sergio Pellegrino. *Deployable structures*, volume 412. Springer, 2014.
- [24] Junuthula Narasimha Reddy. *An Introduction to Nonlinear Finite Element Analysis: with applications to heat transfer, fluid mechanics, and solid mechanics*. OUP Oxford, 2014.
- [25] Friedrich Paul Johannes Rimrott. Two secondary effects in bending of slit thin-walled tubes. 1966.
- [26] Esther Rivas-Adrover. *Deployable Structures*. 01 2015.
- [27] Francisco Roybal, Jeremy Banik, and Thomas Murphey. Development of an elastically deployable boom for tensioned planar structures. In *48th AIAA/ASME/ASCE/AHS/ASC Structures, Structural Dynamics, and Materials Conference*, page 1838, 2007.
- [28] KA Seffen and S Pellegrino. Deployment of a rigid panel by tape-springs. 1997.
- [29] Keith Alexander Seffen. *Analysis of structures deployed by tape-springs*. PhD thesis, University of Cambridge, 1997.
- [30] Stephan P Timoshenko. X. on the transverse vibrations of bars of uniform cross-section. *The London, Edinburgh, and Dublin Philosophical Magazine and Journal of Science*, 43(253):125–131, 1922.
- [31] Kyuichiro Washizu. *Variational methods in elasticity and plasticity*, volume 3. Pergamon press Oxford, 1975.
- [32] Z You and S Pellegrino. Cable-stiffened pantographic deployable structures. i-triangular mast. *AIAA journal*, 34(4):813–820, 1996.